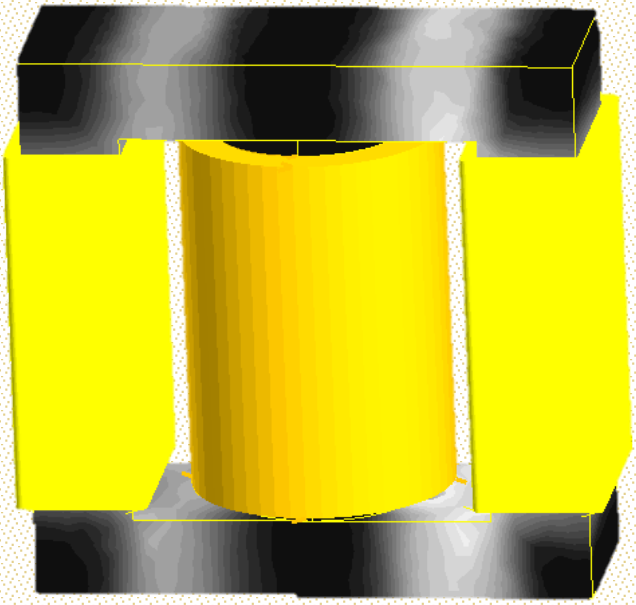

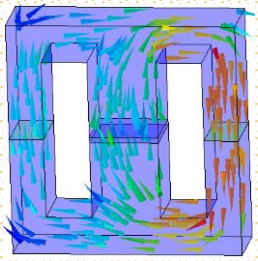

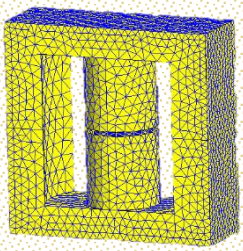

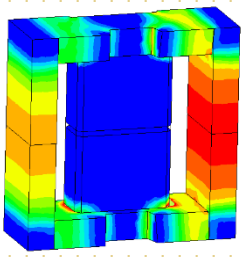

Samuel Filipe Soares Ferreira

Electromagnetic study of a variable inductor controlled by a DC current

Dissertation presented in partial fulfillment of the requirements for the degree of Master in Electrical and Computer Engineering at the University of Coimbra, specialization area of Energy, under the coordination of Professor André Manuel dos Santos Mendes, Auxiliar Professor in the Department of Electrical and Computer Engineering of the Faculty of Science and Technology of the University of Coimbra and Professor Marina Mendes Sargento Domingues Perdigão, Assistant Professor in the Department of Electrical Engineering of the Polytechnic Institute of Coimbra.

January of 2016

· U C ·

Universidade de Coimbra

• U C • FCTUC FACULDADE DE CIÊNCIAS
E TECNOLOGIA
UNIVERSIDADE DE COIMBRA

Estudo do comportamento eletromagnético de uma bobina variável controlada através de uma corrente DC

Tese de Mestrado

Dissertação submetida para obtenção do grau de Mestre em Engenharia Electrotécnica e de Computadores, na Área de Especialização em Energia, elaborada sob a orientação do Professor André Manuel dos Santos Mendes, Professor Auxiliar no Departamento de Engenharia Electrotécnica e de Computadores da Faculdade de Ciências e Tecnologia da Universidade de Coimbra e da Professora Marina Mendes Sargento Domingues Perdigão, professora assistente no Departamento de Engenharia Electrotécnica do Instituto Superior de Engenharia de Coimbra e apresentada no Departamento de Engenharia Electrotécnica e de Computadores da Faculdade de Ciências e Tecnologia da Universidade de Coimbra.

Autor:

Samuel Filipe Soares Ferreira

Juri:

António Paulo Mendes Breda Dias Coimbra (Presidente)

André Manuel dos Santos Mendes (Vogal)

Tony Richard de Oliveira de Almeida (Vogal)

Classificação final:

20 valores

Janeiro de 2016

“To God be the glory forever and ever! Amen.”

Galatians 1:5

ACKNOWLEDGMENTS

First and foremost, I would like to express my deepest gratitude to God, the creator of the Universe, science and everything that was, is and will be. The One who showed me the greatest expression of love as He did not spare his own son but delivered him to die on a tree so I, his enemy, could be set free. Moreover, He is the One who has been supporting me in all aspects of my life and, without Him, this work would not be possible.

I would also like to express my sincere appreciation toward Professor André Mendes and Professor Marina Perdigão. Their patience, guidance, wise, invaluable advice and help were key motivations throughout this work. I wish to thank Professor André for his encouraging speeches and care for the students, which have been a reality since the begging of his lectures. He allowed, not only I, but many other students to be engaged, continue motivated and passionate for electrical subjects. I am also indebted to Professor Marina Perdigão for her continuous advice, concern and for always being available to help.

I wish to thank my colleagues from the IT-Coimbra group and Laboratório de Electrónica Potência, particularly to Marco Martins, Valter Costa and Fábio Gonçalves. I am grateful for their help support and valuable hints.

I also would like to thank to Professor Eduardo Saraiva for review a part of this thesis and share his knowledge about electromagnetism and variable inductors. Moreover, I would like to thank Leah Gois, Ana Hemborough and Ana Isabel for valuable assistance to review sections of this work.

In addition, I would like to express a special gratitude to my family for their patience and support.

I am also very grateful to the professors from the Departamento de Engenharia Electrotécnica e de Computadores da Universidade de Coimbra that greatly contributed to my training during the past years.

Finally, I would like to thank my closest friends, for their support, encouragement and good times.

ABSTRACT

Energy efficiency regulations and the pursuit of more efficient power control systems increased the demand for research on Variable Inductor (VI), in the recent years. As the name indicates, a variable inductor is a device capable of varying its own inductance.

This thesis presents a thorough electromagnetic analysis of the operation of double E-shaped Linear Variable Inductors (LVI). In the studied VI topology, a DC current is used to control the inductance of the VI through a series of electromagnetic phenomena. Therefore, to conduct the electromagnetic analysis a Finite Element Analysis (FEA) software is used. Some 3D VI models are built in the software and studied throughout this thesis. The obtained FEA results are analysed and compared with different models and experimental results.

A critical analysis to the magnetic permeability concept is also described in this thesis. The magnetic permeability is proved to be inefficient to analyse multi-sourced non-linear magnetic systems. The former is then replaced by the differential magnetic permeability which, in turn, is shown to be the property that best characterizes the magnetic behaviour of any system.

In the past thirty years some research into linear variable inductors has been conducted. However no model has been found to predict the inductance variation capability of VIs, in advance. This has brought several problems to VI designers, since they had to build the VI first and, only then, test its inductance variation. This constitutes a major drawback in in the choice of the variable inductor technology over others. In this master thesis an improved reluctance model that solves this classic problem is presented. It also presents an improved design methodology that calculates the VI parameter configuration that best fits the user desires. Finally, a software model of this improved design methodology is showed. The software allows any designer to know the best configuration for their VI in just few minutes, or even seconds.

Key words: variable inductors, variable inductance, electromagnetic analysis, reluctance model, saturated reluctance model, magnetic permeability, magnetic saturation, differential permeability, non-linear materials, multi-winding non-linear magnetic systems, finite element analysis, incremental permeability.

RESUMO

Nos últimos anos, as normas de eficiência energética e a procura por sistemas de controlo de energia mais eficientes têm aumentado a investigação sobre bobinas variáveis. Como o próprio nome indica, uma Bobina Variável (BV) é um dispositivo capaz de variar a sua própria indutância.

Esta tese apresenta uma análise eletromagnética detalhada sobre o funcionamento de Bobinas Variáveis Lineares (BVL) de núcleo duplo tipo E. Na topologia estudada, é usada uma corrente DC para controlar a indutância da BV através de uma série de fenómenos eletromagnéticos. Para estudar o comportamento eletromagnético é usado um Software de Elementos Finitos (SEF). Para isso são construídos e estudados, no *software*, modelos em 3D da BV. Os resultados obtidos pelo SEF são analisados e comparados com os resultados de outros modelos de BVs e com resultados experimentais.

Nesta tese também é feita uma crítica ao conceito de permeabilidade magnética. Esta demonstrou ser inadequada para analisar corretamente circuitos magnéticos não lineares que tenham mais do que uma fonte magnetomotriz. Verificou-se que a solução passa por substituir o conceito de permeabilidade magnética por permeabilidade magnética diferencial, que por sua vez demonstrou ser a propriedade que melhor caracteriza o comportamento magnético de qualquer sistema.

Nos últimos trinta anos tem-se realizado alguma investigação no campo dos BVLs. Contudo, não foi encontrado nenhum modelo capaz de prever, com antecedência, o valor da variação da indutância de uma BV. Isto tem trazido vários problemas aos projetistas de BVs, uma vez que estes têm de montar a bobina em primeiro lugar e só depois testar a sua variação de indutância. Este processo representa uma grande desvantagem na escolha desta tecnologia em vez de outras. Nesta tese de mestrado é apresentado um modelo de relutância melhorado que resolve este problema clássico. Também apresenta uma metodologia de construção capaz de calcular a configuração de parâmetros da BV que melhor se adequa à necessidade do projetista. Por último, é mostrado um modelo de software baseado nesta metodologia. O software possibilita a qualquer pessoa projetar uma BV com as características desejadas em apenas alguns minutos ou até segundos.

Palavras Chave: bobina variável, indutância variável, indutor variável, análise eletromagnética, modelo de relutâncias, permeabilidade magnética, saturação magnética, permeabilidade diferencial, materiais não lineares, elementos finitos, permeabilidade incremental.

ACRONYMS

3C85	*Model name of a ferromagnetic material*
AC	*Alternating current*
EF25	*Model name of a ferromagnetic E-shaped core with 25mm length*
EFD25	*Model name of a ferromagnetic E-shaped core with 25mm length*
ETD49	*Model name of a ferromagnetic E-shaped core with 49mm length*
FEA	*Finite Element Analysis*
FEM	*Finite Element Method*
H-field	*Magnetic Field*
IT	*Instituto de Telecomunicações – Telecomunications Institute of Coimbra's University*
LCR	*Initials for: Inductance (L), Capacitance (C), Resistance (R)*
LED	*Light Emitting Diode*
LVI	*Linear Variable Inductor*
MMF	*Magnetomotive Force*
N87	*Model name of a ferromagnetic material*
RSCC	*Resonant Switched Capacitor Converter*
RF	*Radio Frequency*
TPI	*Toroidal Power Inductors*
VI	*Variable Inductor*

LIST OF SYMBOLS

a	*Dimensionless variable for to adjust the curvature level of the B(H) curve function*
A_e	*Effective magnetic cross section area* $[m^2]$
A_{cu}	*Copper cross sectional area occupied of the wire* $[m^2]$
A_{cw}	*Core window area* $[m^2]$
A_g	*Cross section area of the central arm of the air-gap* $[m^2]$
A_i	*Cross section area of the magnetic path* i $[m^2]$
A_{DC}	*Cross sectional area occupied by the copper of DC winding* $[m^2]$
A_{main}	*Cross sectional area occupied by the copper of main winding* $[m^2]$
A_o	*total winding occupation area* $[m^2]$
B(H)	*Magnetization curve*
$\mathbf{B}$; B	*Magnetic flux density vector; magnetic flux density* $[T]$
$B_{\max}$	*Maximum value of the magnetic flux density*
B_{sat}	*Magnetic flux density for saturated conditions* $[T]$
C_o	*Output Capacitor* $[F]$
C_r	*Resonant Capacitor* $[F]$
dB ; $\mathbf{dB}$	*Flux density element; flux density vector element with magnitude* dB $[\mathrm{T}]$
$\mathbf{dD}$	*Infinitesimal vector element of the electric flux density* $[C \cdot m^{-2}]$
d_{DC}	*Diameter of the DC winding wire* $[m]$
dH	*Magnetic field intensity element* $[A.m^{-1}]$
di	*Electric current element* [A]
$\mathbf{dl}$	*Infinitesimal vector element of the electric circuit contour* $[m]$
d_{main}	*Diameter of the main winding wire* $[m]$
dS ; $\mathbf{dS}$	*Surface element; vector with magnitude* dS *and direction normal to surface element* dS $[m^2]$
dt	*Time element* $[s]$
dV	*Volume element* $[m^3]$
$d\psi$	*Magnetic flux element* $[Wb]$
$\mathbf{D}$; D	*Electric flux density vector; Electric flux density* $[C \cdot m^{-2}]$
D	*Duty Cycle*
$\mathbf{E}$	*Electric field vector* $[V \cdot m^{-1}]$
emf	*Electromotive force* $[V]$
f_s	*Switching frequency* $[Hz]$

h	*Height of the coil* [m]
H ; $\mathbf{H}$	*Magnetic field intensity; Magnetic field vector* $[A \cdot m^{-1}]$
H_a	*Dimensionless variable used to simplify the representation of the B(H) curve equation*
H_{ac}	*Alternating magnetic field* $[A \cdot m^{-1}]$
H_{DC}	*Static magnetic field* $[\mathrm{A \cdot m^{-1}}]$
i	*Instantaneous electric current* $[A]$, *number of the path*
i_{DC}	*Instantaneous electric current of the DC windings* $[A]$
$i_{\mathrm{DC\_max}}$	*Maximum electric current value of the DC windings* $[A]$
$id\vec{S}$	*Infinitesimal current source normal to the wire cross section area* S $[A]$
i_{enc}	*Encircled current flowing on a circular winding* $[A]$
i_{main}	*Instantaneous electric current of the main winding* $[A]$
$i_{\max}$	*Maximum electric current value* $[A]$
int()	*Round down integer function*
$\mathbf{J}$	*Electric current density vector* $[A \cdot m^{-2}]$
J_s	*Magnetic polarization at saturation* $[T]$
k	*Arbitrary value*
K_u	*Filling factor*
K_{u_FEA}	*Filling factor associated to the FEA software*
L	*Inductance* $[H]$
L_{avg}	*Average inductance value* $[H]$
$L_{idc=0A}$, $L_{idc=0.7A}$, $L_{idc=1.5A}$	*Inductance value when the current of DC windings is 0A, 0.7A and 1.5A respectively.*
$L_{\max}$	*Maximum value of the inductance* [H]
$L_{\min}$	*Minimum value of the inductance* [H]
l_{core}	*Length of the magnetic path of the core* $[m]$
L_{main}	*Inductance of the main winding* [H]
L_r	*Resonant inductance value. The same as* L_{main} [H]
l_i	*Length of the magnetic path* i $[m]$
l_e	*Effective magnetic path length* $[m]$
l_{ext}	*Length of the external path of the core* $[m]$.
l_{gap} ; l_g	*Length of the air-gap* $[m]$
l_{sat_i}	*Length of the saturated area of the magnetic path* i $[m]$
l_w	*Length of the core window* $[m]$
mmf	*Magnetomotive force* $[A \cdot turns]$
N	*Number of turns of a winding*

N_{DC}	*Number of turns of the DC windings*
N_{main}	*Number of turns of the main winding*
P	*Point*
Q_{enc}	*Amount of electric charge inside the volume* V $[C]$
$r\,;\hat{r}$	*Length between the inducted point P and the wire, radius of the wire; Length unit vector* $[m]$
r_{cu}	*Radius of the copper cross section of the wire* $[m]$
r_{main}	*Radius of the wire of the main winding* $[m]$
RT	*Initials for Ratio. It is the quotient between the maximum and minimum inductance values*
$\Re$	*Reluctance* $[A \cdot Wb^{-1}]$
$\Re_g$	*Reluctance associated to the path air-gap* $[A \cdot Wb^{-1}]$
$\Re_i$	*Reluctance associated to the path* i $[A \cdot Wb^{-1}]$
$\Re_{sat}$	*Reluctance for saturated conditions* $[A \cdot Wb^{-1}]$
$\Re_{sat\_i}$	*Reluctance for saturated conditions associated to the path* i $[A \cdot Wb^{-1}]$
$\Re_{total}$	*Global reluctance of the magnetic circuit* $[A \cdot Wb^{-1}]$
S	*Boundary area of volume* V $[m^2]$
T_s	*Time step* $[s]$
V	*Arbitrary volume with an* S *boundary* $[m^3]$
V_{in}	*Input voltage* $[V]$
V_{out}	*Output voltage* $[V]$
$v(t)$	*Electromotive force time function* $[V]$
χ	*Length of the gap between the windings and the core* $[m]$
ΔB	*Amount of variation of the magnetic flux density* $[T]$
ΔH	*Amount of variation of the magnetic intensity field* $[\mathrm{A.m^{-1}}]$
Ψ	*Magnetic flux* $[Wb]$
Ψ_{coil}	*Magnetic flux inside a coil* $[Wb]$
Ψ_{DC}	*Total magnetic flux of the DC windings* $[Wb]$
Ψ_{main}	*Magnetic flux on the main winding* $[Wb]$
μ	*magnetic permeability* $[\mathrm{H \cdot m^{-1}}]$
μ_d	*Differential magnetic permeability* $[\mathrm{H \cdot m^{-1}}]$
μ_{ds}	*Differential magnetic permeability for saturated conditions* $[\mathrm{H \cdot m^{-1}}]$
μ_{eff}	*Effective magnetic permeability* $[\mathrm{H \cdot m^{-1}}]$
μ_i	*Initial magnetic permeability* $[\mathrm{H \cdot m^{-1}}]$
$\mu_{kB_{sat}}$	*Permeability of the core for* $i_{dc\_\max}$ *and zero ac current* $[\mathrm{H \cdot m^{-1}}]$
μ_r	*Relative magnetic permeability* $[\mathrm{H \cdot m^{-1}}]$
μ_{ri}	*Relative initial magnetic permeability* $[\mathrm{H \cdot m^{-1}}]$

μ_{r_ds}	*Relative differential magnetic permeability for saturated conditions*
μ_0	*Vacuum magnetic permeability* $[\mathrm{H}\cdot\mathrm{m}^{-1}]$
μ_{sat}	*Magnetic permeability for saturated conditions* $[\mathrm{H}\cdot\mathrm{m}^{-1}]$
μ_Δ	*Incremental permeability* $[\mathrm{H}\cdot\mathrm{m}^{-1}]$
λ_{wl}	*Wire length by unit of weight* $[\mathrm{m.kg^{-1}}]$
ρ_e	*Electric Resistivity value* $[\Omega\cdot m]$
ρ_m	*Mass density value*$[\mathrm{kg.m^{-3}}]$
ρ_v	*Electric charge density* $[\mathrm{C.m^{-3}}]$
ς_{wlr}	*Electric resistance by length of wire* $[\Omega.\mathrm{m^{-1}}]$
τ	*Thickness of the winding* [m]
τ_{main}	*Thickness value of the main winding* [m]
τ_{DC}	*Thickness value of the DC winding* $[m]$
$\nabla\cdot$	*Divergence operator*
$\nabla\times$	*Rotational operator*

TABLE OF CONTENTS

LIST OF FIGURES

LIST OF TABLES

CHAPTER 1 – Introduction

This chapter will provide a brief introduction to Variable Inductors. General considerations about their application and the relevance of an electromagnetic study of the devices is presented. For the purpose of the electromagnetic study, the selected finite element analysis software is presented and some basic equations are addressed. The motivation and main objectives are introduced. The chapter ends with an outline of the work.

1.1. The Variable Inductor

This work aims to demonstrate the behaviour of multiple winding magnetic devices, commonly known as variable inductors, through finite element analysis of a 3-D model. The obtained results are met with an experimental application of the device. The main objective of this thesis is the development of an appropriate design procedure for the variable inductor for future applications.

The variable inductor (VI) is not a recent magnetic device, and has been known since the 1930's. The first model consisted of varying mechanically the length of core's air-gap or the number of winding turns. Later, some models appeared with electronic switches to replace the mechanical interface. However, all these models only allowed a variation of the inductance between fixed predefined values. In 1987 Kislovski, proposed the first quasi-linear controllable inductor, which was later improved to become the Linear Variable inductor (LVI) [1]. The VI's mentioned in this work are referred to the LVI structure. In the late 1980's there was a large research demand around VI systems due to the market request for improved and more power effective electronic ballasts to control tubular fluorescent lamps. Nowadays, with the energy efficiency regulations becoming more and more demanding it is necessary to research new efficient ways to control power systems.

VIs can be used in several applications, and due to their coverage areas, it is possible to divide them into three categories, such as: high-power, mid-power applications, and telecommunications. In high-power applications variable inductors have been researched and used to control voltage variations in electric power systems through the regulation of reactive power [2], [3], and, more recently, to maximize power transfer in solar microgrids [4]. These applications are characterized by their low frequency (<1 kHz) and high power transfer (>1 kVA up to 100 kVA). In mid-power applications VIs have been used and researched to control

the output current of high-frequency resonant circuits [5]. The applications include control of electronic ballasts [6] and LED lighting control [7], [8]. In these applications, VIs are characterized for their high frequency of operation (1 kHz up to 100 kHz) and medium power transfer (10 VA up to 10 kVA). In telecommunications, VIs are widely used to regulate a circuit's impedance in order to have multiband control of radio frequency (RF) circuits [9]–[14]. The VI's used in these applications operate at very-high frequencies (>10 kHz up to dozens or hundreds of GHz) and have a very low power transfer (<10 VA).

This work will study one type of variable inductor applied to mid-power applications. Due to the mathematical complexity associated to the interpretation of electromagnetic effects, it is difficult to find a good model that mirrors the correct operation of VIs. Therefore, a finite element analysis (FEA) software will be used to solve this problem. A summary about the operation of this software is described below. The motivations, main objectives and outline of the work are presented in the end of this chapter.

1.2. The Finite Element Analysis Software

The FEA software is a program that applies the finite element method (FEM) to geometric objects. The FEM is a numerical technique to find approximate solutions for boundary problems associated with differential equations [15]. This method was initially introduced by Richard Courant in 1943 [16] but it was only in 1968 that Miloš Zlámal announced the first important results [17]. With the progress of technology, the FEA software has become a staple method for engineers and scientists to resolve complex electromagnetic problems [18]. The emergence of fast computing machines has allowed the processing of difficult and complex calculus in a shorter time interval. There are many different types of FEA software. This work will use the Flux (by CEDRAT) which studies the electromagnetic effect in 2D or 3D models. The finite element method used by this software solves the Maxwell differential equations, which describes, mathematically, the effect of electromagnetic phenomena. The complexity of these equations are so great that even good mathematicians cannot apply them in anything but the simplest scenarios [19]. Therefore, the FEA software is needed to apply it in real scenarios.

1.2.1. Maxwell Equations

Between 1881 and 1882 James Clerk Maxwell published an early form of four single equations nowadays known as Maxwell's equations [20], [21]. Although he did not discover these, he found the link between them. These equation explain all the known electromagnetic behaviour

and are used by the FEA software. The FEM method applies these differential equations into modelled geometric figures to simulate the real life electromagnetic behaviour. A brief explanation of each equation is expressed below.

Equation 1: (Gauss's Law)

The first of Maxwell's equation, also known as the Gauss's Law in differential form, is shown below:

$$\nabla \cdot \mathbf{D} = \rho_v \tag{1.1}$$

where $\nabla \cdot$ is the divergence operator, $\mathbf{D}$ represents the electric flux density 3D vector [C/m^2], and ρ_v stands for electric charge density [C/m^3].

This equation shows that an isolated electric charge creates a divergent electric flux density with the direction and value of the charge. Therefore a positive charge creates an electrical flux density that "diverges away" from the charge and negative charge creates an electrical flux density that "diverges towards" the charge, as represented in Fig. 1.1.

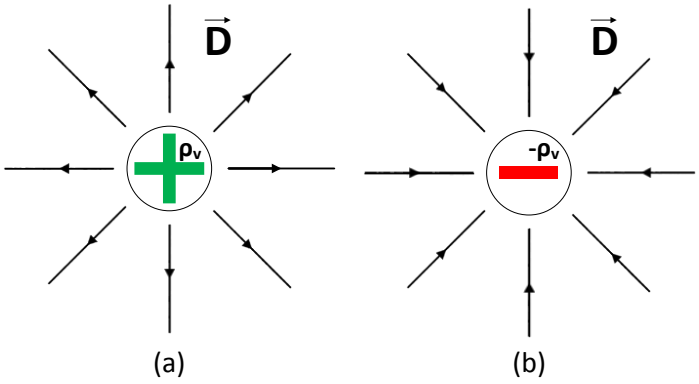

Fig. 1.1 Representation of the electric flux density distribution created by: (a) positive electric charge; (b) negative electric charge.

The integral form is shown in equation (1.2):

$$\int_V (\nabla \cdot \mathbf{D}) dV = \int_V \rho_v dV \Leftrightarrow \int_S \mathbf{D} \cdot \mathbf{dS} = Q_{enc} \tag{1.2}$$

where, V represents an arbitrary volume [m^3]; S symbolizes the boundary area of that volume in square meters [m^2]; $\mathbf{dS}$ is a vector with infinitesimal modulus corresponding to an infinitesimal area of the boundary and pointing outwards, normal to the differential area; and Q_{enc} stands for the total amount of electric charge inside the volume [C]. This equation shows that the total electric flux exiting a given volume is equal to the total electric charge inside. It also demonstrates that the only the component of $\mathbf{D}$ that contributes to the net electric flux in or out the volume is normal to the area S.

Equation 2: (Gauss's Law for Magnetism)

Maxwell's second equation also known as the Gauss law's for magnetism in differential form is presented below:

$$\nabla \cdot \mathbf{B} = 0 \tag{1.3}$$

where $\mathbf{B}$ is the magnetic flux density vector [T]. This equation demonstrates that there is no divergence in magnetic flux density. This is due to the non-existence of isolated magnetic poles. Each magnetic field is created by two opposite poles called dipoles that can never be split. A better understanding of this law may come with the integral form of this equation:

$$\int_V (\nabla \cdot \mathbf{B}) dV = 0 \Leftrightarrow \oint \mathbf{B} \cdot \mathbf{dS} = 0 \tag{1.4}$$

Equation (1.4) states that the sum of all magnetic flux density flowing in or out of any closed surface has to be zero.

Equation 3: (Faraday's Law)

Equation (1.5) contains the third of Maxwell's equation also known as the Faraday's Law in its differential form:

$$\nabla \times \mathbf{E} = -\frac{\partial \mathbf{B}}{\partial t} \tag{1.5}$$

where $E(r,t)$ is the electrical field [V.m^{-1}] , and $B(r,t)$ is the magnetic flux density [T].
This equation demonstrates the relationship between the time changing magnetic flux density and the electric field. It states that a variable magnetic flux density creates a variable perpendicular 3D rotational electric field with opposite polarity. The effect caused by the cross of this magnetic-generated electric field with an electric conductor is called induction. The induction creates an electro-motive force in coiled wires that can be calculated through the integration of equation (1.5) and the application of Stokes' Theorem, as shown below:

$$\begin{gathered} \iint_S \nabla \times \mathbf{E} \cdot \mathbf{dS} = -\frac{d}{dt} \iint_S \mathbf{B}(t) \cdot \mathbf{dS} \Leftrightarrow \oint_{circuit} \mathbf{E} \times \mathbf{dl} = -\frac{d\psi}{dt} \\ \Updownarrow \\ emf = -\frac{d\psi}{dt} \end{gathered} \tag{1.6}$$

where, $\mathbf{dl}$ is an infinitesimal vector element of the circuit contour [m], Ψ is the magnetic flux within the circuit [Wb], and emf is the electromotive force applied to the terminals of the coil [V].

Equation 4: (Ampere's Law)

Equation (1.7) contains the fourth of Maxwell's laws:

$$\nabla \times \mathbf{H} = \frac{\partial \mathbf{D}}{\partial t} + \mathbf{J} \tag{1.7}$$

where $\mathbf{H}$ is the magnetic field vector [A/m], $\partial \mathbf{D}/\partial t$ is the displacement current density vector [A/m^2], and $\mathbf{J}$ is the electric current density vector [A/m^2].

The introduction of the displacement current density was one of the greatest breakthroughs made by Maxwell and allowed him to fix the classical Ampere's Law. However, in magnetic applications this term is often ignored due to its insignificant value for "low" frequencies (below some dozens of GHz). In addition, it represents the variation of the electric charge without the flow of electric current. This event only occurs in very specific environments, such as a capacitor fed by a transient time voltage where there is a change of charge in the plates, but no current between.

Ignoring the displacement current effect, the equation (1.7) becomes equal to the Ampere's law in its differential form. It states that a flowing electric current creates a rotational magnetic field. It can be applied in coiled systems after the following integration:

$$\begin{aligned} \int_S (\nabla \times \mathbf{H}) \cdot \mathbf{dS} &= \int_S \mathbf{J} \cdot \mathbf{dS} \\ i_{enc} &= \int_S \mathbf{J} \cdot \mathbf{dS} \end{aligned} \tag{1.8}$$

where i_{enc} is the encircled current flowing on a circular winding with an S cross section surface.

1.2.2. Biot and Savart Law

Although the Biot and Savart Law is not a Maxwell equation, it is used by Flux software in order to simulate the magnetic field density of some specific coils (non-meshed coils[1]). This law has an inferior calculus complexity when compared to Maxwell's equations. However, it does not consider the eddy current effect and for that reason it is only used it in static applications (see simulation types on Chapter 3).

The Biot and Savart law can be defined as follows:

$$\mathbf{dB} = \frac{\mu_0}{4\pi} \frac{i \cdot \mathbf{dl} \times \hat{r}}{r^2} \tag{1.9}$$

[1] A Non-meshed coil is a type of coil which is not meshed (see chapter 3) allowing one to reduce the total simulation time. Besides it is easier to construct.

where, $\mathbf{dB}$ is the elemental flux density in a point P, $i \cdot \mathbf{dl}$ is the infinitesimal current source; r is the length, measured in meters [m], between the infinitesimal current source and the point P, $\hat{r}$ is the unit vector placed in the infinitesimal current source oriented to the point P, and μ_0 is the vacuum magnetic permeability measured in [N.A^{-2}]. Fig. 1.2 contain a graphical representation of these values.

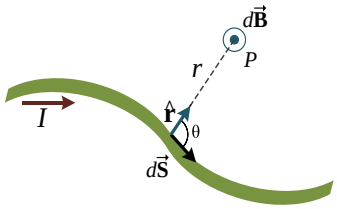

Fig. 1.2 – Representation of Biot and Savart vectors, applied on a electric wire (green line).

Equation (1.9) allows the software to calculate the magnetic influence of a current passing through a coil in a given point P.

1.3. Motivation and Main Objectives

The main motivation for this work is to learn and understand the electromagnetic operation of VIs with the help of FEA software capabilities. The variable inductor proved to be a good choice due to the increased research demand for this type of system in the research group at IT-Coimbra. Underneath, lies the importance of studying the electromagnetic behaviour of this application using the FEA software. The used software is a very powerful tool and has great prominence in present and future research. During the development of this work, a classic problem related to the modelling of VIs arose - there was no algorithm to know, in advance, the minimum inductance value of VIs. In the search for a solution, it was found a major problem related to the interpretation of the magnetic permeability concept. This problem is going to be addressed and solved in this work. The work developed during this dissertation is directed on pursuit of the following objectives:

→ To build a VI model in the FEA software that represents a real life model. To prove its reliability the operation results of the FEA model will be compared to the equivalent real life model presented in [22]. Having a reliable model is essential for the pursuit of the remaining objectives.

→ To perform a steady-state and time domain study to understand the electromagnetic behaviour of the variable inductor. Knowing the VI operation is essential to improve and develop future upgrades.

→ To analyse and compare the electromagnetic behaviour of different E-shaped[2] VI models.

→ To solve the classic problem of modelling a variable inductor, using the knowledge acquired in the previous steady-state and time domain studies. Until now, no appropriate solution or methodology has been presented that shows, in advance, the amount of inductance variation for a specific VI topology. This inductance variation is essential to determine the potential applications for the device.

→ As consequence of the previous objective it becomes necessary to study the magnetic permeability behaviour in multi-sourced non-linear magnetic applications.

→ To develop an improved algorithm that chooses the best design configuration to build a VI with the desired characteristics.

→ To create a software application using the previous algorithm, to provide access to each user to design its own VI in a quick and easy way.

1.4. Outline of the work

This Master thesis is divided into five chapters. The first chapter presents an overview of the variable inductor, the finite element analysis software, and the Maxwell differential equations. The motivation and main objectives of this work are then explained. Chapter 2 contains the basic magnetic notions needed to understand the operation of the VI, including the inductance, magnetic permeability, the ferromagnetic materials properties and the different types of cores used in VI studies. It also presents the VI operating principle, a commonly used VI design methodology and the different types of VI modelling. The next three chapters are the core of this thesis and are divided into the FEA construction model, the finite element analysis, and a proposal of a new VI design algorithm. Chapter 3 presents all the important steps related with the FEA construction model. Chapter 4 contains a thorough electromagnetic analysis of the VI operation resulting from the collected data acquired with the FEA software. The analysis is divided in two sections. The first section addresses the general electromagnetic behavior of the VI operation. The second section studies the dynamic electromagnetic behavior of the VI when inserted in a 100 kHz resonant switched-capacitor converter (RSCC). In Chapter 5 a new VI design algorithm is proposed. The concept of magnetic permeability is carefully analyzed and re-defined for non-linear magnetic materials. A more precise magnetic analysis is then

[2] E-shaped VI models are explained in the section "Types of magnetic cores" in Chapter2.

performed, leading to a new design methodology proposal. Chapter 6 contains the conclusion and future work. All the work described in these chapters is complemented with descriptions and materials provided in the Appendix.

The modelling steps and FEA analysis presented in the following chapters reference previous work done by M. Martins [22]–[24]. In his work, M. Martins implemented a Dimmable LED Driver based on a Resonant Switched Capacitor Converter using a VI based control technique. The implemented double EFD25 VI prototype serves as an experimental model. The ETD49 FEA used in Chapter 4 and Chapter 5, also references a constructed model by Valter Costa which is currently being used to study an alternative methodology to control the charging current of battery for electric vehicle applications. The work of this thesis differs from these two, and from any other published before in its presentation of an electromagnetic static and dynamic analysis of the VI's behaviour. Furthermore, it formulates a critical analysis to the classic magnetic permeability definition, discussing its limitations and presenting a solution that unlocks the capability to correctly study the operation of any magnetic multi-sourced non-linear system. It also presents a more effective way to design VI's that guarantees the desired inductance variation after its assembly.

CHAPTER 2 – Basic magnetic notions and VI operating principle

This chapter aims to transmit basic magnetic notions and properties necessary to the complete understanding of the variable inductor operation. It also describes its principle of operation and the design methodology. At the end of the chapter, three VI modelling methodologies are presented as well as their respective pros and cons.

2.1. Basic concepts of electromagnetism

In order to understand the operation of the variable inductor, it is necessary to know the classical concepts of inductance, magnetic permeability, the magnetic response and properties of ferromagnetic materials, and finally the type of magnetic cores available on the market. These subjects are addressed below.

2.1.1. Ferromagnetic materials

Ferromagnetic materials are known for their high magnetic permeability, and their value can be from hundreds to thousand times higher than the one for the air. This characteristic, and their relative low cost, makes them the most used materials in magnetic applications. They can be used as either permanent magnets or magnetic flux conductors. Two attributes of ferromagnetic materials are their non-linear magnetic response to H-fields and their hysteresis effect. Each material has a B(H) curve that defines its operation. The curve itself contains the information about the hysteresis and non-linear magnetic response. Fig. 2.1(a) shows an example of this curve.

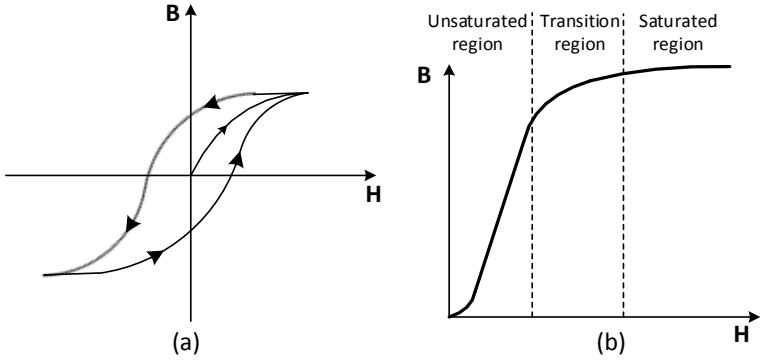

Fig. 2.1 – (a) Typical B(H) curve of non-linear material. (b) Typical magnetization curve of a soft magnetic material, without hysteresis.

For the majority of materials, the flux density is a function of the H-field. In ferromagnetic materials, it depends not only on the H-field but also on the previous magnetization state of the material. This phenomenon called hysteresis can be observed in Fig. 2.1 (a) by the width of the represented loop. Materials with a wide hysteresis curve are called "hard magnetic materials". These tend to hold their magnetization and are usually used to build permanent magnets. Those with a low hysteresis value are called "soft magnetic materials", and tend to easily lose their magnetization. These are commonly used as magnetic flux conductors. In this work, only soft magnetic materials are considered. Due to the complexity of the hysteresis integration in FEM applications, the FEA software does not yet compute this characteristic. The solution for soft magnetic materials, proposed by CEDRAT, is to ignore the hysteresis width since the error committed is very small. Nevertheless, the magnetic response is still non-linear, which makes the FEM calculus quite complex. From now on, the B(H) curve nomenclature in this work is referring to the initial magnetization curve for which hysteresis is absent.

The non-linearity effect can be observed in the curvature of each line in Fig. 2.1. For linear materials, the magnetic flux density is directly proportional to the H-field, and the B(H) representation is a straight line. For non-linear materials there is no direct proportionality between these two and for high H-fields the material saturates. Due to the non-linearity, the magnetization state of ferromagnetic materials is commonly classed as unsaturated, transition or saturated region, depending on the intensity of the H-field, as shown in Fig. 2.1(b).

2.1.2. Magnetic Permeability

The magnetic permeability, μ, is a common property that describes the ease with which the magnetic flux flows through a material [25]. The standard value is the vacuum magnetic permeability, $\mu_0 = 4\pi \times 10^{-7}\,\mathrm{A.m^{-1}}$. For all materials, it is common practice to relate their magnetic permeability to μ_0 through a parameter called relative magnetic permeability, μ_r, using the following equation:

$$\mu = \mu_0 \cdot \mu_r \tag{2.1}$$

The magnetic permeability relates the magnetic field H with the magnetic field density B, through the following equation:

$$B = \mu H \Leftrightarrow \mu = B/H \tag{2.2}$$

The permeability μ assumes a scalar constant value for linear systems. For the non-linear ones, it is a function of the magnetization state of the material as expressed below:

$$\mu(H) = B/H \tag{2.3}$$

The magnetic permeability in multi-winding non-linear systems will be thoroughly analysed in Chapter 5.

In systems where the magnetic flux flows through more than one type of material, it is common to address the "effective permeability" [26]. For the studied VI, it can be calculated according to the following equation (2.4):

$$\mu_{eff} = \frac{\mu_{ri}}{\frac{l_{gap}}{l_{core}} \cdot \mu_{ri} + 1}, \quad l_{core} \gg l_{gap} \quad \text{and} \quad \mu_{ri} \gg 1 \tag{2.4}$$

where l_{core} is the length of path of the magnetic flux in the core [m], l_{gap} is the length of the air-gap [m] and μ_{ri} is the relative initial magnetic permeability of the core $[\mathrm{H \cdot m^{-1}}]$. This equation assumes that there is no occurrence of magnetic saturation in the core and that the area of the cross section of the outer arms is approximately half the corresponding cross section in the centre arm. The equation compiles the equivalent permeability resulting from the combination of two materials with different permeability values into a single value. In the present case, the studied VI is assembled with ferromagnetic cores containing one single air-gap.

Another common term used for permeability is the incremental permeability μ_{Δ}. It is defined as an alternating magnetic field H_{ac} superimposed on a static magnetic field H_{DC} [27]. The hysteresis loop follows a minor loop path as can be observed in Fig. 2.2

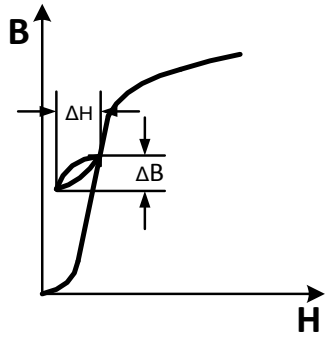

Fig. 2.2- Representation of the incremental permeability

The incremental permeability can be defined by equation (2.5):

$$\mu_{\Delta} = \frac{\Delta B}{\Delta H} \tag{2.5}$$

2.1.3. Inductance

Inductance is a common property of every conductor that characterizes its own inertia to the changing of the electric current. This property assumes great influence in coiled wires, making it one of the key factors in the winding operation. According to Maxwell's fourth

equation and neglecting the displacement current, any variation in the electric current of the coil generates a proportional variation of its own magnetic field intensity H. A time variating H-field generates a proportional variating magnetic flux density B for a constant permeability value. According to the third of Maxwell's laws ($\nabla \times \mathbf{E} = -\partial \mathbf{B}/\partial t$), a time changing flux density generates a negative electromotive force (*emf*) in the coil which opposes the variation of the current. The relationship between this counter *emf* and the current variation is the origin of the notion of inductance [28]. This property is measured in Henry [H], and can be calculated through the following formula:

$$L = \frac{\Psi_{coil}}{i_{enc}} \tag{2.6}$$

Where L is the value of the inductance, Ψ_{coil} is the total magnetic flux passing through the coil measured in Webber [Wb], and i_{enc} is the current that flows in the coil windings, measured in Ampere [A].

The inductance can be represented by the slope of the line formed by the total flux linkage and the current through the winding. Whereas linear inductors exhibit a constant inductance value during each period of the operating frequency, which implies a straight line through the origin of the flux-current plane, non-linear inductors are characterized by a different line, impossible to describe by a single number [29]. VIs are a specific type of non-linear inductors.

By integrating Maxwell's third equation and applying the Stokes' theorem it is possible to express the voltage across a current-controlled VI as presented in (2.7):

$$v(t) = -\frac{d\Psi(t)}{dt} = -\frac{d\Psi(i)}{di}\frac{di(t)}{dt} = -L(i(t))\frac{di(t)}{dt} \tag{2.7}$$

2.1.4. Types of magnetic cores

There are several different types of magnetic cores [30]. For the VI assembly in mid-power applications, it is common to use E-shaped forms. In Fig. 2.3 three different types of E-shaped cores are represented:

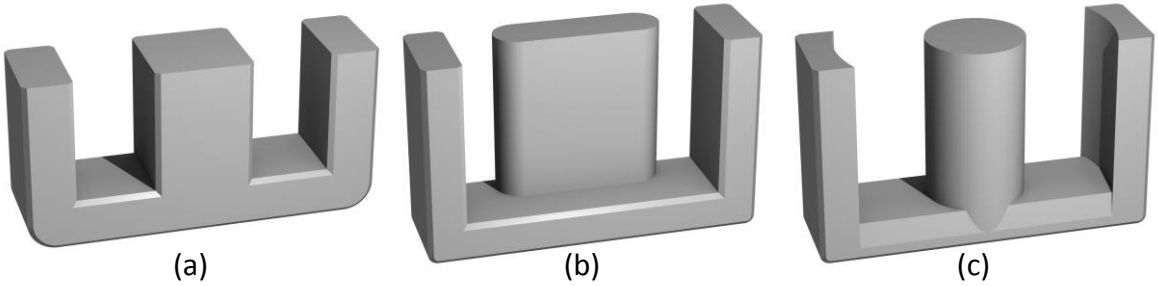

Fig. 2.3 – Different types of E-shaped cores. (a) E core; (b) EFD core; (c) ETD core. Images from [31]

The suitable E-shaped forms for VIs applications must have a cross section area in the centre arm equal to the sum of the cross sections of both outer arms.

It is also common to use toroidal powered inductors (TPI) in mid-power applications [7], [32], however this topology will not be analysed in this work.

2.2. VI operating principle

The variable inductors based on an E-shaped core contain three windings – two DC windings and a main winding. The principle of operation consists in varying the main winding inductance through the control of the flux created by the DC winding.

Fig. 2.4 (a) and (b) shows a schematic representation of the magnetic effect of each winding separately. Fig. 2.4 (c) represents the magnetic effect resulting in the assembly of all three windings in the core.

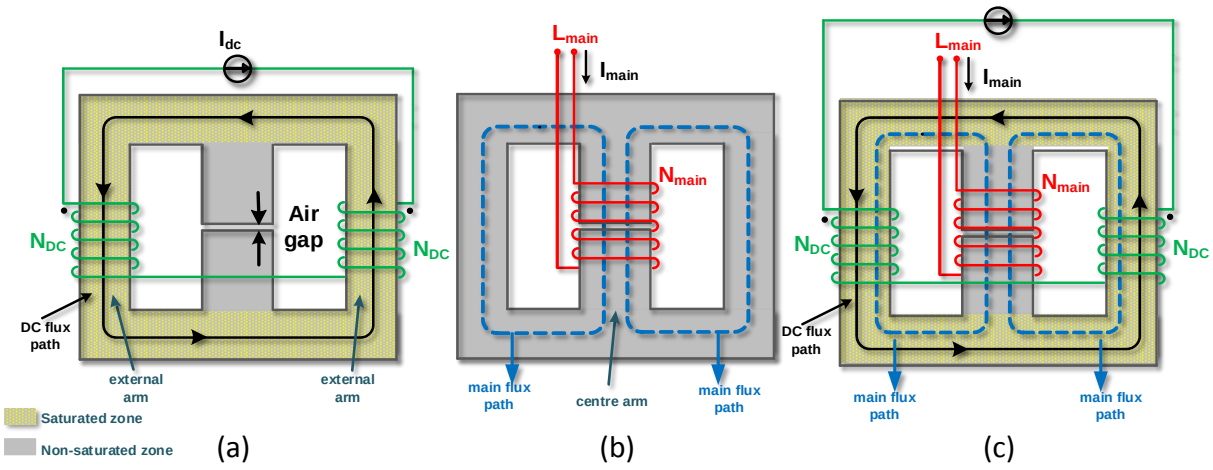

Fig. 2.4 – Assembly and magnetic contribution of the different windings in the variable inductor (a) DC windings assembly and magnetic contribution; (b) Main winding assembly and magnetic contribution; (c) Complete VI model with DC and main windings assembled.

Fig. 2.4 (a) shows a schematic of the magnetic contribution of DC windings, and its respective electric connection. These two windings are typically mounted in the external arms of the core, which are the ones without any air-gap. According to Maxwell's fourth law, a DC current flowing in a coil creates a constant magnetic field/flux. Therefore, with the presented configuration, the DC windings create a constant magnetic flux flowing around the core. The magnetic flux follows the direction of the represented DC flux path which is marked with black arrows. The inexistence of any air-gap within the path makes it easy to saturate. The operation of the variable inductor will rely on the saturation of this zone since it affects the local magnetic permeability. The yellow area represents the most probable area to be saturated by the DC

windings. In this work, the current and magnetic flux corresponding to the DC windings operation will be mentioned as DC current and DC flux respectively.

In Fig. 2.4(b), a schematic of the magnetic contribution of the main winding and the respective assembly zone is represented. As it can be observed, the main winding is typically mounted in the central arm of the core, which is the one containing an air-gap. The purpose of the air-gap is to lower the effective permeability which drastically reduces the magnetic flux produced. This configuration allows the users to create a design procedure that avoids the creation of any type of magnetic saturation in the centre arm since a higher value of $N_{main} \cdot i_{main}$ is needed to saturate the core. The inexistence of saturation in the centre arm is strictly necessary for the correct operation of the VI. Even so, the flux produced will always follow "the easiest path", represented with blue lines. In this work, the current and magnetic flux corresponding to the main winding operation will be named by main current and main flux respectively.

Fig. 2.4(c) contains the schematic representation of the magnetic contribution of the main and DC windings, and the respective assembly and connections. As is possible to observe there is a common path to both the main and DC flux paths. This common zone is key for the operation of the variable inductor.

With equation (2.3) it is possible to prove that an increase in the saturation level corresponds to a decrease in the permeability. Therefore, the saturation created by the DC winding will hinder the passage of the main flux through the common path zone. Furthermore, equation (2.6) states that for the same current, a reduction in the flux value of a coil results in the decrease of its own inductance. In this way, it is possible to handle the inductance variation through the current control of the DC windings.

Since the inductance is dependent on both amplitude of the main current, i_{main}, and value of the DC current, i_{DC}, the total flux linkage, $\Psi_{main}(t)$, seen by the main winding, can be defined as (2.8):

$$\Psi_{main} = f\left(i_{DC}, i_{main}\right) \tag{2.8}$$

2.3. Simplified design methodology of the VI

The following process is the most common for the VI design procedure [24]. It begins by selecting the core type and dimensions, and the desirable variable inductance range. The approach used is, in fact, a simplified approach, based on effective parameters of the magnetic cores employed. This procedure is suitable for VIs based on any E-shaped cores. The inductance of the main winding of the VI will be referred as L_{main}, and the current flowing through it will

be referred as i_{main}. For analysis purposes of the DC winding, the current flowing through it will be referred as DC current i_{DC}. As initial conditions, it is established that the maximum inductance value, $L_{\max}$, should be obtained for zero DC current (i_{DC}): $i_{DC}=0 \rightarrow L_{\max}$ and thereby, the minimum inductance value $L_{\min}$ should be obtained for a maximum value of DC current ($i_{DC\_\max}$): $i_{DC\_\max} \rightarrow L_{\min}$.

The maximum inductance value, $L_{\max}$, can be obtained by using the classic inductor equation and simplified approach as introduced in (2.9).

$$L_{\max}=\frac{N_{main}^2}{\Re_{total}}=\frac{N_{main}^2}{\frac{l_e}{\mu_r\cdot\mu_0\cdot A_e}+\frac{l_g}{\mu_0\cdot A_e}} \tag{2.9}$$

where $\Re_{total}$ is the global reluctance of the magnetic circuit as seen from the main winding [A/Wb], A_e is the effective magnetic cross section area [m²], l_e is the effective magnetic path length [m], l_g is the air-gap length [m], μ_0 is the magnetic permeability of the vacuum [H/m], and μ_r is the relative magnetic permeability of the core material. In the present situation this is equal to the initial permeability[3] [H/m]. Usually the E-shaped core manufacturer provides the corresponding approximation values for A_e and l_e.

The minimum inductance value $L_{\min}$ cannot be calculated since equation (2.3) cannot be used to calculate the permeability in multi-winding systems. A proposal to solve this problem will be introduced in Chapter 5.

The design should also adhere to a maximum constraint which is related to the permissible peak value of the main current, $i_{\max}$, flowing through the main winding. At this point, it is desirable to operate the centre arm at the peak value of the magnetic flux density $B_{\max}$, which must be lower than the saturation value B_{sat}. The relation (2.10) shall be applied.

$$B_{\max}\approx\left[0.1B_{sat};0.3B_{sat}\right] \tag{2.10}$$

The simplified design procedure by which the number of turns of each winding, N_{main} and N_{DC}, are selected is described as follows. The first step is the selection of the magnetic cores and then the identification of their parameters A_e, l_e. The next step is to set the required maximum inductance value $L_{\max}$ slightly higher than the value required by the specific application (corresponding to $i_{DC}=0$). In this case, the peak value of the magnetic flux density

[3] The initial permeability is the permeability of a demagnetized magnetic material for low values of H. Many manufacturers will give this value, however it might correspond to the permeability in the first magnetization of the material for a low H-field. In order to get an accurate value, I recommend the measurement of the slope of the B(H) curve for unsaturated conditions. The measured value might be three to four times higher.

in the centre arm $B_{\max}$ can be easily calculated using the peak value of the main current $i_{\max}$, as given by (2.11).

$$B_{\max} = \frac{N_{main}}{\Re_{total} \cdot A_1} \cdot i_{\max} \tag{2.11}$$

Using equation (2.10) and the selected value of L_{max}, (2.11) may be rewritten which results in equation (2.12), which in turn gives the number of turns for the main winding.

$$N_{main} = \frac{L_{\max} \cdot i_{\max}}{B_{\max} \cdot A_1} \tag{2.12}$$

The air-gap value g may, then, be obtained from equation (2.13).

$$l_g = \frac{\mu_0 \cdot N_{main}^2 \cdot A_1}{L_{\max}} - \frac{l_e}{\mu_r} \tag{2.13}$$

To estimate the number of turns of each DC winding N_{DC} , it is necessary to consider that the external path of the core's assembly must reach saturation at a stipulated maximum value of the DC control current. This leads to:

$$\Psi_{DC} \cdot \Re_{ext} = 2 \cdot i_{\mathrm{DC\_max}} \tag{2.14}$$

where $\Re_{ext}$ is the reluctance of the external path of the core. Recalling that the maximum value of the DC current i_{DC_max} for which the minimum main inductance value, L_{min}, is obtained, N_{DC} can be acquired by re-writing equation (2.14) as follows:

$$N_{DC} = \frac{1}{2} \frac{k \cdot B_{sat} \cdot l_{ext}}{\mu_{kB_{sat}} \cdot \mu_0 \cdot i_{\mathrm{DC\_max}}} \tag{2.15}$$

where:

l_{ext} - Length of the external path of the core [m].

$k \cdot B_{sat}$ - Flux density in the external path due to $I_{\mathrm{DC\_max}}$ for a zero main current [T].

$\mu_{kB_{sat}}$ - Permeability of the core for $I_{\mathrm{DC\_max}}$ and zero ac current [H.m^{-1}].

For $i_{\mathrm{DC\_max}}$ the core is expected to be near saturation, which means that the permeability value will be low. This design procedure is only a simplified approach due to the difficulty to evaluate the change in the permeability or reluctance of the core. The selection of B_{sat} also has a significant impact on the calculation of the inductance reference value. Experimental observation has shown that k should be around 80%. However, depending on the selected magnetic material, the prototype may need a few adjustments in the number of turns. It is also necessary to confirm that the number of turns of the DC and main windings fits in the available space of the core. Therefore the following equation must be used:

$$l_w = \tau_{main} + \tau_{DC} \tag{2.16}$$

where, l_w is the core window length, τ_{main} and τ_{DC} are the thickness[4] values of the main and DC windings respectively.

2.4. VI modelling

Modelling is essential for a correct understanding of the variable inductor behaviour. Typically, there are three different approaches for modelling complex magnetic devices such as multi-winding devices or integrated magnetics:

- *Gyrator-capacitor model* [33]: this technique is based on the employment of a capacitor to simulate the magnetic device. In the gyrator-capacitor approach, the magnetomotive force, mmf, is analogous to voltage and the rate-of-change of magnetic flux is analogous to current, which resembles the duality principle of the classic reluctance model. The gyrator-capacitor approach is considered an effective technique but it is rarely used.
- *Magnetic reluctance model*: This model is by far the most used in VI design, as shown in the previous section. It is simple and offers a more or less accurate method to calculate the inductance value. It begins by establishing a relatively complicated reluctance model of the structure [34] . Fig. 2.5 (a) shows the definition used for the magnetic paths which together make up the device. Each magnetic path i is related to a specific reluctance $\Re_i$ defined by:

$$\Re_i = \frac{l_i}{\mu_{pi} \cdot A_i}, \; i = 1...10 \tag{2.17}$$

where l_i is the length of the magnetic path i [m], A_i is the cross section area of the magnetic path i [m²] and μ_{pi} is the permeability of the magnetic path i [H/m].

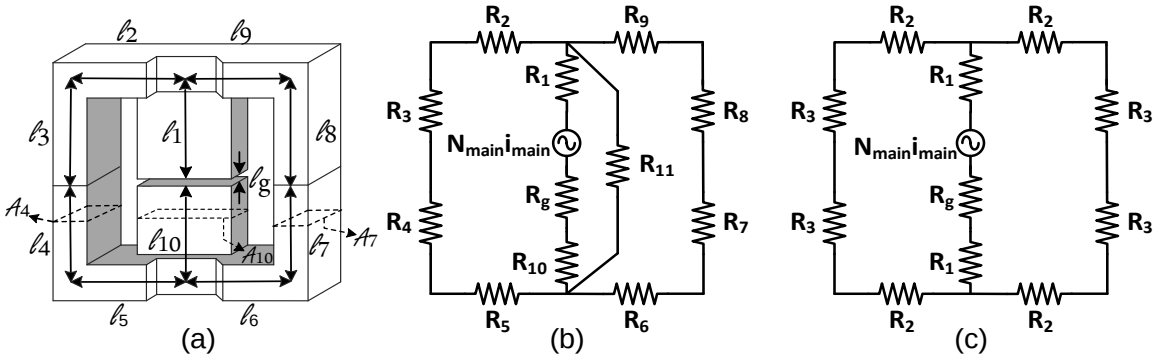

Fig. 2.5 - VI reluctance model: (a) Gapped EFD core; (b) Reluctance model; (c) Equivalent reluctance model

[4] The calculation of the thickness is explained in the coil construction section of Chapter 3.

Fig. 2.5 (b) shows the equivalent-reluctance model circuit where the main winding appears as an mmf source. No DC mmf source (corresponding to the DC winding) is included in the model. The effect of the DC windings is, in fact, already introduced in the model since the DC current affects the permeability, and thereby the reluctance, of the relevant path. The following quantities are especially defined: N_{main} is the number of turns of the main winding [turns]; $N_{main} \cdot i_{main}$ is the *mmf* source associated with the main winding $[A \cdot turns]$; $\Re_i$ is the reluctance of the element in the magnetic path associated to the main winding flux [A/Wb]; $\Re_{11}$ is the reluctance of the magnetic path associated with the leakage flux (flux lines that close in the air) [A/Wb]; and $\Re_g$ is the reluctance associated with the air-gap [A/Wb]. Due to the core's symmetry it is possible to simplify the model as shown in Fig. 2.5(c). The simplification takes into account the following equalities:

$$\Re_2 = \Re_5 = \Re_6 = \Re_9 \tag{2.18}$$

$$\Re_3 = \Re_4 = \Re_7 = \Re_8 \tag{2.19}$$

$$\Re_1 = \Re_{10} \tag{2.20}$$

The reluctance associated to the leakage flux is difficult to estimate. However, its value is typically much higher than any other presented in the model. As it is in parallel with the remaining reluctances, it is common to neglet it. Therefore, using the basic equation of an inductor, the main inductance can be determined as shown in the following equation (2.21):

$$L_{main} = \frac{N^2}{\Re} = \frac{N_{main}^2}{\Re_g + 2 \cdot \Re_1 + \Re_2 + \Re_3} \tag{2.21}$$

The former is valid if the left and right contour of the main flux lines encounters the same reluctances, in spite of different H-levels. It demonstrates that the inductance varies as function of the permeability of the core, a function of the magnetic field intensity H_{DC}, which in turn is a function of the control current i_{DC}. Since this analysis includes non-linear magnetic materials, this is a quite difficult subject[5]. The solution is to perform additional modelling of the VI through FEA.

- *Finite element analysis model*: this model is, by far, the most acurate. There are several software packages available to perform this modelling and obtain the behaviour of the magnetic device. The software uses Maxwell's equations to calculate the electric or magnetic field distribution for any geometric 3D model. It allows the user to calculate and visualize several parameters as the magnetic flux density, permeability, current density, conductivity, resistivity, power or thermal losses, and others.

One of the objectives of this work is to use this last modelling technique to understand the behaviour of the VI and to provide an accurate design project of the device. A good design project is a great asset in the avoidance of future amendments. The modelling steps and FEA analysis are presented in the following two chapters.

CHAPTER 3 – FEA-Model construction

This chapter explains the procedure required to construct a VI model in the Flux (by CEDRAT) software. It shows that the construction of a VI model in the FEA software relies on the fulfilment of several steps, such as the core and coil construction, the correct choice of simulation type, the mesh build, the material assignment, and the construction of an Infinity box. The most important steps necessary to construct a reliable FEA VI model are addressed, and their application to any E-shaped VI is demonstrated. This chapter also contains the construction parameters for the studied EFD25 VI model, as well as all the necessary equations.

3.1. Core-model construction

The 3D core model of the EFD25 VI was constructed using the FEA software. The VI core is composed by 2 EFD25 pieces. The pieces are mounted in opposite directions as shown in Fig. 3.1 (a) and (b), and create an air-gap within, located in the centre arm (shown by the blue area). Fig. 3.1 (c) and (d) contains the front and rear views of the two EFD25 pieces.

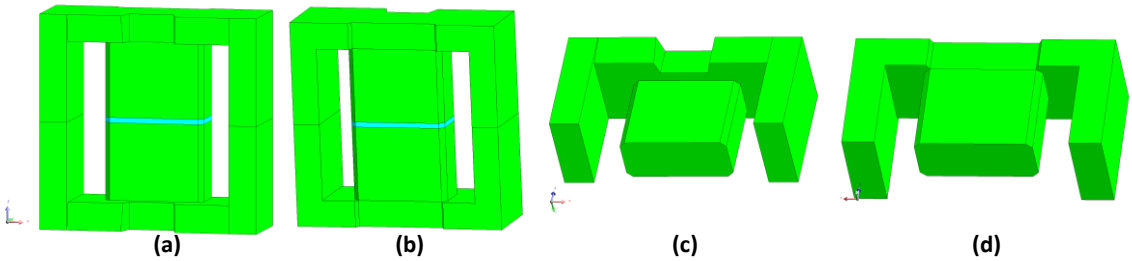

Fig. 3.1 – FEA software EFD25 core model. (a) front view of VI core; (b) rear view of VI core; (c) lower-front view of one EFD25 piece; (d) lower-back view of one EFD25 piece

Each 3D figure is composed by volumes, faces, lines, and points and can be represented in a Cartesian, cylindrical, or spherical coordinate system. The distance between each point is calculated using the values present in the datasheet or through manual measurement.

The dimensions used in the EFD25 VI core's construction are shown in Fig. 3.2 and TABLE 1.

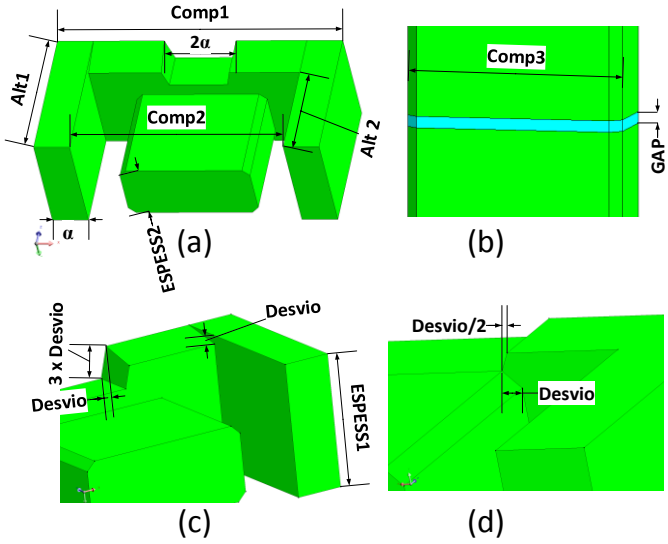

Fig. 3.2 Dimensions of the EFD25 core. (a) front and down view; (b) centre arm macro; (c) Zoom in the front view; (d) Zoom in the back view

TABLE 1
DIMENSION VALUES FOR THE EFD25 VI CORE

Variable Name	Dimension [mm]	Acquirement Method
ALT1	12.5	Datasheet
ALT2	9.3	Datasheet
COMP1	25	Datasheet
COMP2	18.7	Datasheet
COMP3	11.4	Datasheet
DESVIO	0.6	Measurement
ESPESS1	9.1	Datasheet
ESPESS2	5.2	Datasheet
GAP	0.6	Measurement

The use of variables instead of numbers enables the user to build any VI core with different dimensions just by changing its values. That way new VIs using the same type of core can be built easily in the future. In this work two other cores were used. The cores' dimensions can be found in Appendix A.

3.2. Coil-model construction

It is possible to build either meshed or non-meshed coils with FEA software. Meshed coils are difficult to build and the magnetic contribution to the system depends on the quality of the mesh. Although non-meshed coils are easier to build, their shape is limited to some predefined types of coils. The geometry of these coils is independent of the mesh, allowing the software to calculate the magnetic field through the Biot and Savart law instead of using Maxwell's more complex equations, resulting in the reduction of the total simulation time. For this application, non-meshed coils were used.

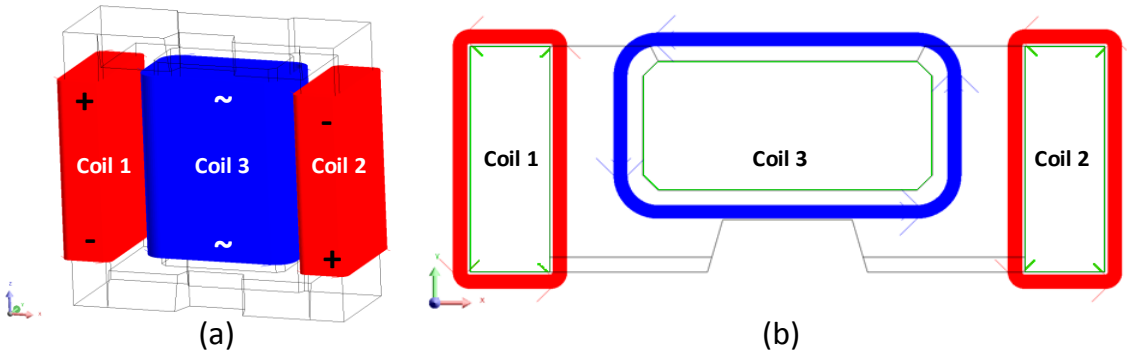

Fig. 3.3 - 3D non-meshed coil models built in FEA software. (a) Front view (b) Top view

Fig. 3.3 presents the locations of the non-meshed coil models. The DC windings are represented by the colour red and the main winding by the colour blue. The arrows around the windings in Fig. 3.3 (b) represent the direction of the positive current flow. In order to work as a variable inductor, the magnetic flux created by this current requires the DC windings to be symmetrically supplied. This means that these windings must be electrically connected in opposite polarity (anti-series).

The diameter of the wire for the main winding d_{main} may be selected using equation (3.1):

$$J_{main} = \frac{I_{\max}}{S} = \frac{I_{\max}}{\pi \cdot r_{main}^2} = \frac{I_{\max}}{\pi \cdot \left(\frac{d_{main}}{2}\right)^2} \Leftrightarrow d_{main} = \sqrt{\frac{4 \cdot I_{\max}}{\pi \cdot J_{main}}} \tag{3.1}$$

where $I_{\max}$ is the rms current value [A], J is the selected rms current density [A/m^2], S is the cross section of the wire [m^2] and r_{main} is the radius of the cross section of the wire [m]. Analogously the diameter d_{DC} of the wire for the control winding may be selected using equation (3.2):

$$d_{DC} = \sqrt{\frac{4 \cdot I_{\mathrm{DC\_max}}}{\pi \cdot J_{DC}}} \tag{3.2}$$

The filling factor of the windings K_u is defined by being the quotient between the total winding occupation area A_o [m^2] and the core window area A_{cw} [m^2] which can be defined by the following expressions:

$$K_u = \frac{A_o}{A_{cw}} \tag{3.3}$$

$$A_o = A_{main} + A_{DC} \tag{3.4}$$

$$A_{cw} = \frac{(\mathrm{comp2} - \mathrm{comp3})}{2} \cdot \mathrm{alt1} \tag{3.5}$$

where A_{main} [m^2] and A_{DC} [m^2] are the cross sectional areas occupied by the copper of main and DC coils respectively, and $\mathrm{comp2}$ and $\mathrm{comp3}$ are the dimensions in [m] represented in Fig. 3.2.

In FEA software the filling factor K_{u_FEA} represents the proportion of the copper area in the total coil area. For each winding, this can be defined by:

$$K_{u\_FEA} = \frac{N \cdot A_{cu}}{h.\tau} = \frac{N \cdot \pi \cdot r_{cu}^2}{h.\tau} \tag{3.6}$$

where h [m] and τ [m]are the coil height and thickness[5], and r_{cu} [m] is the wire copper radius which is given by the factory. The height of the coil h depends on the core dimensions. The thickness τ depends on the conductor radius, number of turns, and on the selected wire displacement. In this work the hexagonal fitting wire displacement introduced by Bossche and Valchev [27] was chosen. Fig. 3.4 represents an example of the cross-sectional area of a coil following the hexagonal fitting.

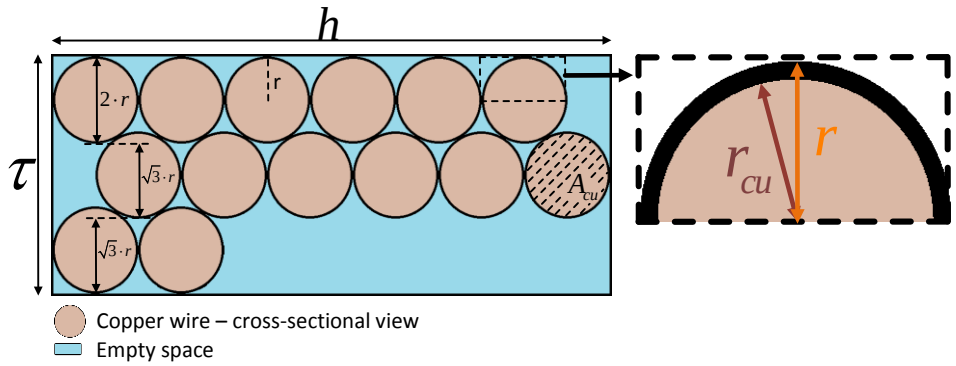

Fig. 3.4 – Representation of a coil winding area, and respective associated variables and dimensions. The windings of the coil follows the hexagonal fitting. The right side shows the zoom of half wire, highlighting the differences between the wire radius and copper radius.

The following equation was implemented to calculate the coil thickness τ:

$$\tau = \left\{ \text{int}\left[\frac{N}{\text{int}\left(\frac{h}{r}\right)} + 0.99(9) \right] - 1 \right\} \cdot r \cdot \sqrt{3} + 2r \tag{3.7}$$

where:

int() is the rounded down integer function;
$2r$ is the thickness of the first layer ;
$r \cdot \sqrt{3}$ is the thickness of each one of the remaining layers, as shown in Fig. 3.4.
$\text{int}\left(\frac{h}{r}\right)$ is the number of turns that fit by layer;
$\text{int}\left[\frac{N}{\text{int}\left(\frac{h}{r}\right)} + 0.99(9) \right]$ is the total number of layers of the coil;

[5] The number of turns of each winding might not completely fill the last layer. In the FEA software the non-meshed coils must have a uniform shape, whereby the thickness value must include the incomplete layer. The error committed is balanced by the filling factor.

$\left\{ \text{int}\left[\frac{N}{\text{int}\left(\frac{h}{r}\right)} + 0.99(9) \right] - 1 \right\} \cdot r \cdot \sqrt{3}$ is the thickness of all layers, with the exception of the first one.

With the knowledge of (3.7) it is possible to verify the condition(2.16).

To complete the coil model construction it is necessary to define its resistivity ρ_e [Ω.m] and mass density ρ_m [kg/m^3]. The wire manufacturer usually does not give these values, however it provides the wire length by unit of weight λ_{wl} [m/kg], and the resistance by length of wire ς_{wlr} [Ω/m], which can both be used to calculate the required parameters. Equations (3.8) and (3.9) express that relationship:

$$\rho_e = \varsigma_{wlr} \cdot \pi \cdot r_{cu}^{\ 2} \tag{3.8}$$

$$\rho_m = \frac{1}{\lambda_{wl} \cdot \pi \cdot r^2} \tag{3.9}$$

The values used for the coil construction of the EFD25 VI are presented in **TABLE 2**.

TABLE 2
DIMENSION VALUES FOR THE EFD25 VI COIL CONSTRUCTION

Variable Name	Main winding	DC windings
χ [mm]	0.1	0.1
τ [mm]	0.55	0.578
h [mm]	16.6	16.4
N	27 (31) (35)[6]	71
K_u	0.6055	0.4805
ρ_e [Ω.m]	1.72E^{-8}	1.68E^{-8}
ρ_m [kg/m^3]	7794.55	7748.02
r_{cu} [mm]	0.2553	0.14295

Where χ is the gap between the coil and the ferromagnetic core.

The coil construction parameters for the remaining constructed VIs can be found in Apendix A.

[6] The number of turns calculated by (2.12) is 35. However, in order to maintain the desired maximum inductance value, in his experimental tests Marco Martins reduced this number to 31 and in the FEA software it was needed to reduce it to 27.

3.3. Mesh build

The name "finite element method" is directly connected with the mesh. The meshing process consists of dividing the study domain into mesh elements (*in help by CEDRAT*). The study domain is composed by all 3D constructions except the non-meshed coils which, as the name implies, are not meshed. The mesh elements form small volumes to which the FEM applies Maxwell's and Biot-Savart's equations to calculate the magnetic interaction between them. In Fig. 3.5 (a) it is possible to observe the mesh used in the EFD25 VI.

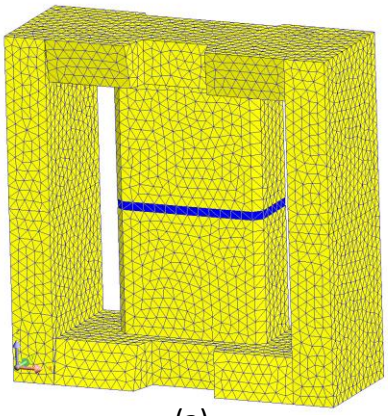

(a)

```
Volume elements :
   Number of elements not evaluated     : 0  %
   Number of excellent quality elements : 57.23  %
   Number of good quality elements      : 32.36  %
   Number of average quality elements   : 9.27  %
   Number of poor quality elements      : 1.15  %
```

(b)

Fig. 3.5 – Mesh information; (a) 3D core model with visible mesh distribution; (b) Global mesh quality evaluation, provided by the FEA software.

The number of volumes is directly connected with the quality of the mesh. The more volume elements used, the more accurate the results are, although the simulation is slower. The absolute value of volume elements used in this simulation is 2036934, and 338364 is the number of nodes. The relative meaning of these values is shown in Fig. 3.5 (b) which shows the global mesh quality calculated by the software. As it is possible to observe, about 99% of the mesh has an average or high quality and 90% is considered good or high quality. It is also important to consider that some of these not "excellent" are related to the low mesh quality used to simulate the non-relevant magnetic effect in the further air zones from the core, which are not shown in the figure. Those zones are delimited by an "infinity box".

3.4. Infinity box

Usually, in magnetic applications, there are magnetic fields and fluxes surrounding the main magnetic structure. Any magnetic field decreases with the increase of the distance from the dipole that is creating it. Therefore, the further the distance from the dipole, the lower the magnetic field effect. Mathematically that effect can be considered zero at the infinite however,

practically, after some distance, the magnetic effect is so low that it can be considered negligible.

The infinity box is a geometric structure that limits the range of the FEM calculus. It is composed by two boxes, an inner box and an outer box as shown in Fig. 3.6.

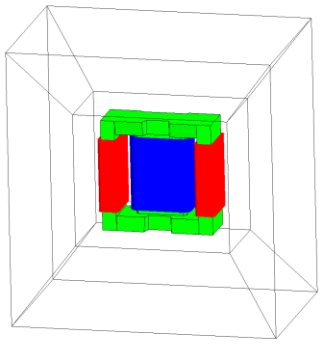

Fig. 3.6 – Infinity box demonstration around the VI model

TABLE 3
INFINITY BOX DIMENSION VALUES

Axis	Inner Box	Outer Box
X	$0.7 \cdot comp1$	$1.4 \cdot comp1$
Y	$1.05 \cdot espess1$	$2.1 \cdot espess1$
Z	$1.2 \cdot alt1$	$2.5 \cdot alt1$

The inner box is used to wrap a smaller volume where the magnetic field is considered relevant. The outer box limits a wider volume where the magnetic field effect is not as relevant but cannot be ignored. These two box systems allow the user to improve their air/vacuum mesh by selecting a tinier mesh in the inner box and a wider one in the outer box. The calculation of the magnetic flux in the air/vacuum region is one of the most time consuming processes in the Flux simulation. The set of a proper infinity box and air/vacuum mesh is fundamental in order to have an accurate and time-efficient model. TABLE 3 contains the dimensions of each half side of the box.

3.5. Magnetic material specification

Each piece of material has its own properties that determine its behaviour under different conditions. CEDRAT allows the user to specify some of the properties associated to each material part which are the following: magnetic, electrical and dielectric property, thermal conductivity, volumetric heat capacity and mass density. For magnetic studies, it is only necessary to define the magnetic property of each used material. In the present study four different types of materials were used: the N87 ferrite metal used in the core structure, the copper metal used in the coil windings, the plastic used in the coil supports and electric wire insulation, and the air that surrounds the VI. The air, plastic, and copper have a linear and similar magnetic behaviour, since their permeability is approximately equal to the vacuum μ_0. Therefore, in order to simplify the construction and reduce the simulation time, the plastic

supports were not considered in the VI building and were replaced by air. In addiction, the copper is internally defined in the non-meshed coil section. The ferrite metal presents a nonlinear magnetic behaviour, and must therefore be defined. Fig. 3.7 (a) contains the N87 B(H) curve which defines the behaviour of the material used in the core construction.

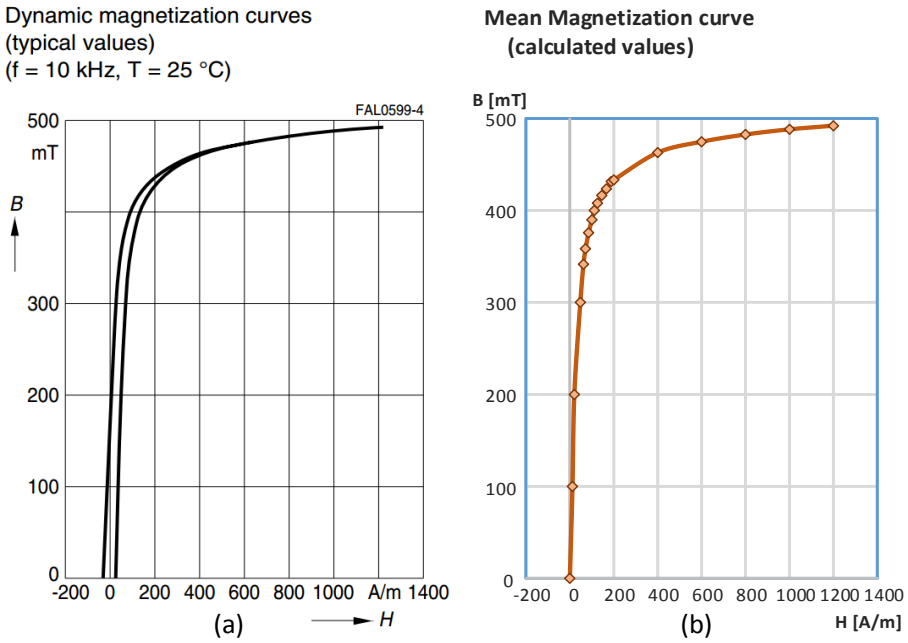

Fig. 3.7 Dynamic magnetization curves for N87 ferrite metal; (a) Hysteresis curve provided in the manufacturer datasheet [35]; (b) mean B(H) spline curve used in FEA Software;

As explained previously, the Flux software does not support hysteresis. The solution presented by CEDRAT for soft magnetic materials is to use the mean curve (presented in Fig. 3.7 (b)). The software allows the B(H) curve to be modelled with a method called "analytic saturation curve + knee adjustment". It is defined according to the following equation:

$$B(H) = \mu_0 + J_s \frac{H_a + 1 - \sqrt{(H_a + 1)^2 - 4H_a(1-a)}}{2(1-a)} \tag{3.10}$$

with:

$$H_a = \mu_0 H \frac{\mu_r - 1}{J_s} \tag{3.11}$$

where μ_0 is the permeability of the vacuum; μ_r is the initial relative permeability of the material (at the origin); J_s is the magnetic polarization at saturation $[T]$; and a is the adjustment coefficient of the B(H) curve knee $(0 < a \leq 0.5)$. This is an accurate method for modelling many materials, including the 3C85. However it does not replicate the behaviour of N87 material in the saturated region correctly. Due to the VI operation, it is particularly important in this study to have an accurate model that correctly follows the material operation in the

saturated region. Therefore, the most accurate solution is to introduce the points of the spline curve showed in Fig. 3.7 (b).
The modulation data of both N87 and 3C85 materials can be found in Appendix B.

3.6. Simulation types

The processing of all electromagnetic phenomenon described by Maxwell's equations is too complex even for modern technology. To simplify the FEM process and make it viable in terms of simulation time, CEDRAT divided the analysis into four categories: Electric, Magnetic, Thermal, and Thermal Coupling. For the VI study the Magnetic application was used. The FEM used in this category does not use the first of Maxwell's equation since it is a strictly electric one. In addiction the FEM used in Electric applications does not use the second of Maxwell's equation. The thermal applications use another type of differential equations that do not relate to this work. Within the magnetic applications, it is possible to select one of three following simulation types: Magneto Static, Steady State AC, and Transient Magnetic. The Steady State AC package allows the study of devices in the harmonic state (sinusoidal steady state) for a given frequency. The Magneto Static package also enables the user to study the phenomena created by a magnetostatic field. The magnetic field is related to the presence of DC currents (stationary currents) and/or of permanent magnets (*in help file - CEDRAT*). The Transient Magnetic package allows the study of the phenomena created by a time variable magnetic field. The magnetic field is related to the presence of variable currents (and possibly permanent magnets) (*in help file – CEDRAT*). In this work, both Magneto Static and Transient Magnetic simulations were performed to study the electromagnetic effect in the VI. The results are shown in the next chapter.

CHAPTER 4 – Finite Element Analysis of the VI

This chapter performs an electromagnetic analysis using FEA software. The present study is divided into two categories. The first one involves a magnetostatic analysis of different DC and main current values. It is used to demonstrate the general VI operation of E-shaped cores. The obtained results are compared with a real life model and with different E-shaped VIs. The second category consists of the insertion of VI in a high frequency resonant circuit and performing a transient-state simulation. This analysis aims to evaluate the dynamic electromagnetic behaviour of the VI when crossed by an alternating current.

4.1. Magnetostatic analysis

Magnetostatic simulations were run using the EFD25, ETD49 and EF25 VIs 3D models. Initially, the simulation was performed using different main and DC currents in order to analyse the general operating principle of double E-shaped VI topologies. For each magnetic simulation the software traces a map of the H-field and flux density *B* along the 3D model for every combination of variables, in this case i_{main} and i_{DC}. Later, another test was performed for a constant main current ($i_{main} = Cte$) and different DC currents and air-gap lengths. The purpose was to analyse the influence of the air-gap in the inductance variation.

Fig. 4.1 and Fig. 4.2 represent, respectively, the magnetic flux density and the permeability of the EFD25 VI at four different operating points in terms of instantaneous current values (i_{main} and i_{DC}). In Fig. 4.1, each arrow represents the orientation, direction, and value of the magnetic flux density. The size and colour of the arrows are proportional to the amount of magnetic flux density. In Fig. 4.2 each sphere represents the value of the local magnetic permeability. The size and colour of the spheres are proportional to the amount of magnetic permeability in that zone.

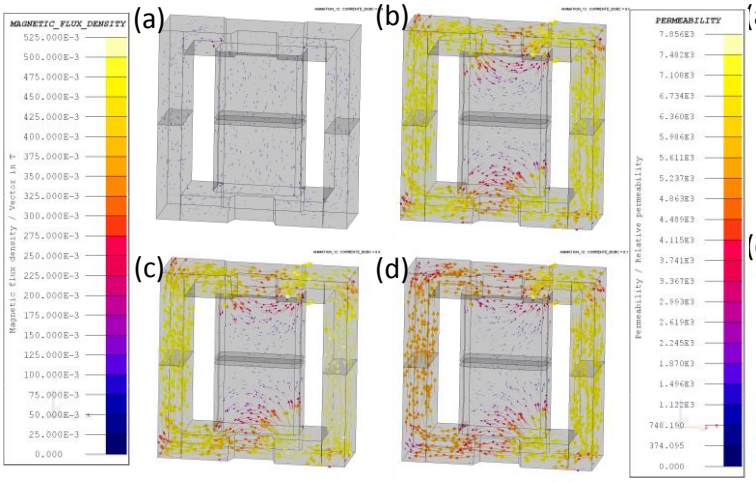

Fig. 4.1 - Magnetic flux density distribution in the VI for different current levels in the main and control windings: (a) $i_{main} = 0.8\text{A}$ and $i_{DC} = 0\text{A}$; (b) $i_{main} = 0\text{A}$ and $i_{DC} = 0.4\text{A}$; (c) $i_{main} = 0.8\text{A}$ and $i_{DC} = 0.4\text{A}$ (d) $i_{main} = 0.8\text{A}$ and $i_{DC} = 0.1\text{A}$.

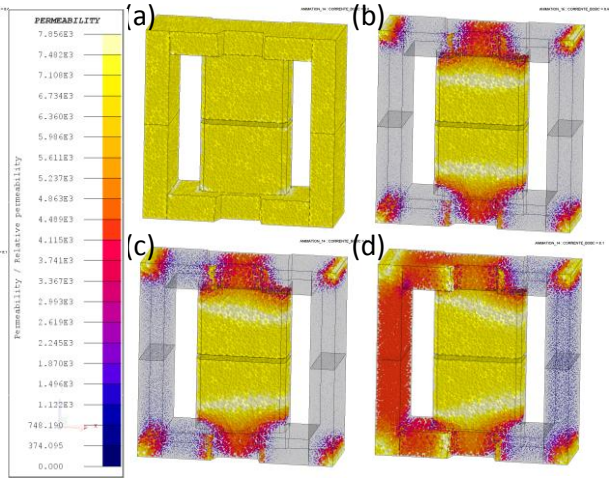

Fig. 4.2 - Permeability in the VI for different current levels in the main and control windings: (a) $i_{main} = 0.8\text{A}$ and $i_{DC} = 0\text{A}$; (b) $i_{main} = 0\text{A}$ and $i_{DC} = 0.4\text{A}$; (c) $i_{main} = 0.8\text{A}$ and $i_{DC} = 0.4\text{A}$ (d) $i_{main} = 0.8\text{A}$ and $i_{DC} = 0.1\text{A}$.

Fig. 4.1 (a) and Fig. 4.2(a) $i_{main} = 0.8A$ and $i_{DC} = 0A$. Fig. 4.1 (a) shows that the magnetic flux density is relatively uniform and exhibits a fairly low value. The gapped core helps maintain a low effective permeability in the centre arm, thereby avoiding quick saturation of the core. However, since the flux density level is low and the core is not saturated, the permeability is high which is clearly seen in Fig. 4.2 (a). As the left and right arms of the core are symmetrical in shape, the permeability is uniform. The permeability in the air-gap is therefore much smaller than in the rest of the core.

In Fig. 4.1 (b) and Fig. 4.2 (b), $i_{main} = 0A$ and $i_{DC} = 0.4A$. In comparison with Fig. 4.1 (a), the flux density is now higher and distributed along the outer arms. It is possible to see from Fig. 4.2 (b) that compared to the centre arm, where there is a gap, the side arms of the core are saturated. This is the reason there is a lower value of magnetic permeability in these zones. The higher level of permeability in the centre arm is due to the fact that there is no current in the main winding and, since the control windings are placed in opposite polarity the generated flux tends to form a loop in the external path.

In Fig. 4.1 (c) and Fig. 4.2 (c), $i_{main} = 0.8A$ and $i_{DC} = 0.4A$. In this case, all windings are responsible for flux generation. The magnetic flux created by the main winding is smaller than the one produced by the control windings due to the number of turns and the existence of the air-gap in the centre arm. However, the magnetic flux density in the core is not uniform. The flux produced by the main winding creates disparities in the value of the magnetic flux density in both side arms due to the positioning of the control windings. On the left arm, the magnetic

flux created by the main winding has an opposite direction compared to the one produced by the left control winding. The situation is reversed in the right arm where both fluxes have the same direction. This is why the magnetic flux density in the left arm is slightly lower when compared to the right arm. Because of the non-linear response of the ferromagnetic material in saturated conditions, different levels of magnetic flux density imply different levels of magnetic permeability as shown in Fig. 4.2 (c).

In Fig. 4.1 (d) and Fig. 4.2 (d), $i_{main} = 0.8A$ and $i_{DC} = 0.1A$. This operating condition maintains i_{main}, but decreases the DC current value. This results in an overall reduction of the magnetic flux density in the side arms of the VI. However, the previous observations are still valid. Since the DC current is lower, the magnetic unbalance between both left and right arm fluxes is higher. If the global saturation level of the side arms is smaller, the unbalance is more noticeable. In addition, the magnetic flux density imposed by i_{main} is less responsible for saturating the core when compared to the one imposed by i_{DC}.

The observations made in Fig. 4.1 and Fig. 4.2 are consistent with the analysis done for the reluctance model of the core. It is now clear that the permeability of the core changes according to the level of the DC control current and the current in the main winding. The air-gap in the centre arm has an impact on the behaviour of the circuit, increasing the reluctance of the centre arm and preventing quick saturation of the core. The superimposition of different flux directions in the outer arms creates a flux value disparity between both of them. To analyse this effect, an additional test was performed where the modulus of magnetic flux density (Fig. 4.3) was measured along a traced path crossing the three arms (Fig. 4.4).

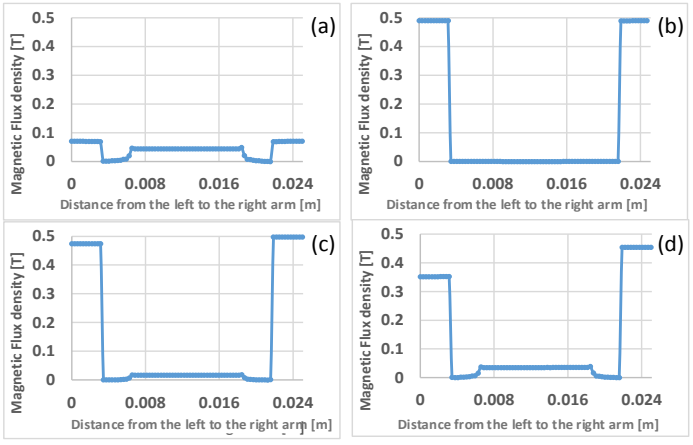

Fig. 4.3 – Module of the magnetic flux density distribution along the red path showed in Fig. 4.4: (a) $i_{main} = 0.8A$ and $i_{DC} = 0A$; (b) $i_{main} = 0A$ and $i_{DC} = 0.4A$; (c) $i_{main} = 0.8A$ and $i_{DC} = 0.4A$ (d) $i_{main} = 0.8A$ and $i_{DC} = 0.1A$.

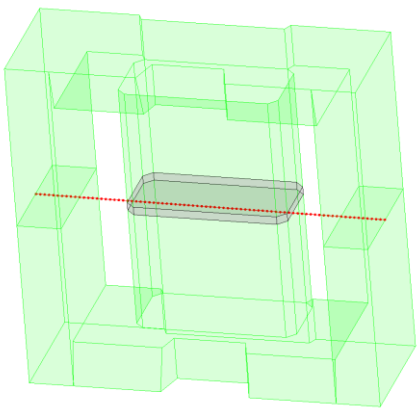

Fig. 4.4 – Location of the compound path marked with a red line used in FEA software in order to obtain Fig. 4.3 results.

Fig. 4.3 (a-d) corresponds to the same operating conditions as in Fig. 4.1 (a-d) and Fig. 4.2 (a-d). The direction of the flux density along the traced path in the material and air-gap areas is parallel to the z-axis (it has a "vertical" looking from a front or side view). Therefore, the modulus returns a value nearly equal to the absolute value of the z-component of the flux density vector.

In Fig. 4.3 (a) $i_{main} = 0.8A$ and $i_{DC} = 0A$. As observed in Fig. 4.1 (a) the magnetic flux density has a low value in all arms of the core. In this curve it is possible to observe that the amount of flux density in the centre arm is slightly lower than in the side arms. This happens due to the fact that the cross sectional area of the centre arm is slightly higher than the sum of the cross sectional areas of the outer arms.

In Fig. 4.3 (b) $i_{main} = 0A$ and $i_{DC} = 0.4A$. This figure confirms the analysis of the previous Fig. 4.1(b), since it shows clearly that there is no flux density crossing the centre arm of the core and the side arms are saturated.

In Fig. 4.3 (c) $i_{main} = 0.8A$ and $i_{DC} = 0.4A$. In this situation, the current in the main winding creates a magnetic flux that superposes the DC flux generated in the side arms. This interaction creates the unbalance in magnetic flux seen in the figure. The decrease in the value of the left arm flux density is due to the sum of two magnetic fields with opposite polarity, and the increase in the right arm flux density is due to the sum of two magnetic fields with the same polarity. In addition, it is possible to observe a slight decrease in the magnetic flux density in the centre arm when compared with Fig. 4.3 (a). This reduction is explained by the increase of saturation in the outer arms, which in turn decreases the material permeability and restricts the flux.

In Fig. 4.3 (d), $i_{main} = 0.8A$ and $i_{DC} = 0.1A$. Comparing this mode of operation with the previous Fig. 4.3 (c), it is clear that the decrease of the DC current increased the flux unbalance between outer arms. This occurs due to the non-linearity of the material. In this case, the left arm is operating in the transition region and the right arm is operating in the saturated region. The decrease of the DC current also increased the centre flux density, as expected.

L_{main} curves from Fig. 4.5 were obtained by the ratio between the total magnetic flux flowing through the main winding and the corresponding instantaneous current value given by FEA software, which conforms to the previous presented equation (2.6). The figure shows the evolution of the instantaneous inductance L_{main} as a function of the DC current for different levels of the instantaneous main current. For higher values of the DC current, the value of L_{main} is lower. For DC current values above $0.7\,\mathrm{A}$ the change in L_{main} is negligible.

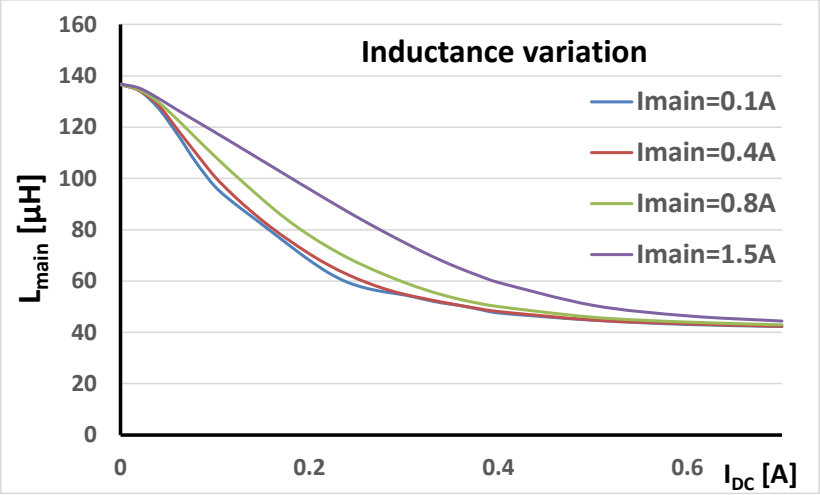

Fig. 4.5 Instantaneous inductance L_{main} as function of the DC control current for different levels of resonant current obtained from FEA model.

The observed evolution is similar for all double E-shaped VI which have the same distribution of control and main windings. In this particular case, it is possible to compare these characteristics with the small-signal characteristic of the VI prototype obtained with an LCR meter, as shown in Fig. 4.6.

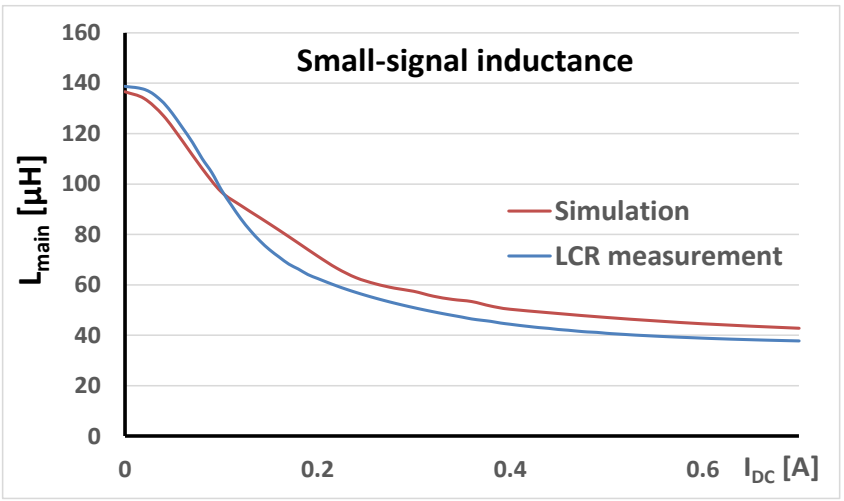

Fig. 4.6 – Small-signal inductance comparison between simulation and LCR measurement. Simulation: $i_{main} = 10mA$

The simulation small-signal curve was obtained with an instantaneous main current of 10 mA. As can be observed, both curves are similar which demonstrates the accuracy of the FEA model.

Another magnetostatic analysis was performed using the ETD49 VI. This VI contains a different core shape and has a higher volume when compared to the EFD25. It was tuned for higher power and higher inductance values. The presented analysis has the objective to compare the similarities and differences between different E-shaped cores.

In Fig. 4.7 and Fig. 4.8 respectively, the magnetic flux density and the permeability of the core is demonstrated at four different operating points in terms of instantaneous current values (i_{main} and i_{DC}).

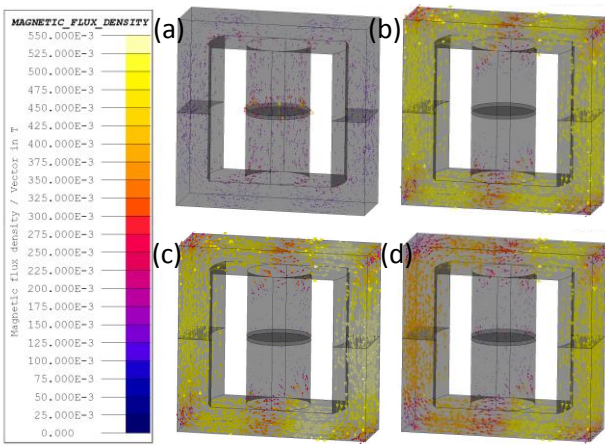

Fig. 4.7 - Magnetic flux density distribution in a ETD49 VI for different current levels in the main and control windings: (a) $i_{main} = 1A$ and $i_{DC} = 0A$; (b) $i_{main} = 0A$ and $i_{DC} = 1.5A$; (c) $i_{main} = 1A$ and $i_{DC} = 1.5A$ (d) $i_{main} = 1A$ and $i_{DC} = 0.5A$.

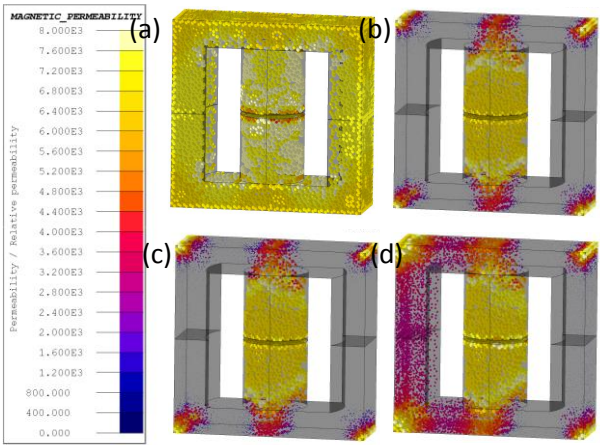

Fig. 4.8 - Permeability in aETD49 VI for different current levels in the main and control windings: (a) $i_{main} = 1A$ and $i_{DC} = 0$; (b) $i_{main} = 0$ and $i_{DC} = 1.5$; (c) $i_{main} = 1A$ and $i_{DC} = 1.5A$ (d) $i_{main} = 1A$ and $i_{DC} = 0.5A$.

In spite of the difference in the current values, the four states of Fig. 4.7 (a-d) and Fig. 4.8 (a-d) correspond to an equivalent operating condition as Fig. 4.1(a-d) and Fig. 4.2(a-d). The winding current difference is due to the higher operating power and the different number of turns associated with this VI.

Fig. 4.7(a) and Fig. 4.8(a), $i_{main} = 1A$ and $i_{DC} = 0A$. Fig. 4.7 (a) shows that the magnetic flux density is relatively uniform and has a low value. This observation is enhanced by Fig. 4.8 (a) which shows that there is no saturation in the core. As observed previously in the EFD25 VI, the air-gap is responsible for maintaining a low flux flow and high permeability

In Fig. 4.7(b) and Fig. 4.8(b), $i_{main} = 0A$ and $i_{DC} = 1.5A$. In this situation, there is no current in the main winding and the DC windings have their maximum current value. Due to the inexistence of an air-gap in the DC flux path, there is a high magnetic flux flow in the outer arms of the core, which is observable in Fig. 4.7(b). Therefore, in Fig. 4.8(b) for the same areas, a low value of magnetic permeability can be observed.

In Fig. 4.7(c) and Fig. 4.8(c), $i_{main} = 1A$ and $i_{DC} = 1.5A$. In this case, all windings are being driven at their maximum nominal current. In Fig. 4.7(c) it can be observed that one of the arms has a higher flux density value than the opposite arm. Compared to Fig. 4.7(b), this arm presents a higher flux density value, despite being driven by the same DC current. This happens because there is a superposition of DC and main flux and both are in the same direction. In the opposite

arm there is also a superposition of magnetic flux but, because they have opposite directions, the resulting flux has a slightly lower value.

In Fig. 4.7 (d) and Fig. 4.8 (d), $i_{main} = 1A$ and $i_{DC} = 0.5A$. This is a similar scenario to the previous one, but with a lower DC current value. The decrease of the DC current increased both the flux and permeability unbalance between both arms of the core.

Despite the fact that the ETD49 VI was modelled for higher power and different inductance values, its behaviour is similar to the EFD25. The study presented in this chapter can be expanded for any other double E-shaped V, as long it respects the methodology presented in Chapter 2.

The following table contains the inductance values resulting from tests performed to three different E-shaped VI cores, each one containing different air-gap values. The presented data was acquired from the FEA simulation software.

TABLE 4

INDUCTANCE VALUES OF DIFFERENT CORE STRUCTURES AND AIR-GAPS, FOR A MAIN CURRENT VALUE OF 0.1A.

All values are in S.I units with the exception of the air-gap length which is in millimetres

		EFD25			EF25			ETD 49				
		Gap=0.1	Gap=0.6	Gap=1	Gap=0.1	Gap=0.6	Gap=1	Gap=0.1	Gap=0.3	Gap=0.6	Gap=1	Gap=1.5
FEA	L_{max}	6.41E-04	1.37E-04	8.89E-05	6.15E-04	1.32E-04	8.66E-05	1.75E-02	6.26E-03	3.98E-03	2.45E-03	1.60E-03
	L_{min}	5.40E-05	4.23E-05	3.64E-05	7.65E-05	5.30E-05	4.26E-05	8.51E-04	7.26E-04	8.45E-04	6.59E-04	5.93E-04
	RT	11.86	3.23	2.44	8.04	2.49	2.03	20.58	8.63	4.72	3.72	2.69
	N	27			27			70				

The table is split into three sections, each one matching a different VI whose core structure name is indicated. The EFD25 and ETD49 correspond to the VIs analysed before. The EF25 has an E-shaped core with dimensions similar to the EFD25, but contains a more uniform shape. All the detailed specifications about this VI can be found in Appendix A.

The inductance analysis was performed for different air-gap lengths whose values are indicated in the second row. The following acronyms for each row apply: $L_{\max}$ is the maximum inductance value when the DC current is zero; $L_{\min}$ is the minimum inductance value when the DC current is maximum ($i_{DC} = 0.7$A for both EFD25 and EF25 VI and $i_{DC} = 1.5$A for the ETD49). RT means ratio and is the quotient between the maximum and minimum inductance values; N is the number of turns completed by the main winding. The main winding has an instantaneous current of 100mA.

In this analysis, it is possible to observe that the smaller the air-gap length, the bigger the obtained ratio. This ratio value is very important since it determines the amount of inductance

variation associated with the VI. In addition, if the air-gap length is shorter, then the maximum current in the main winding must be lower, in order to maintain the condition observed in (2.10) : $B_{max} \approx [0.1B_{sat}; 0.3B_{sat}]$. It was noticed that this condition was not demonstrated in the three VI's when a $0.1mm$ air-gap length was applied. Not applying this condition can decrease the maximum inductance value and increase the minimum one, resulting in a lower ratio value.

4.2. Transient analysis

The transient analysis of the EFD25 based VI is done taking into account that magnetic device is used in a dimmable LED driver based on a RSCC circuit, as presented in Fig. 4.9. The VI allows the rms value of the resonant current, I_{main}, to be controlled between the maximum and minimum values which dictates the value of the output power and the corresponding luminous flux level. In order to perform this transient analysis, the RSCC driver is implemented in the FEA software with the values of TABLE 5 also being considered. The purpose of this is to evaluate the magnetic operating response of the VI under such application. The discretization time used in all transient simulations was $T_s = 1 \times 10^{-6}$s.

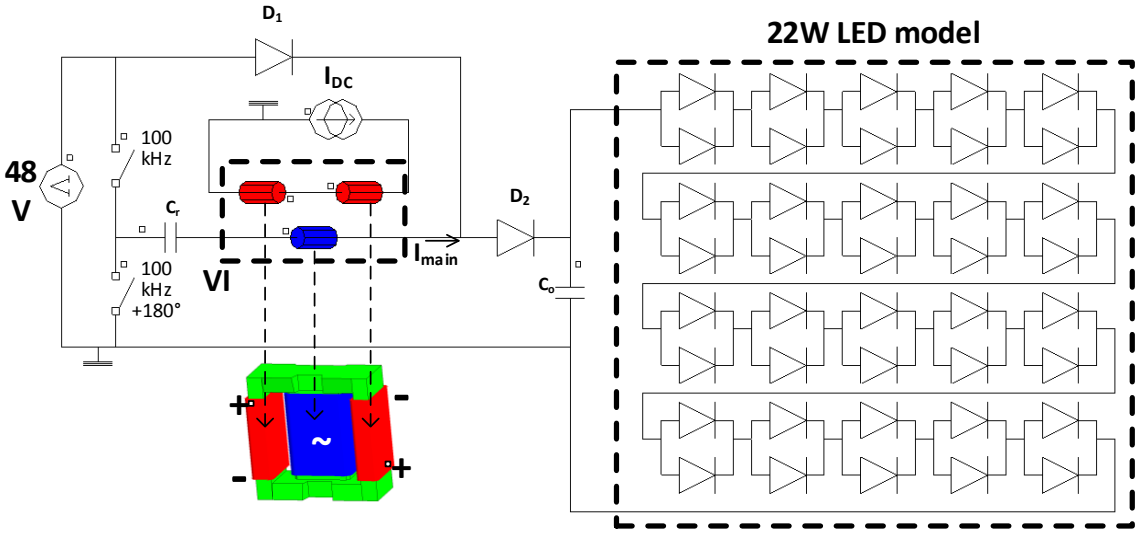

Fig. 4.9 – Step-up of a RSCC circuit implemented in the FEA software

TABLE 5
COMPONENTS OF THE LED DRIVER PROTOTYPE

Description	Specification	Description	Specification
Input voltage	V_{in}=48V	Voltage ratio at resonance	V_{out}=2V_{in}
Switching frequency	f_s=100kHz	Duty cycle	D=0.5
Diodes $D_1; D_2$	BYC5D 500	Switches	MOSFET IRF520
Output Capacitor	$C_0 = 10\mu F / 250V$	Resonant Capacitor	C_r=0.47μF/100V
LED branch	20x Osram Golden Dragon Plus, I_{LEDs} = 0.1A ~ 0.35A	Output Capacitor	C_O=10μF/250V

Fig. 4.10 shows both the resonant current and the corresponding magnetic flux waveforms in different operating conditions, for $i_{DC} = 0A$, $i_{DC} = 0.1A$ and $i_{DC} = 0.4A$.

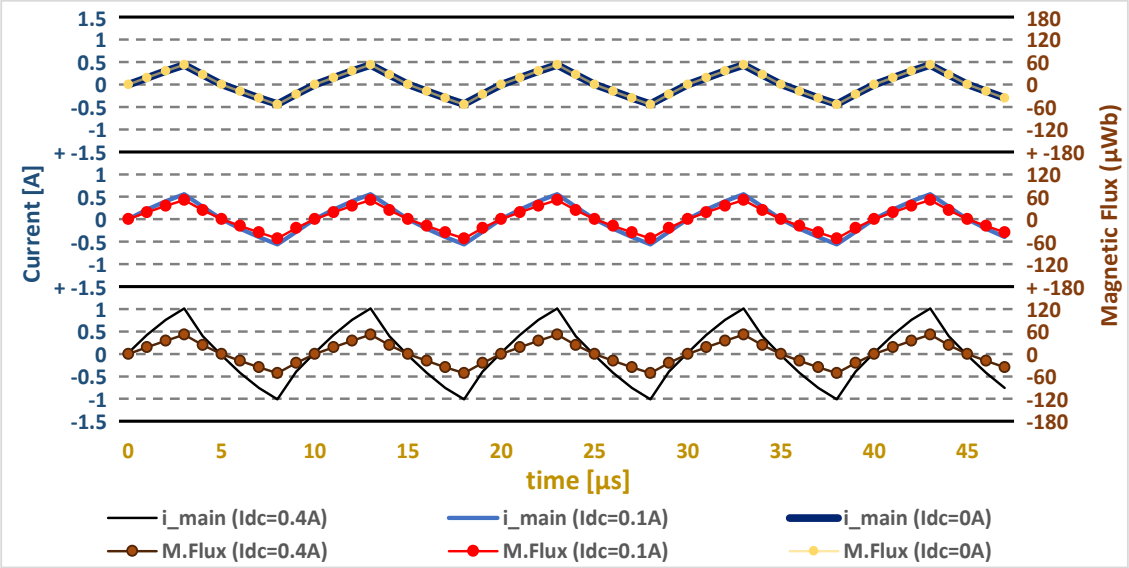

Fig. 4.10 - FEA simulation results: main winding magnetic flux and current waveforms at f_s=100 kHz for: (a) $i_{DC} = 0A$ (minimum power); (b) $i_{DC} = 0.1A$; (c) $i_{DC} = 0.4A$ (maximum power).

These waveforms were acquired under output voltage steady-state conditions for a 100 kHz switching frequency. All three magnetic flux curves show a similar peak value. However, when the DC current increases from 0A to 0.4A, the peak value of the main current increases from 0.5A to 1A. This is linked to the decrease of the permeability (or increase in reluctance) "seen" by the main winding due to the saturation caused by the total flux linkage in the side arms. In addition, it is possible to notice that the increase of the DC current does not significantly affect the magnetic flux established in the centre arm of the core.

Fig. 4.11 (a) and Fig. 4.11 (b) show both the current and voltage waveforms of the main winding of the VI obtained from the experimental LED driver, for maximum and minimum

load (LEDs) power level, respectively. A strong correlation is shown between the simulated current waveforms, shown in Fig. 4.10 (a) and Fig. 4.10 (c) and these experimental results. This validates the proposed FEA simulation model, showing it to be a powerful tool to understand the global behaviour of the VI.

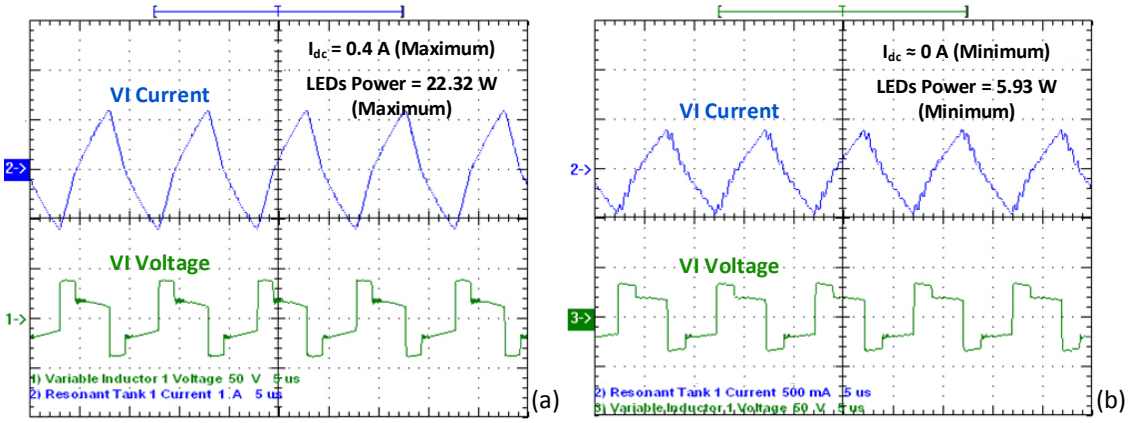

Fig. 4.11 – VI current and voltage: (a) blue and green curves, respectively (1 A/div and 50 V/div, respectively, 5 µs/div), at maximum power level conditions ($i_{DC} = 0.4A$); (b) blue and green curves, respectively (0.5 A/div and 50 V/div, respectively, 5 µs/div), at minimum power level conditions ($i_{DC} = 0A$).

Fig. 4.12 shows the L_{main} instantaneous variation for three different i_{DC} values (those from Fig. 4.10). It also indicates the corresponding average value of L_{main}. Clearly there is no oscillation in the value of L_{main} for $i_{DC} = 0$. The VI is operated in the linear region of the B(H) curve. As discussed in the previous analysis of the results presented in Fig. 4.1(a) and Fig. 4.2 (a), there is no saturation in the core at any instant, as the peak value of the main current is relatively low and there is no DC current flowing through the control windings. Therefore, L_{main} is expected to be constant.

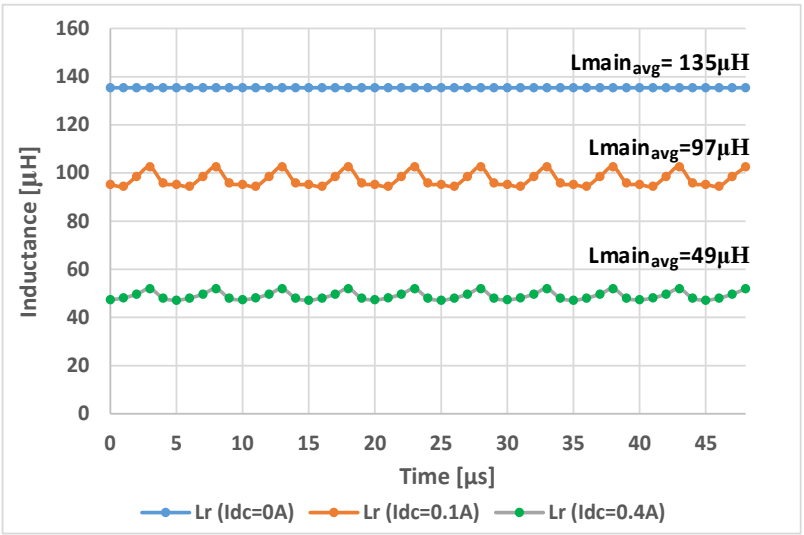

Fig. 4.12 - L_{main} for different levels of DC current at f_s=100kHz, obtained from the FEA model. $Lmain_{avg}$ is the arithmetic average value of L_{main}

It is also possible to observe that the increase of i_{DC} leads to a smaller average value of L_{main}. However, in these cases, L_{main} does not remain constant and in fact, oscillates at twice the operating frequency. This is due to two reasons: the fact that $i_{DC} \neq 0$ which has an impact on the magnetic flux density (the core is forced to operate in the knee of the magnetization curve), and the fact that the current in the main winding is AC. The alternate behaviour of i_{main} has a direct impact on the permeability unbalance identified in Fig. 4.3 and Fig. 4.4, as well as in the saturation level of the core. The permeability increase in one side of the arm is not proportional to the decrease in the opposite side, because the magnetic response of the ferromagnetic material is not linear in the transition and saturated regions. Therefore the reluctance seen by the main winding varies through time, creating a pulsating inductance value described as $L_{main}(t)$. It is also clear that this oscillation is smaller for $i_{DC} = 0.4A$ than for $i_{DC} = 0.1A$. Under the previous conditions, if the saturation level of the core is higher then the peak value of L_{main} tends to be lower. The oscillation in L_{main} tends to decrease as a result. There will be a maximum value of i_{DC} for which the variation in L_{main} is negligible. At this operating point, the core is fully saturated and L_{main} tends to be constant again.

In the transient simulation, it was also obtained the VI large-signal inductance curve. This curve differs from the small-signal one showed in Fig. 4.6 since the current flowing through the main winding does not have a small value of 10mA but the dynamic value of the resonant circuit of Fig. 4.9. As it was observed in Fig. 4.10 and Fig. 4.11 the amplitude of i_{main} depends on the DC current value. Therefore, to obtain the large signal-inductance curve, a test was performed where the DC current would change through five fixed steps as shown in Fig. 4.13(a).

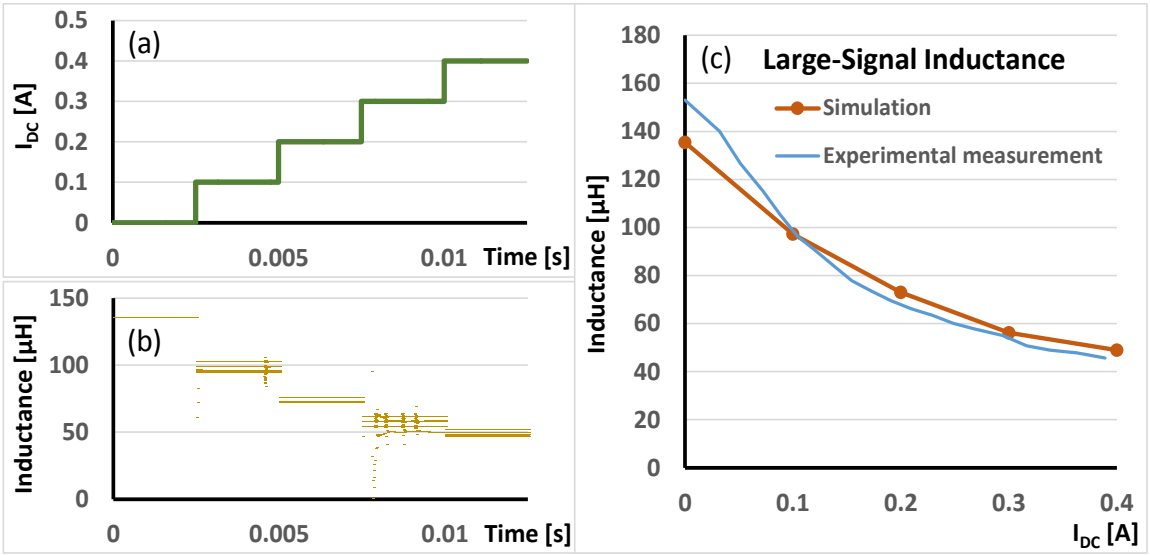

Fig. 4.13 - Large-Signal inductance characterization. (a) DC current variation through time; (b) Inductance variation through time; (c) Large-signal inductance curve comparing the simulation and experimental measurement.

It was verified that the resonant circuit needed about $1ms$ to reach its steady state value. Therefore each step was simulated during$1.25ms$. The filtered dynamic inductance value is shown in Fig. 4.13 (b). The inductance represented here was obtained through the quotient between the magnetic flux and current of the main winding. Fig. 4.13(c) shows the large-signal inductance variation obtained using the FEA software and a comparison to the experimental measurement [22]. The five orange points represented here are the arithmetic average values of the inductance of Fig. 4.13 (b) for each value of the DC current of Fig. 4.13 (a).

As it is possible to observe in Fig. 4.13 (c), the large signal inductance curve obtained with the FEA software is similar to the inductance value obtained by measurement. This reinforces the model's reliability. The small differences observed between simulation and experimental results might have many sources, which are explained below. The figure also demonstrates that the inductance variation practically does not depend on the operation state of the RSCC circuit. Therefore, as soon as a DC step is applied, the change on the inductance value is immediate and remains the same during the time the circuit needs to reach its steady state.

4.3. FEA 3D model adjustments

The studied EFD25 VI was designed using the methodology presented in Chapter 2. However, in order to exhibit a good agreement with the experimental results, some adjustments were made. After the VI assembly, M. Martins noticed he needed to reduce the number of turns of the main winding in order to have a functional VI with the desired maximum inductance [22]. The initial projected number of turns 35 were reduced to approximately 31. Therefore, all the experimental results presented in his work and in this thesis were obtained under that condition. The constructed FEA model also had to be adjusted in order to match the experimental results. In this case, it was confirmed that the most accurate number of main winding turns would be 27.

The experience acquired with the finite element software allows some of the factors that contributed for the necessity of the FEA model adjustments to be identified. They are described as follows:

- Mesh quality – There was an attempt to set the best quality/time performance mesh. With the presented mesh, general magnetostatic tests take approximately 1~2 days[7] to

[7] Simulations performed in Flux 10.4 running on a Windows 7 64bit computer with an Intel® Core™ i7-2600k CPU@ 3.4Ghz processor and 16GB RAM.

simulate while transient tests take 2~8 days (depending on the amount of cycles to simulate). Further tests showed that a tinier mesh would result in a smaller adjustment to 29 turns instead of 27. However, a model with this mesh would not be a time efficient one, and instead of days, the timeframe would be weeks.

- Material Modulation – The N87 material was modelled using a spline curve as mentioned in Chapter3. The data was acquired using the B(H) curve image presented in the material datasheet. A great effort was made to have the most accurate possible curve in Fig. 3.7 (b). Initially, it appears to be an accurate curve. However it contains small errors not shown by sight but that can be highlighted when a differential is applied. Chapter 5 will reveal that this differential is essential to correctly understand the behaviour of the VI. In addition, FEA software applies an interpolation function to calculate the mean points of the B(H) curve which boosts those small errors. Furthermore the B(H) curve presented in the material datasheet is limited. For the N87 material the datasheet presents results for an H-field up to $1200 A.m^{-1}$, while saturated areas in the core contain H-field up to 2400 $A.m^{-1}$ (discussed further in Chapter 5). Therefore there is a considerable part of the B(H) curve that is simply estimated by the software and might not be accurate. This lack of accuracy for saturated regions does not affect the number of turns but may slightly affect the obtained minimum inductance value.
- Experimental results – The experimental results itself may contain errors. There are several factors that influence the obtained results such as the small irregularities in the VI construction or in the instrumentation used to acquire data. For example, in Fig. 4.13 (c) the large-signal inductance associated with a null DC current value is higher than expected. According to the operating principle of the VI, it should be equal or at least slightly lower than the equivalent small-signal value showed in Fig. 4.6.
- FEA software error – The software itself contains some internal errors. The majority of the observed ones did not seem to affect the results, only the capability of obtaining them. However, it was observed that the electrical simulation is not very accurate in resonant circuits, and in some situations it presented serious flaws when compared to other strictly electrical simulators like Simulink or Multisim. In magnetic simulations, it is hard to detect flaws, since there are is no easy alternative to compare the acquired results. However, one cannot rule out this hypothesis.

CHAPTER 5 – Proposal of a new VI reluctance model and design algorithm

One of the classic problems associated with VI modelling is the lack of knowledge with regards to the magnitude of the inductance variation. This chapter begins by proposing a new VI reluctance model that is able to calculate both the maximum and the minimum VI inductance. However, it is highlighted that the implementation of the new model requires the calculation of the magnetic permeability in non-linear and multi-winding systems. The classic concept of magnetic permeability is analysed, as a result, and reformulated in order to be applied to any magnetic system. The differential permeability concept will be used to realize a thorough analysis of the VI operation and correctly describe the permeability distribution along the core under saturation conditions. The new reluctance model is then tested with several VIs. Finally, a new design methodology is proposed and implemented in a Labview program to be easily used by any power electronics engineer.

5.1. VI reluctance model behaviour under saturation

As the name implies, the Variable Inductor is a device which is distinguished from other inductors by its capability of varying the inductance. In Chapter 2, a simplified design methodology that tuned any VI according to the desired maximum inductance value was introduced. However, this procedure did not guarantee that the VI would have the desired inductance variation, a characteristic only discovered with tests performed after the VI assembly. This could represent a major problem to the designer, as they may need to conduct several building attempts and try different combinations of core sizes, winding turns, maximum DC current values, and wire thicknesses, in order to obtain the desired inductance variation. An alternative to that methodology could be the use of an FEA software which allows them to study the VI behaviour in-depth and analyse its inductance variation. However, this requires access to expensive software and many hours to learn how to operate it, construct the model, and simulate it. Even with a pre-constructed FEA model, the simulation process could take between several hours to days. Moreover, the FEA software is able to predict with some accuracy the resulting inductance variation, although it cannot provide the user with the correct combination

of parameters to build the desired VI. This chapter, therefore, aims to present a new modelling technique, based on the reluctance model.

By now it is known that the maximum inductance L_{max} occurs in conditions of null DC current $i_{DC} = 0$, and the minimum inductance L_{min} is obtained in conditions of maximum DC current $i_{DC} \rightarrow$ max. A reluctance model able to emulate the magnetic behaviour of the VI for non-saturated conditions was also presented. This model is based on the assumption that it is possible to understand magnetic behaviour through the analysis of an equivalent electric circuit. This methodology has been used in several applications along the years, and is part of the curriculum taught at many Universities around the world. Fig. 5.1 (a) contains the equivalent reluctance model for an E-shaped VI. This model allows the inductance seen by the main winding for non-saturated conditions (shown in equation (2.21)) to be calculated. In Fig. 5.1 (b), a proposal to use the same reluctance model to calculate the inductance of the main winding for conditions of magnetic saturation is presented.

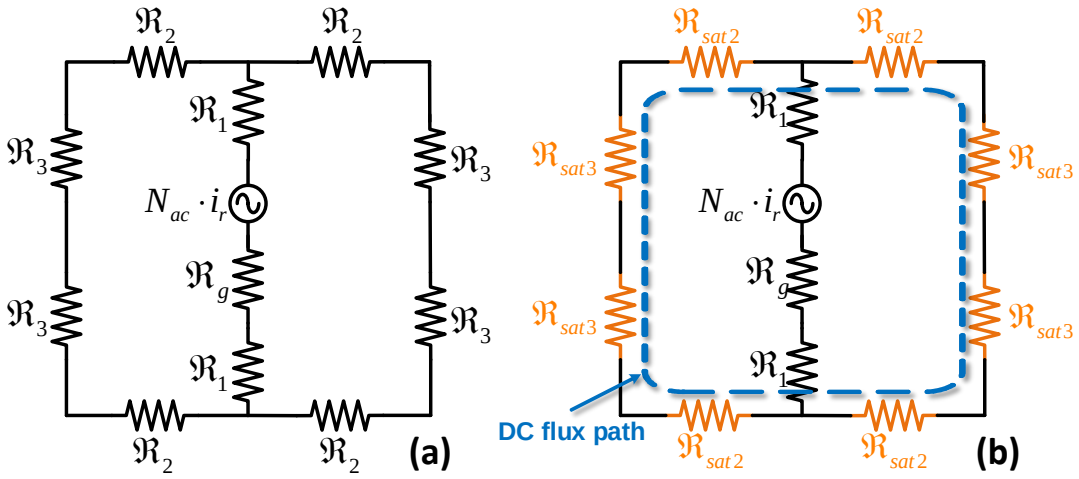

Fig. 5.1 Reluctance model; (a) classic model to obtain the maximum inductance value; (b) proposed model to obtain the minimum inductance value.

It was observed that the DC windings create magnetic saturation along the DC flux path. Therefore, the idea behind Fig. 5.1 (b) is to replace $\Re_2$ and $\Re_3$, with $\Re_{sat2}$ and $\Re_{sat3}$, which are the equivalent reluctance values for saturated conditions. By solving the circuit of Fig. 5.1 (b) the minimum inductance L_{min} can be calculated according to (5.1):

$$L_{min} = \frac{N_{main}^2}{\Re_g + \Re_1 \times 2 + \Re_{sat2} + \Re_{sat3}} \tag{5.1}$$

where the equivalent reluctance for saturated conditions $\Re_{sat2}$ and $\Re_{sat3}$ can be calculated with equation(5.2):

$$\Re_{sat\_i} = \frac{l_i}{\mu_{sat} \times A_i}, \; i = 2,3 \tag{5.2}$$

Where l_i is the length of the magnetic path i [m], μ_{sat} is the value of the permeability for saturated conditions [H.m^{-1}] and A_i is the cross section of the area of the path i [m^2].

The problem issue with this model is the calculation of the permeability value for saturated conditions. The classic equation presented in (2.2), $\mu = B/H$, cannot be used here. The reason is explained below.

5.1.1. Critical analysis of the magnetic permeability definition and impact on the VI model

In Chapter 2, the magnetic permeability was defined as "a property that describes **the ease** with which the magnetic flux flows through a material". In non-linear systems that "ease" varies according to the magnetization state of the material. To demonstrate the limitations of the classic permeability equation in describing, mathematically, its own definition, a theoretical magnetic material is selected for reference. This material's B(H) curve is shown below:

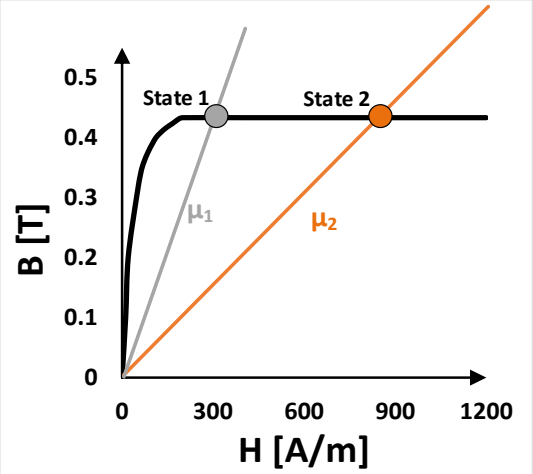

Fig. 5.2 – Initial B(H) curve of a theoretical material that can be completely saturated for H-fields higher than $200 A.m^{-1}$

Fig. 5.2 represents the B(H) curve of the theoretical material that can be completely saturated for H-fields higher than $200 A.m^{-1}$. By "complete saturation" it is meant that the material no longer supports any more passage of magnetic flux. Two different magnetized states are highlighted in the graph using grey and orange dots. The slope of grey and orange lines represent the magnetic permeability associated with each dot. These lines were obtained through the graphic implementation of the classic permeability equation presented in (2.2), where $\mu_1 = B_1/H_1$ and $\mu_2 = B_2/H_2$. As it is possible to see, $\mu_1 > \mu_2$ and $\{\mu_1, \mu_2\} \neq 0$.

However both μ_1 and μ_2 are intended to represent the permeability of a material in a "completely saturated" operating state. In other words, if a second winding tries to increase the flux density for a material operating in *State*1 or *State*2, the permeability perceived by it is zero, since there is no "(…) ease with which the magnetic flux flows through a material". This might present a problem when handling non-linear and multi-winding devices. Although the classic equation is not wrong, it does not return the expected value. The equation $\mu = B/H$ returns a "mean permeability value", which is perceived by the winding that creates the magnetized state. μ_1 is the "mean permeability value" perceived by the winding that creates the magnetic field associated to *State*1 and μ_2 is the "mean permeability value" seen by the winding that creates the magnetic field associated to *State*2. In the majority of non-linear applications this equation is valid, as there is only one magnetic source contributing to the magnetization of the material. However, in the studied type of variable inductors there is more than one winding contributing to the total magnetic flux flowing in the core. For this reason the classic equation is not valid. It is not hard to conclude that the true value of the "property that describes **the ease** with which the magnetic flux flows through a material" is the slope of the B(H) curve. This slope is defined by the differential value of the permeability.

Author note: *No material is known to have the behaviour represented by the B(H) curve of Fig. 5.2. The known most extreme possible case of saturation is when the slope of the B(H) curve is equal to the magnetic permeability in vacuum. The purpose of the used example is to easily explain the limitations of the concept of magnetic permeability. It would be harder to explain the same behaviour with a real case scenario.*

5.2. Differential permeability

The permeability problem associated to non-linear and multi-winding systems can be solved by replacing the permeability value by the differential magnetic permeability, given by the following equation:

$$\mu_d(H) = \frac{dB(H)}{dH} \tag{5.3}$$

where $\mu_d(H)$ is the differential permeability in function of the H-field, and dB/dH is the slope of the B(H) curve.

In linear systems the differential permeability assumes the same value as the permeability. In non-linear systems the value is also the same if the operating point is situated in the

unsaturated region. In the transition and saturated regions the differential permeability returns the useful permeability value associated to the magnetized state. Analysing Fig. 5.2, the differential permeability of both $State1$ and $State2$ is zero which corresponds to the expected value for that material.

Differential permeability has not been widely used to study the behaviour of ferromagnetic materials. There is some published work about differential permeability related to magnetic materials [36]–[39], however none was found using this concept to analyse the behaviour of ferromagnetic materials. The potential of the differential permeability is so unknown that a book published in 2005 [27] defines the concept of differential inductance but does not explain its source – the differential permeability. It also overlaps the concept of differential permeability with incremental permeability. A more recent book [40] has a chapter dedicated to variable inductors. The author presents a thorough study of what he defines as effective inductance. This type of inductance depends on the differential inductance which in turn depends on the differential permeability. However, similarly to [27] no reference is made where differential permeability is used to explain the magnetic behaviour of the non-linear materials.

The FEA software used, adapted to conduct electromagnetic studies, also overlaps differential with incremental permeability. There is one article [7] that briefly interprets the permeability concept as being the slope of the B(H) curve obtained with the following expression: "$(\lim_{\Delta H \to 0} \Delta B/\Delta H)$". The meaning behind the expression that the author intends to define is equivalent to differential permeability, but is not correctly defined due to the following reasons: it affirms that this is the expression of permeability - which it is not - and does not point to any references; it does not make any mention of the concept of "differential permeability"; and the expression itself can be confused with the incremental permeability definition, since $\mu_\Delta = \Delta B/\Delta H$. In addition, $\lim_{\Delta H \to 0}(\mu_\Delta) \neq \mu_d$ especially in the unsaturated zone of a ferromagnetic material. This subject was previously approached by S. H. Minnich in a review of [41] where he emphasised the need for caution in distinguishing between differential and incremental permeability since they are two distinct and widely recognized terms. In conclusion, the differential permeability equation is the equation that correctly interprets the definition of permeability and should be broadly considered in future magnetic-related engineering and physics studies. University engineering programs where magnetism and magnetic materials properties are taught might consider these definitions in order to correctly guide the future electrical engineer into this field of application.

In Fig. 5.3 a comparison between the evolution of the permeability and the differential permeability for the N87 ferrite material is shown. Both curves were obtained through the application of the equations (5.4) and (5.5) to the spline B(H) curve previously showed in Fig. 3.7(b). Equation (5.5) is a numerical approximation to the differential permeability.

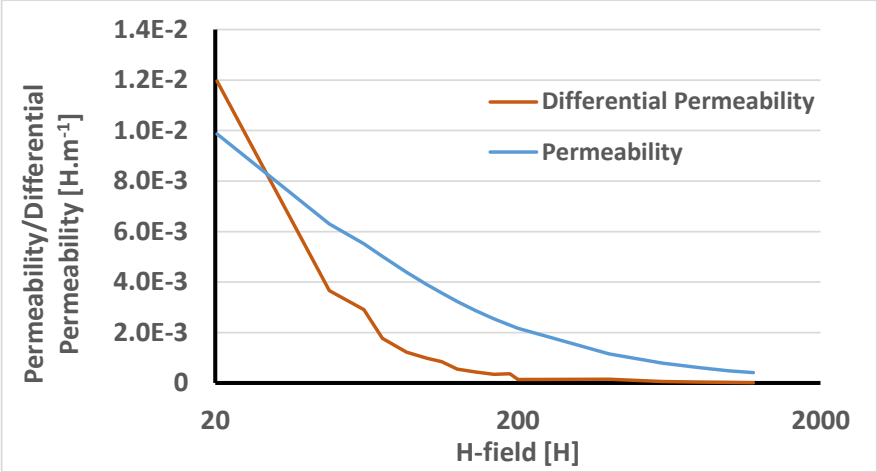

Fig. 5.3 – Evolution of permeability and differential permeability for the N87 ferromagnetic material. The H-field axis is presented in a logarithmic scale

$$\mu[\mathrm{k}] = B[\mathrm{k}] / \mathrm{H}[\mathrm{k}], k \in \mathbb{N} \tag{5.4}$$

$$\mu_{ds}[k+1] = \frac{B[\mathrm{k}+1] - B[k]}{H[k+1] - H[k]}, k \in \mathbb{N} \tag{5.5}$$

In Fig. 5.3 the H-field axis is presented in a logarithmic scale. The irregularities observed in the differential permeability curve are the result of small errors committed in the extraction of the B(H) curve which are highlighted with a derivative function. In the figure it can be observed that the decrease in differential permeability is much higher than the permeability. Furthermore, the differential permeability assumes low values in the saturated region. In fact, for H-fields higher than $300 A.m^{-1}$ the differential permeability value is from several dozens to a few hundred times lower than the correspondent value of a non-saturated region. In addition, the more saturated the material is, the lower the differential permeability variation. Between $400 A.m^{-1}$ and $1200 A.m^{-1}$ the differential permeability only decreases from $6E{-}5H.\mathrm{m}^{-1}$ to $2E{-}5H.\mathrm{m}^{-1}$ for the N87 ferrite material.

5.2.1. Distribution of saturated regions in the core

The Flux by CEDRAT's FEA allows the "incremental permeability" distribution in any object to be visualized. However, since the software does not operate hysteresis, this "incremental permeability" is not related to its definition presented in equation (2.5) but it is an

approximation to the differential permeability as it was shown in equation (5.5). Nevertheless, as it was already presented, it is important not to mistake these two terms. Therefore all the data presented in this work will be referred to as differential permeability.

The differential permeability distribution for the three constructed VIs is presented in Fig. 5.4. The figure also shows the H-field distribution of the EFD25 VI.

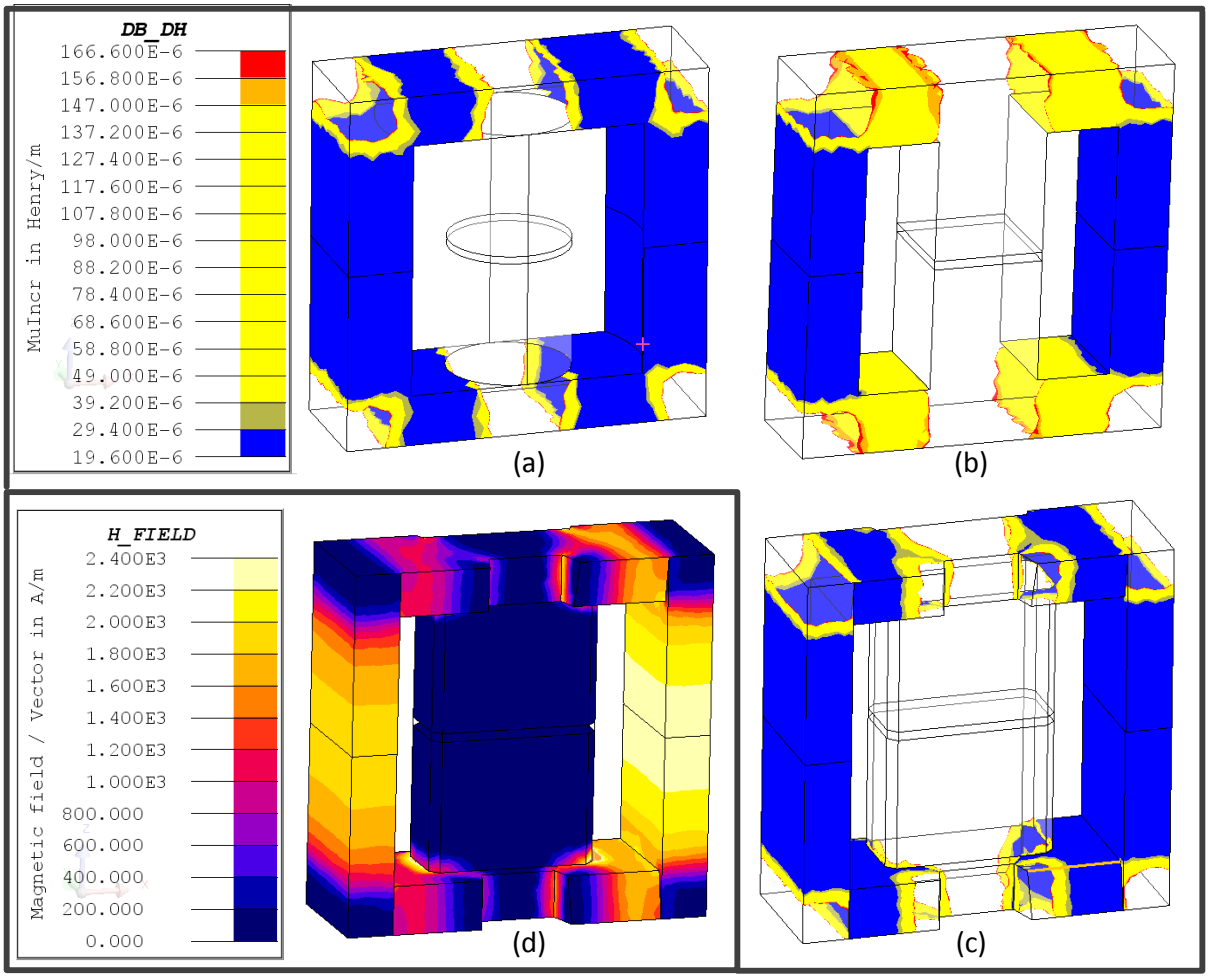

Fig. 5.4 (a-c) – Visualization of the differential permeability distribution of saturated regions for conditions of minimum main inductance. (a) ETD49 $i_{main} = 0.25\text{A}; \text{i}_{DC} = 1.5\text{A}$; (b) EF25 $i_{main} = 0.1\text{A}; \text{i}_{DC} = 0.7\text{A}$; (c) EFD25 $i_{main} = 0.1\text{A}; \text{i}_{DC} = 0.7\text{A}$. (d) – Visualization of the H-field distribution of (c)

In Fig. 5.4 (a-c) the differential permeability distribution of three different VIs is shown. Each VI is operating in conditions of minimum inductance (high value of DC current). The colour scale varies from $1.96E-5 \;\; H.m^{-1}$ to $16.66E-5 \;\; H.m^{-1}$, which corresponds to the slope variation of the N87 B(H) curve in the saturated region. Therefore the coloured areas correspond to the areas which are saturated. The transparent areas correspond to transition or unsaturated regions, whose differential permeability is too great for the scale represented. It is clear that the blue area, which is associated to a differential permeability variation within

approximately $2E-5\ \ H.m^{-1}$ to $3E-5\ \ H.m^{-1}$, is the dominant colour in these figures. In these figures, it is also interesting to observe that, in spite of the similar dimensions and operating conditions of the EF25 and EFD25 VIs, the differential permeability in the upper and bottom part of the core is different. The EFD25 has a bluer colour and the EF25 contains more yellow. This proves that the EFD25 is an optimized version of the EF25, which tends to maintain a more uniform differential permeability value in the DC flux path.

In Fig. 5.4 (d) the H-field distribution of the VI for the conditions of Fig. 5.4 (c) is shown. High magnetic field values are observable in this image. The N87 B(H) curve, showed previously in Fig. 3.7(a), has an H-field range of up to 1200A.m^{-1}. However, it is clear that the core operates with much higher fields which go up to 2400 A.m^{-1}. This is possible since the FEA software interpolates the B(H) curve in order to perform simulations for the unknown saturated regions. The software calculates the slope of the two last introduced spline points and extends it infinitely. Therefore, for N87 the software assumes a constant value of differential permeability for H-fields higher than 1000A.m^{-1} (flux version 10.4). In this case this is $1.96E-5$ H. m^{-1}. An error has obviously been committed in this interpolation, although it is believed to be small since the differential permeability tends to be constant in saturated fields.

A test was also performed to obtain the visualization of the differential permeability distribution of saturated regions for different air-gap values. The results were similar to Fig. 5.4 and proved to be independent of the air-gap size. This data can be found in the Appendix A.

Previously in Fig. 2.4 it was predicted that the areas associated with the DC flux path would be uniformly saturated, however they are not. It is now possible to observe that these areas are composed by an array of various differential permeability values which can be transposed into an array of different reluctance values. This creates a problem in the design of the proposed model, since it is necessary to find a mean differential permeability value. This "search" for the mean value can be simplified if the effect of the transition and unsaturated regions were to be neglected. It is acceptable to do so since the differential permeability of unsaturated regions is much higher than the saturated ones and the length of the areas associated to the transition region are too small when compared to the remaining ones. Therefore, making an analogy to electrical terms, the transparent areas of Fig. 5.4(a-c) correspond to "short-circuit zones" for the passage of magnetic flux, and the coloured areas are "resistivity zones". The length and mean differential permeability values of these "resistivity zones" will be calculated below.

5.2.2. Length of the saturated area

In order to calculate $\Re_{sat2}$ and $\Re_{sat3}$ it is necessary to calculate the length of the saturated region of the core. It was observed before that the differential permeability associated to saturated regions does not occupy the entire length of the DC flux path. Fig. 5.5 represents the top-left corner zoom of Fig. 5.4 (c).

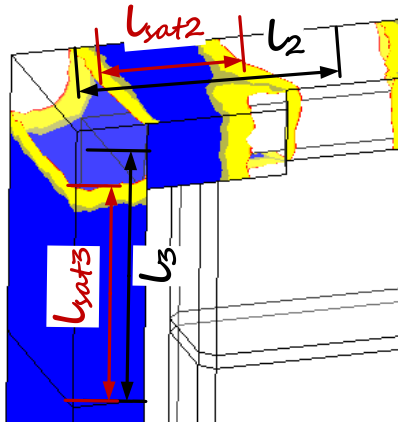

Fig. 5.5 Top-left corner zoom of an E-shaped core comparing the length values for classic reluctance model and the proposed one;

The intention of Fig. 5.5 is to demonstrate the difference between the length used in the calculation of $\Re$ and the length that will be used to calculate $\Re_{sat}$. The superimposed arrows exhibit the reduction between these two values. Equation (5.6) was created to calculate the length of the saturated area in the core associated to the path numbers two and three:

$$\begin{aligned} l_{sat2} &= \frac{comp3}{16} + \frac{(comp2 - comp3)}{2} + \frac{(comp1 - comp2)}{8} \\ l_{sat3} &= alt2 + \frac{(alt1 - alt2)}{4} \end{aligned} \tag{5.6}$$

where l_{sat2} and l_{sat3} are the length values of the magnetic paths two and three, previously defined in Fig. 2.5 (c) and Fig. 5.1, and $comp1, comp2, comp3, alt1$ and $alt2$ are the length values given by the factory, explained in detail in Fig. 3.2. This equation was tested and proved accurate for the ETD49, EFD25 and EF25 for different values of air-gaps. Therefore, it is believed that (5.6) is accurate for any other E-shaped VI since it respects the (2.10) design condition where: $B_{max} \approx [0.1B_{sat}; 0.3B_{sat}]$.

5.2.3. Mean value of the differential permeability estimate

The calculation of $\Re_{sat}$ requires the knowledge of the differential permeability value of the saturated areas. However, as observed in Fig. 5.4 (a-c), there is an array of values along the DC

path which make it impossible to consider all of them in the calculation. Therefore to maintain the simplicity of the model, a mean value has to be acquired. As there is no algorithm to calculate the mean permeability value, a methodology for E-shaped VIs based on the obtained results will be implemented.

It was observed in Fig. 5.4 (d) that, for minimum inductance conditions, the saturated regions of the material along the DC flux path, have an H-field variation between $300A.m^{-1}$ and $2400\mathrm{A.\,m^{-1}}$. This variation corresponds to a differential permeability variation between $16.66E-5\mathrm{H.\,m^{-1}}$ and $1.96E-5\mathrm{H.\,m^{-1}}$. It was also observed that the area of the core which had a magnetic field variation between 300A.m^{-1} and 400A.m^{-1} was too small, when compared with the total area of the core, (these results can be observed in Appendix A). In addition, it was noticed that the differential permeability variation decreased greatly with the increase of saturation. The following table, in which the mean differential permeability values for different H-fields are shown, highlights this observation:

TABLE 6
MEAN DIFFERENTIAL PERMEABILITY VALUES FOR THE N87 MATERIAL

	Non-Saurated	Saturated				
H-field $[H.m^{-1}]$	0-61.9	300-400	400-600	600-800	800-1000	> 1000
$\mu_d[A.m^{-1}]$	8.4E-3	~15.5E-5	~6E-5	~4E-5	~3E-5	~2E-5

Fig. 5.4 (a-c) also demonstrated that the majority of the differential permeability distribution along the DC flux path was situated within $1.96E{-}5A.m^{-1}$ and $2.94E{-}5A.m^{-1}$.

Taking all these statements into consideration, and relating TABLE 6 with Fig. 5.4 (a-d), it is possible to conclude that the mean differential permeability in saturated conditions, may be a value between $6E{-}5H.m^{-1}$ and $2E{-}5H.m^{-1}$, probably closer to the lower value than the higher one. Therefore, a value around $3E{-}5H.m^{-1}$ would be a good estimate for the ETD49 and EFD25. The EF25 VI should have a higher value, probably around $4E{-}5H.m^{-1}$, since the upper and bottom areas of the core are not blue. The reliability of this estimate will be tested further in this work. To estimate the differential permeability of other types of materials it is necessary to calculate the B(H) curve maximum and minimum slope of the saturated region. The user can select a value within that range knowing that the lower the differential permeability value is, the lower the minimum inductance obtained and therefore the greater the energy spent to saturate the core will be.

***Author note**: The purpose of this estimate is not to find the exact value that corresponds to the minimum inductance value of a specific VI setting, but to find the minimum inductance*

that can be obtained with that VI setting. There is not a single and correct mean differential permeability value for a specific VI setting, since it greatly depends on the VI saturation state, which in turn depends on the value of DC current and number of DC windings ($N_{DC} \cdot i_{DC}$). Therefore, for a given VI setting, a minimum inductance value is obtained and for the same setting in conditions of a greater DC current, an even lower value will be obtained. The presented estimate is intended to give users a notion of the inductance variation capability of a given VI setting. Thus, if they intend to spend less energy, they might choose a higher mean differential permeability value (for example $4E{-}5A.m^{-1}$), and if they intend to have a greater inductance variation they can choose a lower mean differential permeability value (for example $2.5E{-}5A.m^{-1}$). For the N87 material the chosen value must be within $6E{-}5H.m^{-1}$ and $2E{-}5H.m^{-1}$.

5.3. Adjustment of the VI reluctance model under saturation

With the knowledge acquired in the previous analysis, an adjustment to the proposed $\Re_{sat}$ equation(5.2) has to be implemented. It was proved that the differential permeability value μ_d is in accordance with the permeability definition. In the $\Re_{sat}$ equation instead of μ_{sat}, μ_{ds} will be used. This corresponds to the mean differential permeability value in the DC flux path for saturated conditions. It was also observed that the saturation is not evenly distributed along the DC flux path. Therefore the calculation of $\Re_{sat}$, l_2 must be replaced by l_{sat2} and l_3 by l_{sat3}, whose values are defined in (5.6). The reformulated $\Re_{sat}$ equation is as follows:

$$\Re_{sat\_i} = \frac{l_{sat\_i}}{\mu_{ds} \times A_i}, \; i = 2,3 \tag{5.7}$$

where $\Re_{sat\_i}$ is the equivalent reluctance of path i for saturated conditions and A_i is the cross section of the area of the path i [m^2].

From here on the calculation of the maximum and minimum inductance values of the VI is possible and it is defined in (5.8):

$$\begin{aligned} \mathrm{L}_{\max} &= \frac{N_{main}^2}{\Re_g + \Re_1 \times 2 + \Re_2 + \Re_3} \\ \mathrm{L}_{\min} &= \frac{N_{main}^2}{\Re_g + \Re_1 \times 2 + \Re_{sat2} + \Re_{sat3}} \end{aligned} \tag{5.8}$$

5.4. The most influential parameters in the inductance value

The knowledge of the maximum and minimum inductance equations made it possible to take a step forward and analyse which parameters of the VI triggered the inductance value. Several tests were performed in which a single parameter of the VI was changed and the effects analysed. The obtained results are presented in TABLE 7.

TABLE 7
CHANGES THAT TRIGGER EFFECTS IN THE INDUCTANCE VALUE.

Change	Effect
Number of turns	No change in the inductance ratio[8], only in the maximum and minimum inductance values.
Gap length	An increase in the gap size decreases the inductance ratio significantly.
Doubling $l1$	No change in the ratio. Slight decrease in L_{max} and L_{min}.
Doubling $l2$	Increase in the inductance ratio. Decrease of L_{min}. Almost no change in L_{max}.
Doubling $l3$	Increase in the inductance ratio. Decrease of L_{min}. Almost no change in L_{max}.
Doubling A1	Significant increase in the inductance ratio. Slight increase of $L_{min.}$. Significant increase in L_{max}.
Doubling A2	Slight decrease in the inductance ratio. Slight increase of L_{min}. Almost no change in L_{max}.
Doubling A3	Decrease in the inductance ratio. Increase of L_{min}. Almost no change in L_{max}.

The information presented in the previous table is not adequate to calculate the "optimal core shape" for a VI assembly as the changes effectuated were not accompanied by a checking of the VI operating conditions presented in the design procedure of chapter 2. For example, according to this table, the maximum ratio that is possible to be obtained corresponds to the lowest possible air-gap value. However a tiny air-gap might not fulfil all the necessary conditions for the VI operation. The lower the air-gap, the lower the main current has to be in order to guarantee the condition (2.10), where $B_{\max} < 0.3B_{sat}$. The same happens with the reduction of both A2 and A3 areas which will definitely increase the inductance ratio. However, a lower area in the DC flux path will make it easy to saturate, affecting the condition (2.10) which, in turn, reduces the maximum allowed current in the main winding. The purpose of the performed tests is to better understand the VI operation. From now on, it is possible to create an algorithm that calculates the optimal core choice knowing the following statements:

- The smaller the core, the cheaper.

[8] Inductance ratio is the quotient between the maximum and minimum inductance value.

- The main winding turn number does not affect the inductance ratio.
- The smaller the air-gap, the bigger the inductance ratio.
- The bigger the core dimension, the bigger the inductance ratio.
- The main winding must guarantee condition (2.10): $B_{\max} < 0.3B_{sat}$.
- The main and DC windings must fit within the core's available space, which is given by (2.16): $l_w \geq \tau_{main} + \tau_{DC}$.

Before creating an algorithm based on these conditions it is necessary to prove the reliability of the model, which will be done below. An algorithm proposal will then be presented.

5.5. Reliability of the proposed VI reluctance model

To prove the reliability of this model, two tests were conducted where the maximum and minimum inductance value obtained w put to the test with the results obtained previously in the FEA simulation. The results acquired are summed up in the following table:

TABLE 8
INDUCTANCE COMPARISON BETWEEN THE FEA SOFTWARE SIMULATION AND THE PROPOSED MODEL FOR DIFFERENT CORE STRUCTURES AND AIR-GAPS.
(all values are in s.i units with the exception of the air-gap length which is in millimetres.)

		EFD25			EF25			ETD 49				
		Gap=0.1	Gap=0.6	Gap=1	Gap=0.1	Gap=0.6	Gap=1	Gap=0.1	Gap=0.3	Gap=0.6	Gap=1	Gap=1.5
FEA	L_{max}	6.41E-04	1.37E-04	8.89E-05	6.15E-04	1.32E-04	8.66E-05	1.75E-02	6.26E-03	3.98E-03	2.45E-03	1.60E-03
	L_{min}	5.40E-05	4.23E-05	3.64E-05	7.65E-05	5.30E-05	4.26E-05	8.51E-04	7.26E-04	8.45E-04	6.59E-04	5.93E-04
	RT	11.86	3.23	2.44	8.04	2.49	2.03	20.58	8.63	4.72	3.72	2.69
	N	27			27			70				
SRM - T.1	L_{max}	6.43E-04	1.36E-04	8.88E+01	6.15E-04	1.32E-04	8.67E-05	1.75E-02	6.26E-03	3.98E-03	2.45E-03	1.60E-03
	L_{min}	5.41E-05	4.23E-05	3.64E+01	7.65E-05	5.30E-05	4.27E-05	8.51E-04	7.26E-04	8.44E-04	6.58E-04	5.93E-04
	RT	11.90	3.22	2.44	8.04	2.48	2.03	20.56	8.62	4.72	3.73	2.69
	N	31	33.6	34.9	30.9	33.7	35.2	86.5	85	94.5	95.2	93.8
	μ_i		0.0084			0.0084				0.0084		
	μ_{ds}	**3.27E-05**	**2.89E-05**	**2.70E-05**	**5.21E-05**	**4.46E-05**	**3.87E-05**	**3.06E-05**	**2.91E-05**	**3.07E-06**	**2.54E-05**	**2.75E-05**
SRM - T.2	L_{max}	8.20E-04	1.48E-04	8.93E-05	7.89E-04	1.42E-04	8.57E-05	1.94E-02	7.17E-03	3.69E-03	2.24E-03	1.50E-03
	L_{min}	6.37E-05	4.71E-05	3.89E-05	7.75E-05	5.35E-05	4.29E-05	9.24E-04	8.55E-04	7.68E-04	6.77E-04	5.90E-04
	RT	12.88	3.14	2.29	10.19	2.65	2.00	20.96	8.39	4.80	3.31	2.55
	N	35			35			91				
	μ_i	0.0084			0.0084			0.0084				
	μ_{ds}	3.00E-05			4.00E-05			3.00E-05				

There are two main proprieties that may influence the model results. The first is number of turns of the main winding N_{main}, since, as previously observed, there is a deviation between the value obtained with the classic reluctance model and the FEA simulation. The second property is the differential permeability for saturated conditions μ_{ds}, because it is not a "fixed" value but an estimated one. Therefore, the first test intends to adjust these two values in order to match the maximum and minimum inductance obtained values, both with the proposed model and the FEA software. The goal is to verify that there is not a great variation in the N_{main} value and that μ_{ds} is set between $6E{-}5H.m^{-1}$ and $2E{-}5H.m^{-1}$. The second test intends to establish a fixed value for N_{main} and μ_{ds} and ensure there is not a great deviation in the inductance ratio.

TABLE 8 is split into three set of columns, each one corresponding to a different core structure indicated in the top row. Each set is sub-divided into three or five columns, with each one containing values for different core air-gap sizes indicated in the second row. The table is also split into three main rows. The top main row, named "FEA" corresponds to the results obtained with the FEA software, previously presented and analysed in TABLE 4. The middle and bottom main rows named "SRM – T.1" and "SRM – T.2", present the results for two different tests conducted with the proposed reluctance model for saturated conditions. Each main row set is sub-divided in either three or six rows. The following table acronyms apply: RT stands for Ratio, which corresponds to the quotient between the maximum and minimum inductance values for each row set; N is the number of turns of the main winding; $L_{\max}$ and $L_{\min}$ is the maximum and minimum inductance obtained with the saturated reluctance model; μ_i is the initial permeability and μ_{ds} is the mean saturated differential permeability.

The first test was conducted to nullify the deviations observed between the number of windings in the simulation and the reluctance model. Therefore, the number of windings turns was adjusted so that $L_{\max}$, obtained with equation (5.8), matched the value obtained with simulation. As can be seen in "SRM – T.1" and "FEA" tests, the same value is present for both $L_{\max}$ figures. Following this, the value of μ_{ds} was tuned so that $L_{\min}$ matched the value obtained in the FEA software. As can be observed, these two values are approximately equal. In addition, all core types and different air-gap dimensions the μ_{ds} values are between $6E{-}5H.m^{-1}$ and $2E{-}5H.m^{-1}$ which proves the reliability of the differential permeability definition. Furthermore, the differential permeability for saturated conditions of the EF25 has a higher value than the other two cores, as was previously predicted and observed in Fig. 5.4 (a-c). Finally, the saturated differential permeability of the EFD25 for a $0.6mm$ air-gap and the

ETD49 for a $1mm$ air-gap is close to the value estimated before ($3E{-}5H.m^{-1}$), proving, one more time, the reliability of this algorithm.

The second test was conducted to represent the reliability of the model in the presence of user-made choices. Therefore, a fixed value for the number of winding turns and differential permeability in saturated conditions was chosen. The differential permeability value was chosen according to the previously estimated value for each VI. The EFD25 and EF25 N_{main} value is equal to 35 since it corresponds to the value calculated by M.Martins. In order to calculate the ETD49 main windings' turn number, the proportion between the EFD25 VI simulated and calculated N_{main} value was maintained. Therefore a value of 91 turns was chosen. There is a deviation in L_{max} and L_{min} values, as it is possible to observe, but there is an even smaller deviation in the ratio value. A small ratio deviation is very important since the ratio determines the capability of the inductance variation of the VI. Moreover, having an accurate ratio value makes the deviations, observed in L_{max} and L_{min}, being less relevant since they can be easily corrected after the VI assembly, through the adjustment of the N_{main} value. This test therefore, proves that even though the users do not know the correct mean value of the differential permeability for saturated conditions, they can still design an accurate VI with the presented model, and the only essential parameter that needs adjusting after the VI assembly is the number of turns of the main winding.

5.6. New design methodology proposal

Since it is now possible to calculate both maximum and minimum inductance values, a new design methodology will be proposed. Similarly to the previously presented design methodology, the process begins by selecting the core type, material and dimensions. However, now the desirable maximum and minimum inductance value must also be selected. The following proposal was formed assuming that it is possible to control the inductance range and ratio by simply varying the main winding number of turns and the air-gap length respectively. Therefore, the presented methodology is adapted to return the correct air-gap value and number of winding turns in order to create the desired VI. The design is based on the former procedure, presented in Chapter 2, with additions regarding the proposed reluctance model. It is divided into six steps shown below:

- *First step*: To extract the some material proprieties. Initially it is necessary to establish a saturation point and extract its respective saturated magnetic field H_{sat} and flux density B_{sat} values as shown in Fig. 5.6. This point must have an high H-field value. Typically the point of

the B(H) curve with higher saturation level is selected. This point will be used to calculate the number of turns of DC windings. After the selection of the point it is possible to calculate μ_{sat} as shown in the equations list in (5.9). The value of initial permeability μ_i must then be extracted. Usually the material datasheet contains a standard value for μ_i or μ_{ri} (relative initial permeability). However, as explained before, it is strongly recommended not to use any of these values in this procedure. These values were calculated by the factory and include the hysteresis effect of an initial magnetization. When the core receives its first magnetization, the material responds with a lower value of permeability for low H-fields and only then it increases to a higher value. It is this "higher value" that is required to implement the proposed design procedure and Fig. 5.6 shows how to obtain it. Finally it is necessary to estimate the mean differential permeability μ_{ds} . There is not an algorithm to calculate this value accurately, and, after several attempts, no relation was found between μ_{ds} and the chosen saturation point. Research in this area is ongoing. A summary of these proprieties is shown in Fig. 5.6 and in equation list (5.9):

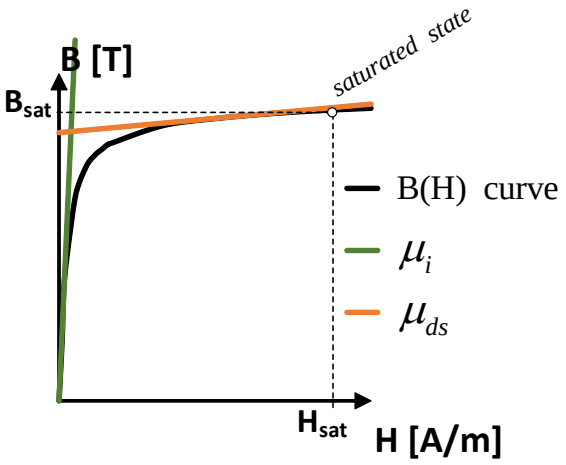

Fig. 5.6 – B(H) curve with superimposed differential permeability slopes and selected saturated mean point of operation

$$\mu_{sat} = \frac{B_{sat}}{H_{sat}}$$
$$\mu_i = \lim_{H \to 0} \frac{B}{H}$$
$$\mu_{ds} = \frac{dB_{sat}}{dH_{sat}} \qquad (5.9)$$
$$\mu_{ri} = \frac{\mu_i}{\mu_0}$$
$$\mu_{r\_ds} = \frac{\mu_{ds}}{\mu_0}$$

where, μ_{r_ds} is the relative differential permeability for saturated conditions. For the N87 material the following was verified: $\mu_i = 8.4E{-}3 H.m^{-1}$ and $\mu_{ds} = [6E{-}5; 2E{-}5] H.m^{-1}$.

- *Second step*: To find the proper air-gap length that corresponds to the desired inductance ratio. Due to the symmetry of the E-shaped cores, it is possible to apply the following simplifications:

$$A_g = A_1$$
$$A_2 \simeq A_3 \simeq \frac{A_1}{2} \qquad (5.10)$$

Considering (5.10) the air-gap length can be calculated as shown in (5.11) deduction:

$$RT = \frac{L_{\max}}{L_{\min}} = \frac{\dfrac{N_{main}{}^2}{\Re_g + \Re_1 \times 2 + \Re_2 + \Re_3}}{\dfrac{N^2}{\Re_g + \Re_1 \times 2 + \Re_{2sat} + \Re_{3sat}}} = \frac{\Re_g + \Re_1 \times 2 + \Re_{2sat} + \Re_{3sat}}{\Re_g + \Re_1 \times 2 + \Re_2 + \Re_3} =$$

$$= \frac{\dfrac{g}{\mu_0 A_g} + \dfrac{l_1}{\mu_{ri}\mu_0 A_1} \times 2 + \dfrac{l_{sat2}}{\mu_{r\_ds}\mu_0 A_2} + \dfrac{l_{sat3}}{\mu_{r\_ds}\mu_0 A_3}}{\dfrac{g}{\mu_0 A_g} + \dfrac{l_1}{\mu_{ri}\mu_0 A_1} \times 2 + \dfrac{l_2}{\mu_{ri}\mu_0 A_2} + \dfrac{l_3}{\mu_{ri}\mu_0 A_3}} \tag{5.11}$$

$$\Updownarrow$$

$$g = -2 \times \frac{\mu_{ri}\left(l_{sat2} + l_{sat3}\right) + \mu_{r\_ds} \times l_1 - \mu_{r\_ds} \times RT \times \left(l_1 + l_2 + l_3\right)}{\mu_{ri} \times \mu_{r\_ds}\left(1 - RT\right)}$$

where RT is the ratio between the maximum and minimum desired inductance. As can be observed, to calculate the air-gap length it is necessary to know l_1, which is a value that itself depends on the length of the air-gap. It is possible to solve this problem by matching l_1 with l_3 as the error committed is negligible. The final expression of calculation of the the air-gap, assumes the following form:

$$g = -2 \times \frac{\mu_{ri}\left(l_{sat2} + l_{sat3}\right) + \mu_{r\_ds} \times l_3 - \mu_{r\_ds} \times RT \times \left(l_2 + l_3 \times 2\right)}{\mu_{ri} \times \mu_{r\_ds}\left(1 - RT\right)} \tag{5.12}$$

At this point, regardless of the main winding number of turns, the final inductor will have the ratio corresponding to the quotient of the desired maximum and minimum inductance values. In order to have an inductor, not only with the correct ratio but also with the desired inductance reach, it is necessary to calculate the number of turns. This procedure will be explained in the next step.

If a case arises where it is impossible to construct a core with the calculated air-gap, then the closest lowest possible air-gap must be selected. If there is not a lower one available, then a bigger core must be selected and the user must return to the first step.

- *Third step*: To calculate the number of turn of the main winding in order to obtain the desired inductance values. As was observed before, the change in the main winding number of turns does not change the ratio between maximum and minimum inductance. Considering the simplifications in (5.10) and the calculation of the air-gap in (5.12), the number of turns of the main winding can be calculated as expressed in equation (5.13):

$$L_{\max} = \frac{N_{main}^2}{\Re_g + \Re_1 \times 2 + \Re_2 + \Re_3} = \frac{N_{main}^2}{\frac{g}{\mu_0 A_g} + \frac{l_1}{\mu_{ri}\mu_0 A_1} \times 2 + \frac{l_2}{\mu_{ri}\mu_0 A_2} + \frac{l_3}{\mu_{ri}\mu_0 A_3}}$$

$$\Updownarrow \tag{5.13}$$

$$N_{main} = \sqrt{\frac{L_{\max}}{\mu_0 A_1}\left[g + \frac{2}{\mu_{ri}}(l_1 + l_2 + l_3) \right]}, N_{main} > 0$$

- *Fourth step:* To guarantee that the VI can operate with the obtained g and N_{main} values. As observed in (2.10), a VI must respect the following condition:

$$B_{\max} \leq B_{sat} \tag{5.14}$$

To fulfil this rule, the maximum peak current must be limited as shown by inequation (5.15):

$$i_{\max} \leq \frac{\Re_{total} \cdot A_1 \cdot 0.3 \cdot B_{sat}}{N_{main}} \tag{5.15}$$

If the previous condition cannot be fulfilled, a bigger core must be selected and the process repeated from the first step.

- *Fifth step:* To calculate the DC winding number of turns. With the knowledge of the saturation distribution of the core, the factor k of the previous equation presented in (2.15) can be eliminated and the length of the external path l_{ext} replaced by the length of the path that is saturated. Therefore the DC number of turns can be determined by equation (5.16):

$$N_{DC} = \frac{1}{2} \frac{B_{sat} \cdot 4 \cdot (l_{sat2} + l_{sat3})}{\mu_{sat} \cdot i_{dc\_\max}} \tag{5.16}$$

where l_{sat2} and l_{sat3} can be calculated with the expression presented in (5.6).

Note: Equation (5.16) incorporates the saturated permeability value and not the differential permeability for saturated states, since the magnetic flux responsible to create the saturation is produced by itself and not by other winding. This equation is equivalent to equation (2.15) which was calculated in [22], [24], [42] but wrongly applied in [22]. In this work it was verified that the value retuned by this equation was approximately four times lower than the pretended one. In addition, a relationship has not yet been found between the permeability and the differential permeability for saturated regions. Research in this area is still being conducted.

- *Sixth step:* To guarantee the main and DC windings fit in the core winding area. Once the correct number of turns of DC and main windings are known it is possible to verify that the

coils fit in the available core space. Therefore equation (2.16) must be verified, as repeated below:

$$l_w = \frac{comp2 - comp3}{2} \geq \tau_{main} + \tau_{DC} \tag{5.17}$$

where the thickness of each winding τ can be calculated with equation (3.7), which is shown below:

$$\tau = \left\{ \text{int}\left[\frac{N}{\text{int}\left(\frac{h}{r}\right)} + 0.(9) \right] - 1 \right\} \cdot r \cdot \sqrt{3} + 2r \tag{5.18}$$

If the condition of (5.17) is not verified, a larger core must be selected.

A summary schematic of this algorithm can be found in Appendix C.

5.7. Labview app

Based on the proposed model, a Labview program was built to calculate the maximum and minimum inductance values for any VI double E-core type topology. The app uses the proposed reluctance model in order to calculate the minimum inductance. More details about this program can be found in Appendix D.

CHAPTER 6 – Conclusions and future work

This final chapter presents the conclusions related to the electromagnetic study of a variable inductor and the contributions of this work. As conclusions, the main goals that were achieved will be emphasized in this chapter and special attention will be given to future work.

6.1. Conclusions and main contributions

The conclusions presented in this Master's Thesis may be detailed as follows:

FEA software model

During the construction process of the VI model, it was necessary to deal with several limitations that threatened the accuracy of the model, such as: lack of information about the operation of the N87 material for H-fields higher than1200A.m^{-1}; lack of the spline curve values of the initial B(H) magnetization curve; the generation of a good mesh rather than an excellent one, due to time constraints. In spite of all these limitations, the magnetostatic and transient analysis demonstrated that the constructed FEA model of the EFD25 VI is an accurate replica of the real model. The small-signal and large-signal inductance curves observed in Fig. 4.6 and Fig. 4.13, show an agreement between the simulation and experimental results which proves the reliability of the model and certifies the electromagnetic analysis conducted.

VI electromagnetic behaviour

The electrostatic analysis conducted in Chapter 4 demonstrated that a single current in the DC winding generated a magnetic flux looping along the external path (or DC flux path). Due to the VI design no DC generated flux in the central arm was not found, (except a residual value). It was also verified that the current in the main winding generated a magnetic flux in the central and outer arms as predicted in Chapter 2. Also, Fig. 4.1 (a), Fig. 4.2(a), Fig. 4.7(a) and Fig. 4.8(a) showed that the maximum i_{main} value was not enough to saturate any part of the core. This happened due to the condition $B_{\max} < 0.3B_{sat}$ presented in the design equation (2.10) . Another observation was the unbalance in the flux density module between right and left arms of the core, when both DC and main currents were applied. It was concluded that the flux

unbalance was the result of the superposition of main and DC magnetic flux in the outer arms, which had the same direction in one arm and opposite direction in the other. Finally the simulation conducted to the different air-gap values, allowed to conclude that the smaller the air-gap, the higher is the ratio between the maximum and minimum inductance.

A transient analysis was conducted in Chapter 4. The EFD25 VI was inserted in a RSCC circuit designed to control the power level of a 22W LED lamp. In the analysis conducted for Fig. 4.10 and Fig. 4.11 it was concluded that the inductance variation of the VI was not related to the variation of the magnetic flux in the main winding but to the variation of main current value ($L = \Psi / i$). It was also verified that there is an oscillation in the inductance value through the time with twice the frequency of f_s, when a DC current is applied. The inductance oscillation amplitude also decreases with the increase of the saturation state of the core. Finally a simulation was performed to observe the large-signal inductance variation. It was concluded that L_{main} mainly depends on the DC current value and not on the operation state of the resonant circuit. Moreover, the L_{main} response time to a DC current step was observed to be immediate.

In Chapter 5 some breakthroughs in the electromagnetic analysis of the VI were made. It was verified that the magnetic permeability equation was not in accordance with its definition and thus had no practical application in the analysis of non-linear multi-winding circuits. It was discovered that the solution relies in the differential permeability equation. The differential permeability of a material is the property that correctly describes "**the ease** with which the magnetic flux flows through" it. The differential permeability equation allowed to observe the magnetic circuit behaviour with a different perspective. Fig. 5.4 (a-c) showed that the saturation was not evenly distributed along the DC flux path and some areas of this path were not saturated at all. It was also observed that the EFD25 is an optimized version of the EF25, since it better controls the saturation distribution in the outer arms of the core. The ETD family demonstrated to possess a similar behaviour to the EFD core, since both had a similar magnetic saturation distribution. Having the knowledge of the capability of the differential permeability in accurately representing the behaviour of a magnetic circuit, a proposal of a new reluctance model was made, allowing to calculate the VI's inductance value for saturated conditions. Tests were conducted in which the effect triggered in the inductance value after the implementation of a physical change in the core was observed. Among other observations, the results presented in TABLE 7 demonstrated that the number of turns does not influence the inductance ratio, contrary to the air-gap length which greatly affects it.

In conclusion the main contributions may be detailed as follows:

- The equation to find the minimum inductance value of the VI was found.

  Until now, variable inductors were designed and tuned to have a desired maximum inductance value. However, there was no method to predict the amount of inductance variation of the VI. This represented a problem to all designers, since they first had to built the VI and only then conduct experimental tests to discover L_{min}. This thesis presented the solution to that problem.

- A new VI design methodology was proposed.

  The knowledge of the L_{min} equation allowed to implement a new design methodology which selects the best core and VI characteristics in order to get an optimized VI (smallest core volume) with the desired inductance variation.

- A Labview software was created to calculate the VI characteristics according to the user desired inductance variation.

  The software allows to quickly calculate the L_{max} and L_{min} values of any E-shaped VI, without the need to manually solve the respective equations. In addition, a second version of the software was implemented in which was included part of the design methodology proposal. This version allows any user to quickly calculate the air-gap length and N_{main} value for the desired VI. More information about this software can be found in Appendix D.

- An improvement to the classic reluctance model was proposed.

  From now on, it is possible to use the reluctance model to study every magnetic system regardless of the number of *mmf* sources and the non-linearity of the materials. The replacement of the magnetic permeability with the differential permeability in the reluctance equation, opens new borders to apply the model in many other applications.

- A solution to better understand the behaviour of magnetic circuits was found, which consists of the use of the differential magnetic permeability term instead of the magnetic permeability.

  The knowledge of the differential magnetic permeability property of a material proved to be fundamental in the study of the operation of Variable Inductors. Certainly, this concept will also be useful for the study of other devices that have non-linear magnetic materials. The literature review around this term demonstrated a general lack of information about the differential permeability capabilities. Besides, no reference was found in which the

differential permeability was used to replace the magnetic permeability in order to study the operation of magnetic circuits. Therefore this work proved to be singular and pioneer in this area.

- A detailed finite element electromagnetic analysis was presented allowing to understand the behaviour of VI's under static and dynamic conditions.

  The constructed VI models were designed to be easily adaptable to any application. The core was programed to assume any other size within its family. From now on, the construction of any other EFD, EF or ETD VI is possible by simply indicating the dimensions presented in the datasheet. The models were also programed to automatically resize each winding according to the used number of turns and wire radius. The infinity box size, the filing factor, resistivity and mass density value were also programed to be automatically calculated. These model enable the detailed electromagnetic study of any type of double E-shaped core.

- A paper has been accepted and presented at IEEE Industry Applications Society (IAS) Meeting 2015:

  Perdigão, M.S.; **Ferreira, S.F.**; Martins, M.; Mendes, A.S.; Alonso, J.M., "Finite element analysis of a variable inductor for an RSCC based LED lamp driver," in *Industry Applications Society Annual Meeting, 2015 IEEE* , vol., no., pp.1-8, 18-22 Oct. 2015
  doi: 10.1109/IAS.2015.7356874

- An extended version of the previous paper is being submitted to the IEEE Transactions on Industry Applications.

6.2. Future work

The main subject of this work was to realize an electromagnetic analysis of VI's operation. In terms of future work an extension of the already published paper is planned to be included in the IEEE Transactions on Industry Applications. Two more papers are intended to be published based on the work presented in this thesis. In the first paper a review the concept of magnetic permeability explaining its limitations with regard to the analysis of magnetic circuits is intended. Also, it intends to introduce the concept of differential permeability in response to the magnetic permeability. In the second paper, the new design methodology will be presented.

During the year of 2016 it is intended to realize an electromagnetic study of a different VI's topology, which contains two toroidal cores instead of an E-shaped one. The operation of the toroidal VI is different than the one presented in this thesis.

Besides the planned future work, it would be relevant to proceed in the following directions:

- Realize an electromagnetic study of the variable transformer introduced in [42] using the FEA software.
- Conduct a space efficiency and economical study to understand which topology (E-shaped and toroidal) best suits each application.
- Some applications might require a VI operating at minimum inductance conditions for the majority of the timeframe. In order to save energy, in the research group at IT it was suggested to introduce magnets inside the external arms of the core, which in turn will create the flux loop which saturates the core. In this case the DC windings would be used to counteract the magnet flux density in order to decrease the magnetic saturation of the core and increase the inductance of the main winding. It would be of interest to conduct an electromagnetic study of this proposed topology.
- As it was observed in this study, a good equation which relates the DC number of turns with the magnetic saturation of the core was not yet discovered. Research in this area is still needed to create an efficient algorithm which calculates the optimal core and VI characteristics for E-shaped cores and other topologies.

REFERENCES

[1] A. S. Kislovski, "Quasi-linear controllable inductor," *Proc. IEEE*, vol. 75, pp. 267–269, 1987.

[2] O. Ichinokura, M. Maeda, M. Sakamoto, K. Mitamura, T. Ito, and T. Saito, "Development of 3-phase 100 kVA orthogonal-core type variable inductor with sinusoidal output," *IEEE Trans. Magn.*, vol. 34, no. 4, pp. 2066–2068, Jul. 1998.

[3] K. Nakamura, O. Ichinokura, M. Maeda, S. Akatsuka, K. Takasugi, and H. Sato, "Analysis of orthogonal-core type linear variable inductor and application to VAr compensator," *IEEE Trans. Magn.*, vol. 36, no. 5, pp. 3565–3567, 2000.

[4] L. Zhang, W. G. Hurley, and W. H. Wölfle, "A New Approach to Achieve Maximum Power Point Tracking for PV System With a Variable Inductor," *IEEE Trans. Power Electron.*, vol. 26, no. 4, pp. 1031–1037, Apr. 2011.

[5] D. Medini and S. Ben-Yaakov, "A current-controlled variable-inductor for high frequency resonant power circuits," in *Proceedings of 1994 IEEE Applied Power Electronics Conference and Exposition - ASPEC'94*, 1994, pp. 219–225.

[6] J. M. Alonso, M. A. Dalla Costa, M. Rico-Secades, J. Cardesin, and J. Garcia, "Investigation of a New Control Strategy for Electronic Ballasts Based on Variable Inductor," *IEEE Trans. Ind. Electron.*, vol. 55, no. 1, pp. 3–10, Jan. 2008.

[7] L. Huber and M. M. Jovanović, "Single-Stage, Universal-Input AC/DC LED Driver With Current-Controlled Variable PFC Boost Inductor," *IEEE Trans. Power Electron.*, vol. 27, no. 3, pp. 1579–1588, Mar. 2012.

[8] R. A. Pinto, J. M. Alonso, M. S. Perdigao, M. F. da Silva, and R. N. do Prado, "A new technique to equalize branch currents in multiarray LED lamps based on variable inductor," in *2014 IEEE Industry Application Society Annual Meeting*, 2014, pp. 1–9.

[9] W. N. Carr, "A micro variable inductor chip using MEMS relays," in *Proceedings of International Solid State Sensors and Actuators Conference (Transducers '97)*, 1997, vol. 2, pp. 1137–1140.

[10] Y. Yokoyama, T. Fukushige, S. Hata, K. Masu, and A. Shimokohbe, "On-Chip Variable Inductor Using Microelectromechanical Systems Technology," *Jpn. J. Appl. Phys.*, vol. 42, no. Part 1, No. 4B, pp. 2190–2192, Apr. 2003.

[11] K. Okada, H. Sugawara, H. Ito, K. Itoi, M. Sato, H. Abe, T. Ito, and K. Masu, "On-Chip High-Q Variable Inductor Using Wafer-Level Chip-Scale Package Technology," *IEEE Trans. Electron Devices*, vol. 53, no. 9, pp. 2401–2406, Sep. 2006.

[12] S. Zhou, X.-Q. Sun, and W. N. Carr, "A monolithic variable inductor network using microrelays with combined thermal and electrostatic actuation," *J. Micromechanics Microengineering*, vol. 9, no. 1, pp. 45–50, Mar. 1999.

[13] P. Park, C. S. Kim, M. Y. Park, S. D. Kim, and H. K. Yu, "Variable Inductance Multilayer Inductor With MOSFET Switch Control," *IEEE Electron Device Lett.*, vol. 25, no. 3, pp. 144–146, Mar. 2004.

[14] Y. Ito, Y. Yoshihara, H. Sugawara, K. Okada, and K. Masu, "A 1.3-2.8 GHz Wide Range

CMOS LC-VCO Using Variable Inductor," in *2005 IEEE Asian Solid-State Circuits Conference*, 2005, pp. 265–268.

[15] E. Süli, "Lecture Notes on Finite Element Methods for Partial Differential Equations." Mathematical Institute University of Oxford, p. 5, 2012.

[16] R. Courant, "Variational methods for the solution of problems of equilibrium and vibrations," *Bull. Am. Math. Soc.*, vol. 49, no. 1, pp. 1–24, Jan. 1943.

[17] M. ZLÁMAL, "On the Finite Element Method.," *Numer. Math.*, vol. 12, pp. 394–409, 1968.

[18] G. W. Slade, "Fast finite-element solver for a reluctance mass accelerator," *IEEE Trans. Magn.*, vol. 42, no. 9, pp. 2184–2192, Sep. 2006.

[19] "Maxwell's Equations." [Online]. Available: http://www.maxwells-equations.com/. [Accessed: 28-Oct-2015].

[20] J. C. Maxwell, "On Physical Lines of Force," *London, Edinburgh, Dublin Philos. Mag. J. Sci.*, vol. 21, no. I,II, pp. 161–157, 281–291, 338–348.

[21] J. C. Maxwell, "On Physical Lines of Force," *London, Edinburgh, Dublin Philos. Mag. J. Sci.*, vol. 23, no. III, IV, pp. 12–24, 85–95.

[22] M. Martins, "LED Lamp Driver Based on a Resonant Switched Capacitor Converter with a Variable Resonant Tank," Universidade de Coimbra, 2015.

[23] M. Martins, M. S. Perdigao, A. S. Mendes, R. A. Pinto, and J. M. Alonso, "Dimmable LED driver with variable inductor based on a resonant switched-capacitor topology," in *2015 IEEE Energy Conversion Congress and Exposition (ECCE)*, 2015, pp. 5329–5336.

[24] M. S. F. S. F. . M. M. M. A. S. A. J. M. Perdigão, "Finite Element Analysis of a Variable Inductor for an RSCC based LED Lamp Driver," 2015.

[25] P. J. Sweeney and II, *CompTIA RFID+ Study Guide: Exam RF0-101*. John Wiley & Sons, 2006.

[26] S. Zurek, "Effective magnetic permeability [Encyclopedia Magnetica]," *2015*. [Online]. Available: http://www.encyclopedia-magnetica.com/doku.php/effective_magnetic_permeability. [Accessed: 30-Oct-2015].

[27] A. Van den Bossche and V. C. Valchev, *Inductors and Transformers for Power Electronics*. 2005.

[28] C. R. Nave, "Inductance of a coil." [Online]. Available: http://hyperphysics.phy-astr.gsu.edu/hbase/magnetic/indcur.html. [Accessed: 30-Oct-2015].

[29] L. O.Chua, *Linear and Non-Linear Circuits:* McGraw-Hill Inc.,US; New edition edition (Oct. 1987), 1987.

[30] Magnetics®, "Learn More Shapes." [Online]. Available: http://www.mag-inc.com/products/ferrite-cores/ferrite-shapes/learn-more-shapes. [Accessed: 04-Dec-2015].

[31] "Magnetic core." [Online]. Available: https://en.wikipedia.org/wiki/Magnetic_core#.22E.22_core. [Accessed: 04-Dec-2015].

[32] Z. Dang and J. A. Abu Qahouq, "Evaluation of High-Current Toroid Power Inductor With NdFeB Magnet for DC–DC Power Converters," *IEEE Trans. Ind. Electron.*, vol. 62, no.

11, pp. 6868–6876, Nov. 2015.

[33] Q. Chen, L. Xu, X. Ruan, S. C. Wong, and C. K. Tse, "Gyrator-Capacitor Simulation Model of Nonlinear Magnetic Core," in *2009 Twenty-Fourth Annual IEEE Applied Power Electronics Conference and Exposition*, 2009, pp. 1740–1746.

[34] G. W. Ludwig and S.-A. El-Hamamsy, "Coupled inductance and reluctance models of magnetic components," *IEEE Trans. Power Electron.*, vol. 6, no. 2, pp. 240–250, Apr. 1991.

[35] "Ferrites and accessories - SIFERRIT material N87." EPCOS, p. 7, 2006.

[36] D. Zhang, Y. Zhou, P. Yan, T. Shao, and Y. Sun, "Differential permeability of ferrite cores at high magnetization rates," in *2010 IEEE International Power Modulator and High Voltage Conference*, 2010, pp. 517–520.

[37] M. Jaafar, V. Markovski, and M. Elleuch, "Modelling of the differential permeability and the initial magnetization curve for ferromagnetic materials," in *2004 IEEE International Conference on Industrial Technology, 2004. IEEE ICIT '04.*, 2004, vol. 1, pp. 460–465.

[38] J. P. A. Bastos and N. Sadowski, "A New Formulation Using Differential Permeability Based on the Source-Field Method," *IEEE Trans. Magn.*, vol. 46, no. 8, pp. 3369–3372, Aug. 2010.

[39] J. P. A. Bastos, N. Sadowski, J. V. Leite, N. J. Batistela, K. Hoffmann, G. Meunier, and O. Chadebec, "A Differential Permeability 3-D Formulation for Anisotropic Vector Hysteresis Analysis," *IEEE Trans. Magn.*, vol. 50, no. 2, pp. 341–344, Feb. 2014.

[40] W. G. Hurley and W. H. Wölfle, *TRANSFORMERS AND INDUCTORS FOR POWER ELECTRONICS*. John Wiley & Sons Ltd, 2013.

[41] T. Nehl, F. Fouad, and N. Demerdash, "Determination of Saturated Values of Rotating Machinery Incremental and Apparent Inductances by an Energy Perturbation Method," *IEEE Trans. Power Appar. Syst.*, vol. PAS-101, no. 12, pp. 4441–4451, Dec. 1982.

[42] M. S. Perdigao, "Research and Development on New Control Techniques for Electronic Ballasts based on Magnetic Regulators," Universidade de Coimbra, 2011.

APPENDIX A: SPECIFICATIONS OF THE STUDIED VIS

A.1 ETD 49 VI

An ETD49 VI was initially designed by a colleague named Valter Martins. It was projected to be inserted into a resonant circuit to control the charging current of an electric car battery. Meanwhile, the chosen resonant circuit topology was abandoned and a new one is currently being investigated. However, a FEA model of the ETD49 VI was built and its characteristics and simulations results are presented below.

General properties

Material: N87; $\mathbf{N_{dc}}$**:** 86; $\mathbf{N_{ac}}$:70; **Inductance variation:** 566µH ~ 154µH

Core Shape

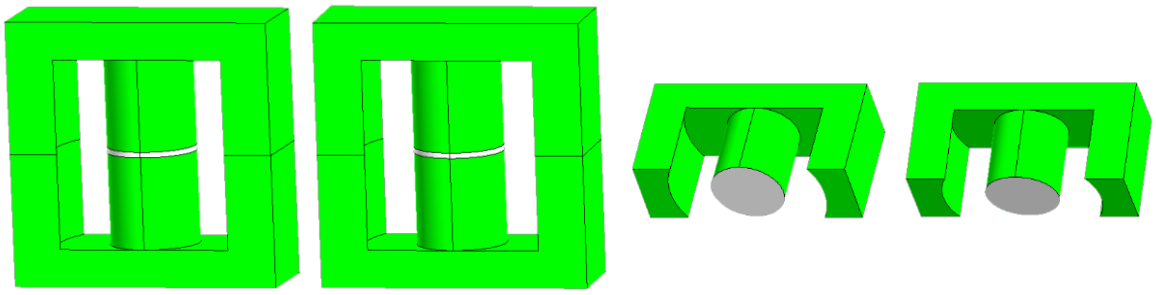

Figure i– FEA software ETD49 core model. (a) front view of VI core; (b) rear view of VI core; (c) lower-front view of one EFD25 piece; (d) lower-back view of one EFD25 piece

TABLE 9
DIMENSION VALUES FOR THE ETD49 VI CORE

Variable Name	Dimension [mm]	Variable Name	Dimension [mm]	Variable Name	Dimension [mm]
ALT1	24.7	**ALT2**	17.7	**COMP1**	49.8
COMP2	36.1	**COMP3**	16.7	**ESPESS**	16.7
GAP	1				

Coil properties

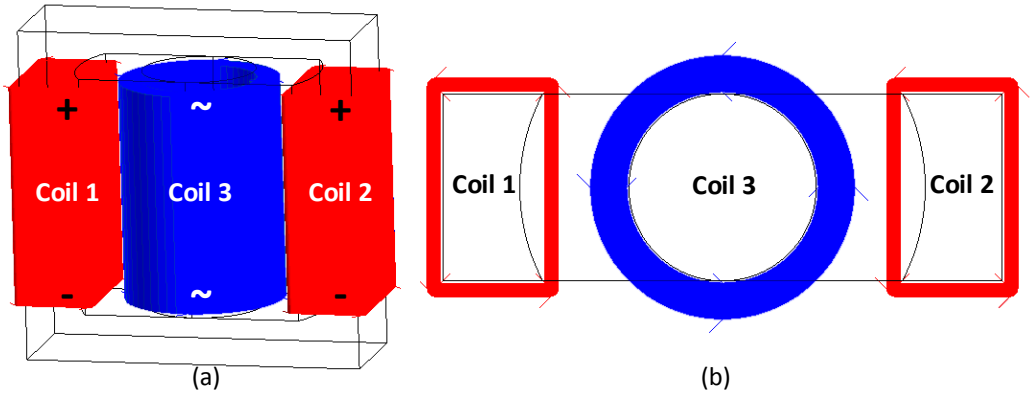

Figure ii- 3D non-meshed coil models built in FEA software. (a) Front view (b) Top view

TABLE 10
DIMENSION VALUES FOR THE ETD49 VI COIL CONSTRUCTION

Variable Name	Main winding	DC windings
$\chi\ [mm]$	0.15	0.15
$\tau\ [mm]$	3.27	1.28
$h\ [mm]$	32.7	32.7
N	70	86
K_u	0.63	0.67
ρ_e	$1.65E^{-8}$	$1.76E^{-8}$
ρ_m	8112	7046
$r_{cu}\ [mm]$	0.5575	0.322

Simulation results

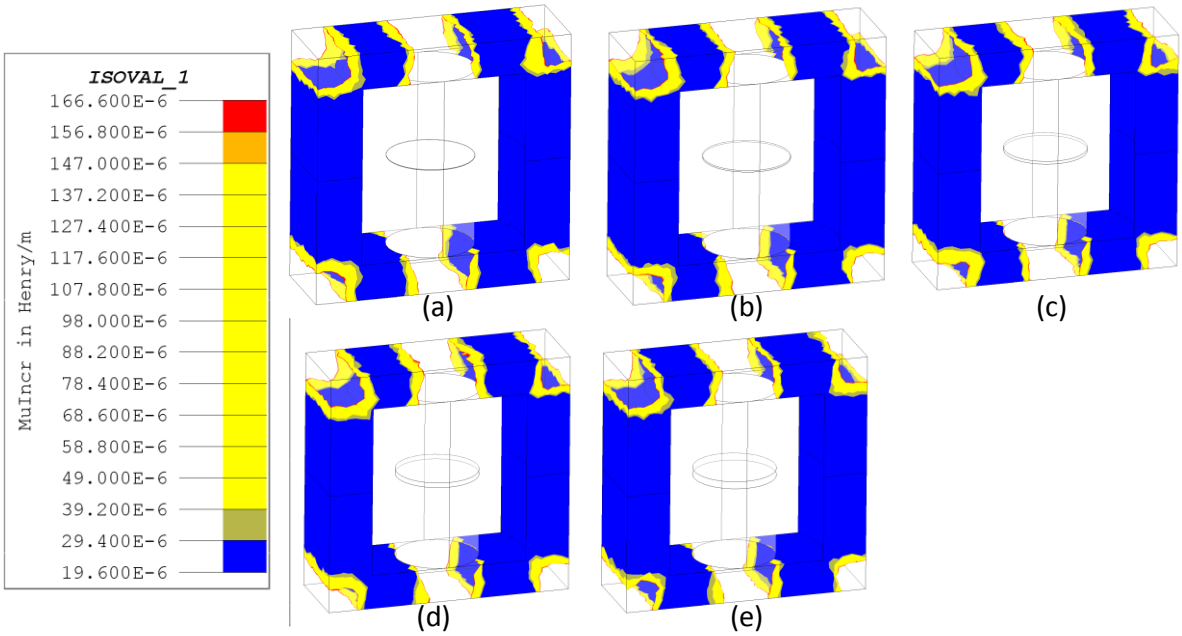

Figure iii – Differential permeability distribuition for H-fields higher than 300A.m-1, operating at minimum inductance conditions $i_{main} = 0.25A; i_{dc} = 1.5A$. (a) $l_g = 0.1mm$; (b) $l_g = 0.3mm$; (c) $l_g = 0.6mm$; (d) $l_g = 1mm$; (e) $l_g = 1.5mm$.

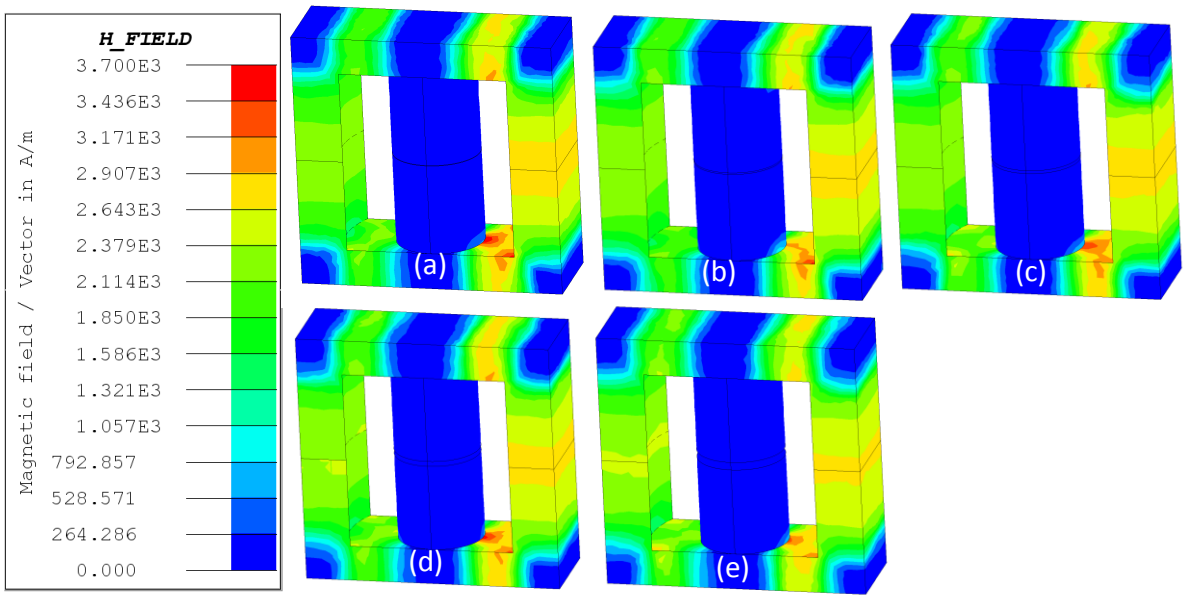

Figure iv– H-field distribution in minimum inductance conditions ($i_{main} = 0.25A; i_{dc} = 1.5A$) for different air-gap length. (a) $l_g = 0.1mm$; (b) $l_g = 0.3mm$; (c) $l_g = 0.6mm$; (d) $l_g = 1mm$; (e) $l_g = 1.5mm$.

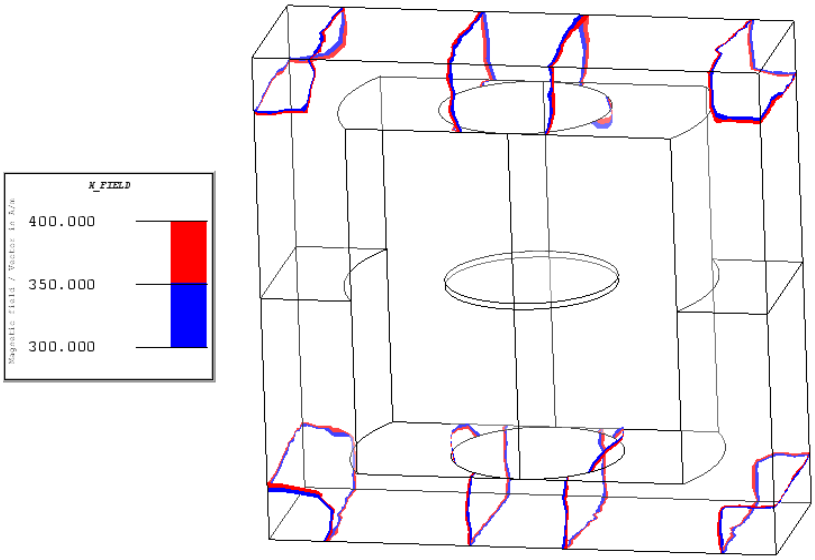

Figure v – Areas of the core operating with an H-field between 300A.m^{-1} and 400A.m^{-1} in minimum inductance conditions ($i_{main} = 0.25A; i_{dc} = 1.5A$).

A.2 EF25 VI

Initially, an EF VI was constructed to operate in the same conditions as the presented in [42]. Later it was tuned to operate in the same conditions as the EFD25 in this thesis. Therefore it was chosen a similar core in size, the same wire and number of turns in each coil, a similar air-gap length and similar current values. The characteristics and simulation results ares presented below.

General properties

Material: N87; **N_{dc}:** 71; **N_{ac}**:27; **Inductance variation:** 131µH ~ 52µH

Core Shape

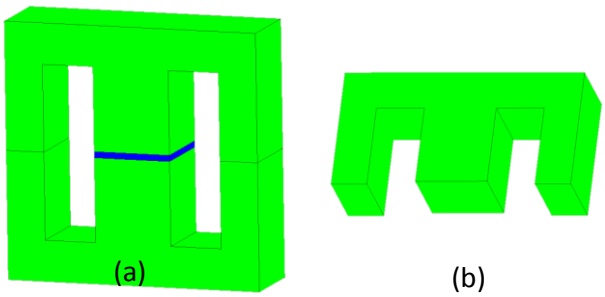

Figure vi – FEA software EF core model. (a) front and back view of VI core; (b) frond and back view of one EFD25 piece

TABLE 11
DIMENSION VALUES FOR THE EF25 VI CORE

Variable Name	Dimension [mm]	Variable Name	Dimension [mm]	Variable Name	Dimension [mm]
ALT1	12.8	**ALT2**	8.7	**COMP1**	25
COMP2	17.5	**COMP3**	7.5	**ESPESS**	7.5
GAP	0.6				

Coil properties

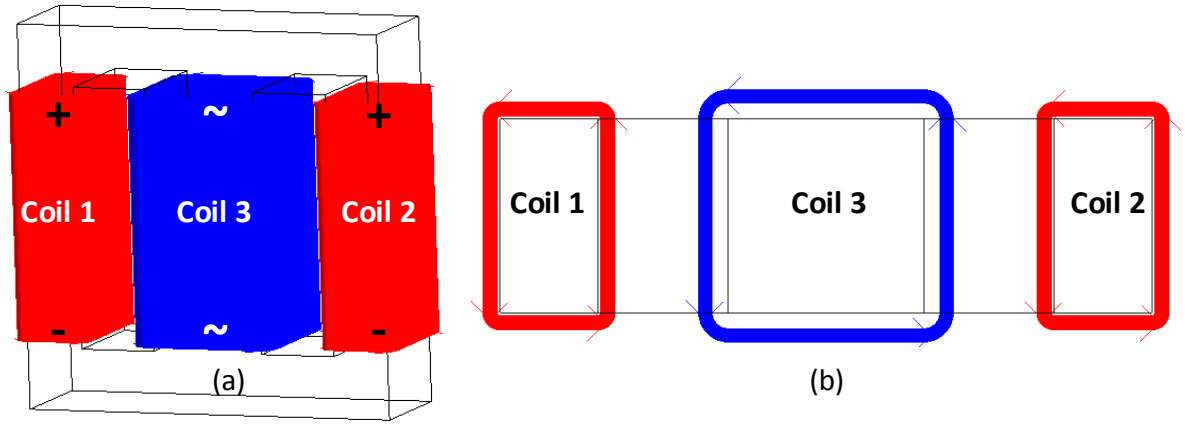

Figure vii - 3D non-meshed coil models built in FEA software. (a) Front view (b) Top view

TABLE 12
DIMENSION VALUES FOR THE EF25 VI COIL CONSTRUCTION

Variable Name	Main winding	DC windings
$\chi\ [mm]$	0.6	0.1
$\tau\ [mm]$	0.55	0.58
$h\ [mm]$	16.6	16.4
N	27	71
K_u	0.61	0.48
ρ_e	1.72E-8	1.68e-8
ρ_m	7794.55	7748.02
$r_{cu}\ [mm]$	0.26	0.14295

Simulation Results

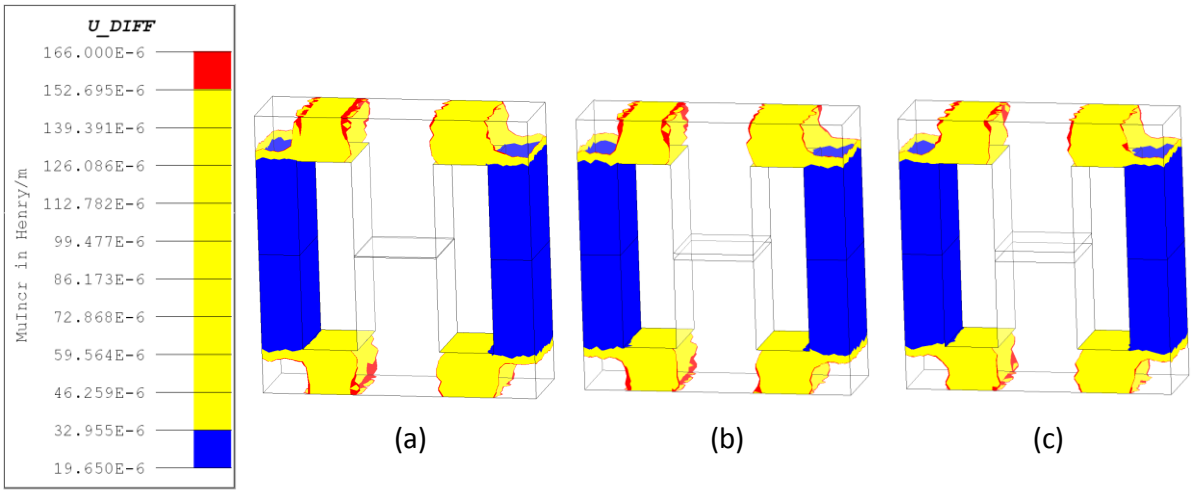

Figure viii - Differential permeability distribuition for H-fields higher than 300A.m-1operating at minimum inductance conditions $i_{main} = 0.1A; i_{dc} = 0.7A$ and different air-gap values. (a) $l_g = 0.1mm$; (b) $l_g = 0.6mm$; (c) $l_g = 1mm$.

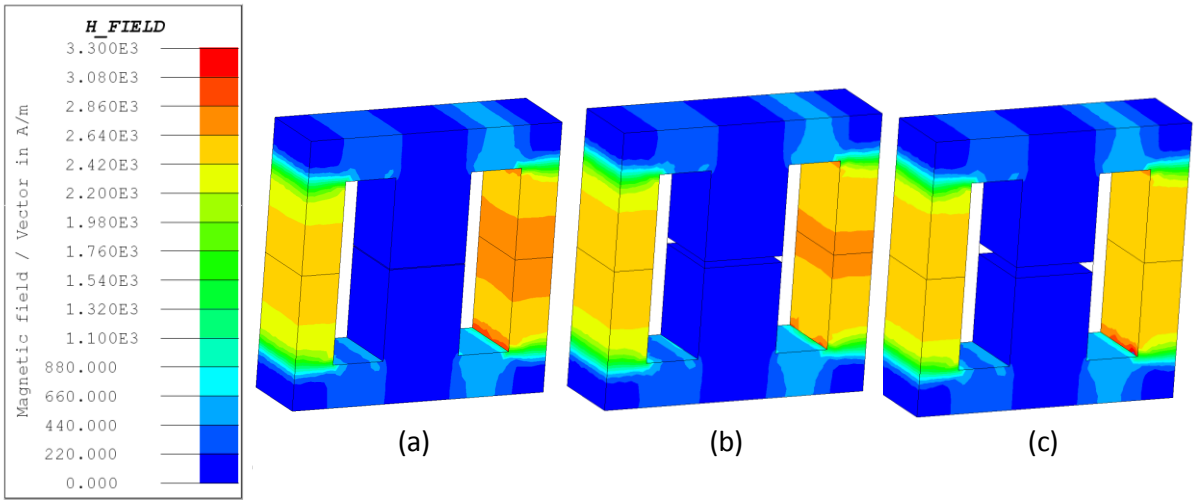

Figure ix - H-field distribution in minimum inductance conditions ($i_{main} = 0.1A; i_{dc} = 0.7A$) for different air-gap length. (a) $l_g = 0.1mm$; (b) $l_g = 0.6mm$; (c) $l_g = 1mm$.

APPENDIX B: NON-LINEAR MATERIAL MODULATION

B.1. N87

The N87 is a ferromagnetic material used this in the cores of the studied EFD25 EF25 and ETD49 VIs. The factory does not provide any information about the B(H) curve of the material except a low quality image containing the magnetic response of the material up to 1200 A.m^{-1}. Therefore, it was used an alternative method to extract the necessary information. Figure x shows the original B(H) curve with auxiliary straight lines superposed. These lines were used to mark the X and Y axis. The number of pixels between these lines and the origin was counted and, though a cross-multiplication rule extracted the correct mean point of the B(H) curve. TABLE 13 contains the data acquired.

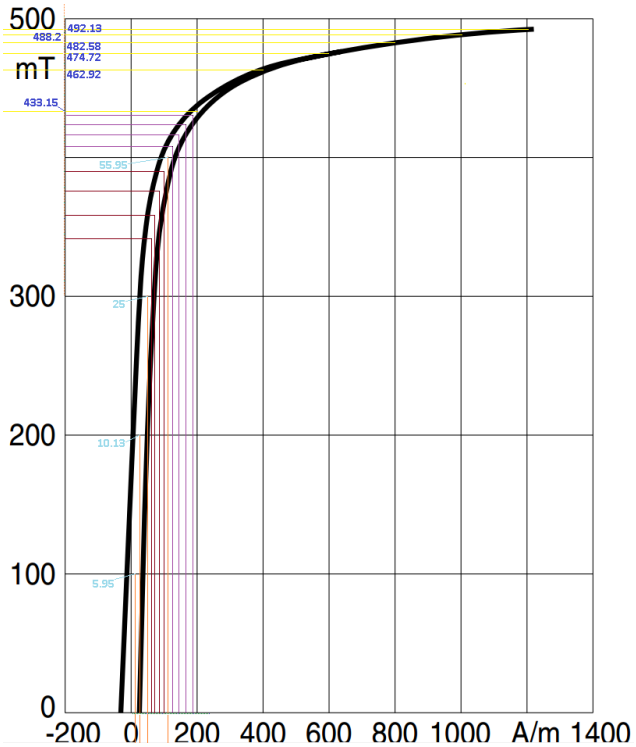

Figure x – Original N87 B(H) curve from [35] with auxiliary lines used to construct TABLE 13.

TABLE 13
SPLINE N87 B(H) CURVE VALUES USED IN THE FEA SOFTWARE

H [A.m^{-1}]	B [T]
0	0
11.9	0.1
20.26	0.2
47.61	0.3
61.9	0.34157
71.43	0.35843
85.71	0.37584
100	0.38989
111.9	0.4
126.19	0.40787
145.24	0.41629
166.67	0.4236
188.1	0.43146
200	0.43315
400	0.46292
600	0.47472
800	0.48258
1000	0.4882
1200	0.49213

In this work each ferromagnetic core was modelled according TABLE 13 data. The software uses an interpolation method to create a quasi-continuous B(H) curve. As an

alternative the software allows to model the material with the equation below (already presented in (3.10)).

$$B(H) = \mu_0 + J_s \frac{H_a + 1 - \sqrt{(H_a+1)^2 - 4H_a(1-a)}}{2(1-a)};\ H_a = \mu_0 H \frac{\mu_r - 1}{J_s}$$

The following parameters are the ones that best fit for the N87 according to the former equation: $J_s = 0.5$, $\mu_r = 8500$, a=0.5. However, the interpolation method models much better the N87 material particularly in the transition region. However, there is no information about the magnetic behaviour of the material for H-fields higher than 1200 A.m^{-1}. After 2000A.m^{-1}, the difference in the flux density value between these two methods is much more relevant. Figure xi shows a superposition of the N87 B(H) curves acquired by extraction (the spline curve), interpolation, and the equation (3.10).

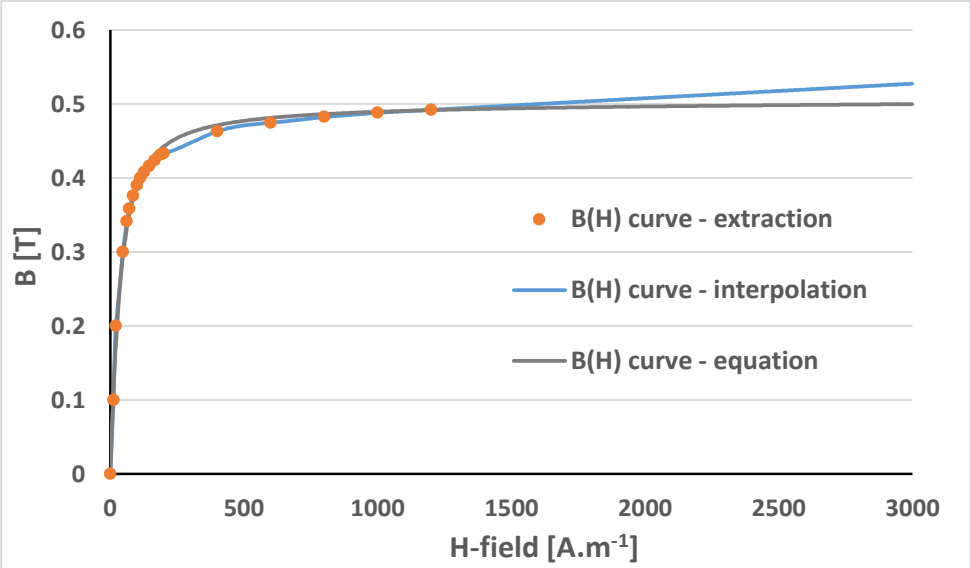

Figure xi – N87 B(H) curve acquired through extraction, interpolation and equation (3.10).

Figure xii shows the differential permeability of the N87 material. Each curve represents a different type of material modulation.

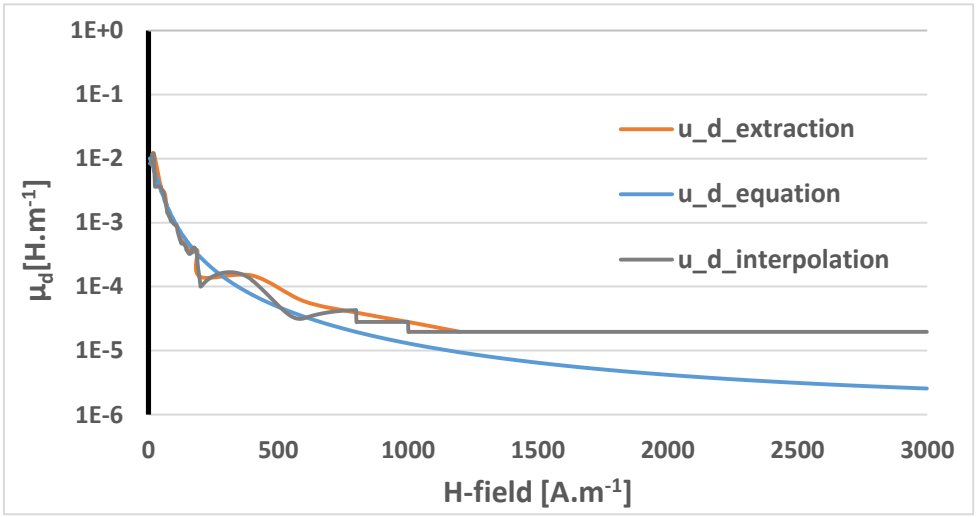

Figure xii - N87 B(H) differential permeability curve. Each curve is obtained through a different material modulation method

B.2. 3C85

The 3C85 is a ferromagnetic material which was not used in any core presented in this work. However it was used in the FEA for other applications and it is of interest present its results here. The parameters of equation (3.10) that best fit the 3C85 material are the following: $J_s = 0.44$, $\mu_r = 8500$, a=0.21. Figure xiii contains a superposition of the spline B(H) curve and the one obtained with equation (3.10). TABLE 14 contains the values of the spline B(H) curve.

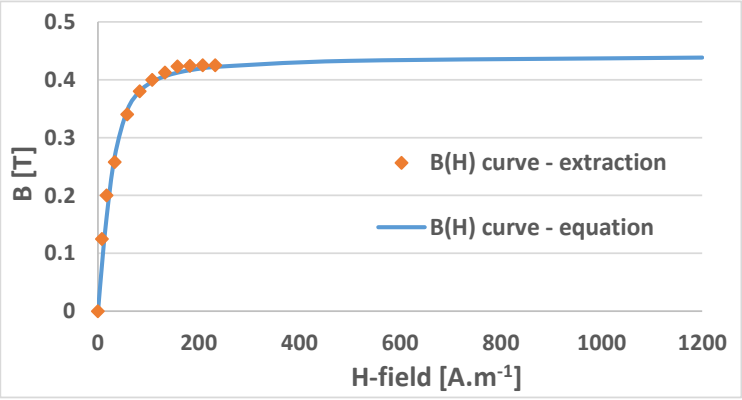

Figure xiii – B(H) curve of the 3C85. The orange dots were extracted from the datasheet of the material. The blue line was obtained with equation (3.10)

TABLE 14
3C85 B(H) CURVE VALUES USED IN THE FEA SOFTWARE

H [A.m^{-1}]	B [T]
0	0
8	0.125
17	0.2
33	0.258
58	0.34
83	0.38
108	0.4
133	0.4125
158	0.423
183	0.424
208	0.425
233	0.425

APPENDIX C: SCHEMATIC ALGORITHM OF THE PROPOSED DESIGN METHODOLOGY

A schematic of the proposed design methodology was drawn as shown below.

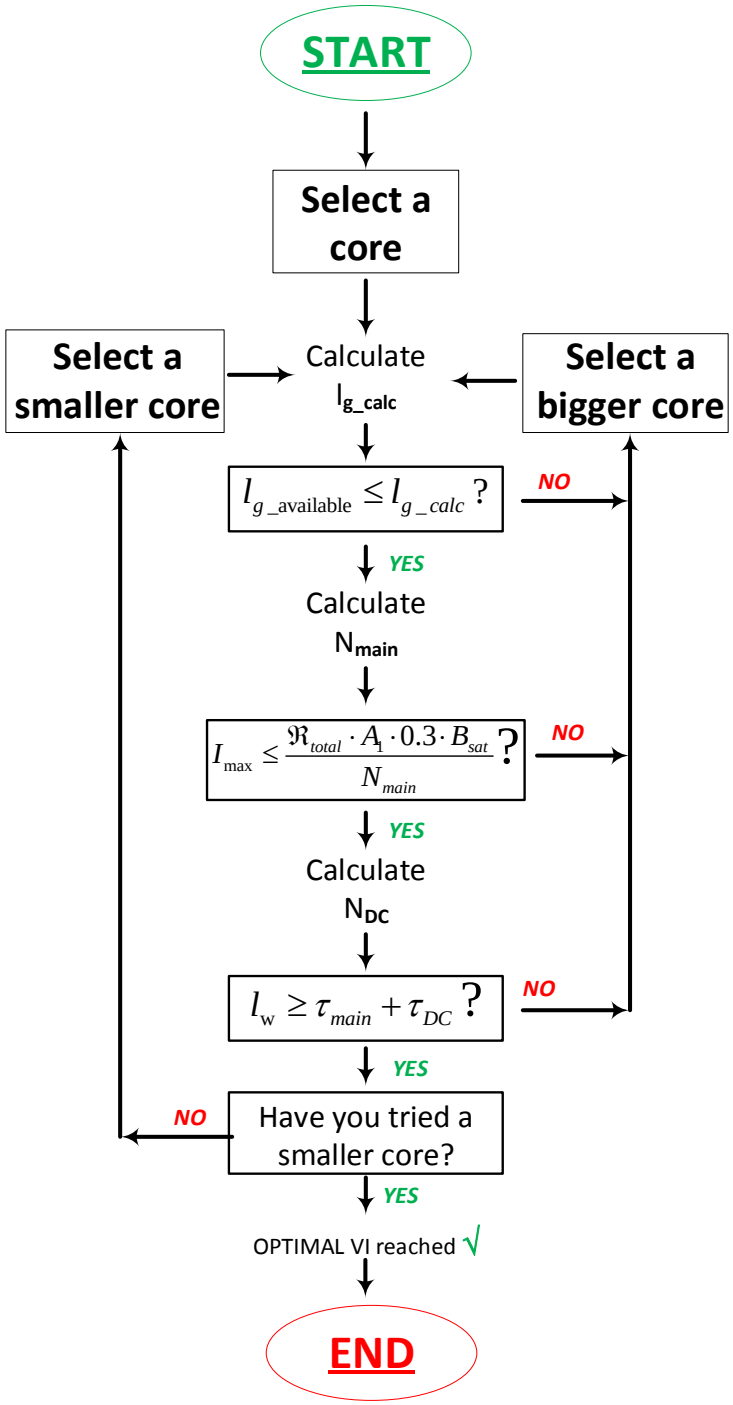

Figure xiv – The schematic algorithm figure of the proposed design procedure.

APPENDIX D: LABVIEW PROGRAM

A program was built in Labview containing part of the proposed design methodology. It was created to be intuitive, and of easy use. Figure xv contains a print-screen of the program.

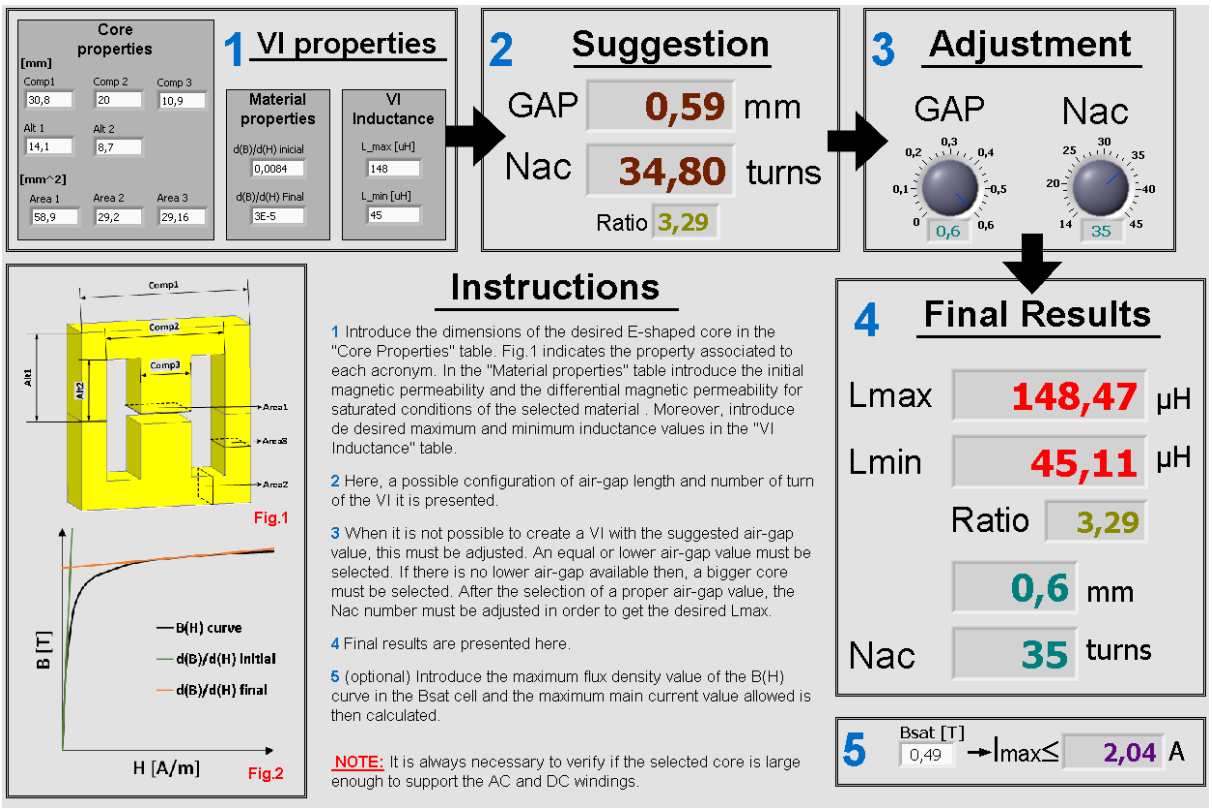

Figure xv– Print-screen of the VI design software built in Labview. .

This software allows anyone to design their own VI by simply introducing the core dimensions presented in the datasheet, the properties of the selected material and the desired inductance variation (in Section 1 of Figure xv) . The software calculates the optimal air-gap length and number of turns of the main winding (Section 2). Then it allows the designer to adjust the air-gap value to the closest lower possible available (Section 3). Still, in this section, the N_{ac} value must be regulated. The final results of maximum and minimum inductance values are presented in Section 4, as well as the respective ratio and the selected l_g and N_{ac}. In Section 5, after the introduction of B_{sat}, the maximum allowed main current is calculated.